

**THE FUNDAMENTAL DISSOLUTION KINETICS OF SILVER
SULFIDE AND MERCURY SULFIDE IN ATMOSPHERIC CYANIDE
SOLUTIONS**

by

Joon Won Lee

B.A.Sc., The University of British Columbia, 2010

A THESIS SUBMITTED IN PARTIAL FULFILLMENT OF THE REQUIREMENTS
FOR THE DEGREE OF

MASTER OF APPLIED SCIENCE

in

The Faculty of Graduate Studies

(Materials Engineering)

THE UNIVERSITY OF BRITISH COLUMBIA
(Vancouver)

June 2013

© Joon Won Lee, 2013

Abstract

The dissolution kinetics of pure silver sulfide (acanthite) and mercury sulfide (metacinnabar) were investigated using rotating disc and stirred reactor methods and the results were explained using the Levich and shrinking-core Parabolic Leach equations, respectively. It was observed that silver sulfide dissolution was limited by cyanide mass-transport and mercury sulfide by parabolic leaching. Silver sulfide leaching was practically unaffected by pH and dissolved oxygen concentrations while mercury sulfide leaching was sensitive to both parameters. Dissolution rates of both species increased linearly with cyanide concentration and activation energies were calculated using the Arrhenius rate equation as 5.15kJ/mol and 5.81kJ/mol, respectively, which indicates mass-transport control. It was also considered that silver sulfide dissolution is suppressed by sulfide-saturation in the solution, while mercury dissolution is inhibited by the growth of sulfur-rich product layers on the particles. Kinetic results were compared to extraction experiments conducted on a spent Heap Leach Residue sample from the Yanacocha Mine in Peru which contained acanthite and cinnabar as its primary silver and mercury species. Extraction kinetics of silver from the Leach Residue was analogous to pure silver sulfide's experimental results, except that extraction rates decreased with pH. Mercury extraction from the residue was insensitive to both cyanide and pH, but was responsive to oxygen concentration. The discrepancies between pure sample investigations and the Leach Residue suggest that unforeseen interactions with other minerals may be affecting the extraction rates of silver and mercury from the Yanacocha Mine.

Preface

All of the experimental data used in the current work were produced from original experiments that were conducted by this author at the Department of Materials Engineering at the University of British Columbia. This refers to all of the data retrieved from the rotating disc experiments of silver sulfide, stirred reactor experiments of mercury sulfide, and stirred reactor experiments of the Leach Residue obtained from the Yanacocha Mine.

Supervision of the project was provided by Dr. David Dreisinger who overviewed the research objectives, experimental approach, and analysis of results. Dr. Berend Wassink advised on establishing proper experimental and analytical procedures. The project was sponsored by the Newmont Mining Corporation, who also provided the spent Leach Residue sample for experiments.

Table of Contents

Abstract	ii
Preface	iii
Table of Contents	iv
List of Tables	vii
List of Figures	viii
List of Equations	xi
Nomenclature	xii
Acknowledgements	xiii
Dedication	xiv
1 Introduction	1
2 Background Information	3
2.1 Markets, Economics and Resources.....	3
2.1.1 Silver Uses and Market Trends	3
2.1.2 Silver Sources and Mineralogy.....	4
2.1.3 Mercury Market Trends	5
2.1.4 Mercury Environmental Regulations	6
2.1.5 Mercury Sources and Mineralogy.....	7
2.1.6 Mercury Toxicology.....	8
2.2 Chemical and Physical Properties	11
2.2.1 Silver Metal Properties	11
2.2.2 Silver Sulfide Properties.....	11
2.2.3 Silver-Cyanide-Sulfur Species.....	12
2.2.4 Mercury Metal Properties	18
2.2.5 Mercury Sulfide Properties	19
2.2.6 Mercury-Cyanide-Sulfur Species.....	20
2.3 Kinetics Studies	23
2.3.1 Dissolution Kinetics of Silver Metal	23
2.3.2 Dissolution Kinetics of Silver Sulfide.....	28
2.3.3 Dissolution Kinetics of Mercury Sulfide	33
3 Research Objectives	36
4 Experimental Set-up	37
4.1 Materials	37

4.1.1	General Reagents	37
4.1.2	Silver Sulfide Reagent	37
4.1.3	Mercury Sulfide Reagent	38
4.1.4	Heap Leach Residue Composite.....	38
4.2	Equipment	40
4.2.1	Compressed Silver Sulfide Discs.....	40
4.2.2	Hardware and Equipment.....	41
4.3	Analytical Methods	42
4.3.1	Titration of Free Cyanide, Colorimetric	42
4.3.2	Atomic Adsorption Spectroscopy (AAS).....	44
4.3.3	Cold Vapour Atomic Adsorption (CVA-Hg)	44
4.3.4	Metallographic Techniques (SEM/EDS, XRD, XPS).....	45
4.4	Experimental Methods.....	46
4.4.1	Silver Sulfide - Rotating Disc Experiment.....	46
4.4.2	Mercury Sulfide – Stirred Reactor Experiment.....	50
4.4.3	Leach Residue – Stirred Reactor Experiment	52
5	Experimental Results	54
5.1	Silver Metal Results.....	54
5.1.1	Silver Rotating Disc - Validation of Method.....	54
5.2	Silver Sulfide Results	56
5.2.1	Silver Sulfide & Non-linear Dissolution Rates	56
5.2.2	Silver Sulfide Particle Size Distribution and Disc Treatment	58
5.2.3	Silver Sulfide Dissolution Kinetics Results.....	59
5.3	Mercury Sulfide Results	65
5.3.1	Mercury Sulfide Dissolution & Shrinking Core Model	65
5.3.2	Mercury Sulfide Solubility.....	69
5.3.3	Mercury Sulfide Kinetic Results	72
5.4	Leach Residue Results	78
5.4.1	Leach Residue Experimental Conditions.....	78
5.4.2	Leach Residue & Silver Extraction.....	79

5.4.3	Leach Residue & Mercury Extraction.....	81
6	Discussion	85
6.1	Dissolution Kinetics of Silver Sulfide	85
6.1.1	Silver Sulfide Rate Controlling Mechanism.....	85
6.1.2	Silver Sulfide & Cyanide, Oxygen and pH Effects.....	85
6.1.3	Silver Sulfide & Ferricyanide, Hydrogen Peroxide	87
6.1.4	Silver Sulfide & Sulfide Oxidation Limited Kinetics.....	88
6.2	Dissolution Kinetics of Mercury Sulfide	91
6.2.1	Mercury Sulfide Rate Controlling Mechanism.....	91
6.2.2	Mercury Sulfide & Sulfide Oxidation Limited Kinetics.....	91
6.2.3	Mercury Sulfide & Cyanide, Oxygen and pH Effects.....	92
6.3	Dissolution Kinetics Heap Leach Residue, Yanacocha Mine	96
6.3.1	Leach Residue Silver Extraction & Cyanide, Oxygen and pH	96
6.3.2	Leach Residue Silver Extraction & Sulfide Saturation.....	97
6.3.3	Leach Residue Mercury Extraction & Cyanide, Oxygen and pH	98
7	Conclusion.....	100
	References	103
	Appendix.....	106
	Appendix A: Calculation of the Activation Energy	106
	Appendix B: Mineral Assay of Heap Leach Residue	107

List of Tables

Table 1: Reduction Reactions for Ag-CN-H ₂ O Eh-pH Diagrams.....	13
Table 2: Mercury-Cyanide Complexes Stability Constants (Penneman & Jones, 1961)	20
Table 3: Experimentally Analyzed Silver and Mercury Concentrations in Leach Residue	39
Table 4: Conditions of Silver Sulfide Rotating Disc Experiments	60
Table 5: Conditions of Mercury Sulfide (Metacinnabar) Stirred Reactor Experiments	73
Table 6: Conditions for Heap Leach Residue (Source: <i>Yanacocha Mine</i>) Stirred Reactor Experiments	78

List of Figures

Figure 1: Multi Year Silver Prices, 2000-2013 (Kitco, 2013).....	4
Figure 2: Ag-H ₂ O System – 0.001M Ag, HSC Software.....	13
Figure 3: Ag-H ₂ O System – 0.001M Ag, Xue & Osseo (1985).....	14
Figure 4: Ag-S-H ₂ O System – 0.001M Ag ₂ S, HSC Software.....	14
Figure 5: S-H ₂ O System - 5x10 ⁻⁴ M S, HSC Software.....	15
Figure 6: Ag-CN-H ₂ O System – 0.001M Ag, 0.1M CN ⁻ , HSC Software.....	15
Figure 7: Ag-CN-H ₂ O System – 0.001M Ag, 0.1M CN ⁻ , Xue & Osseo (1985).....	16
Figure 8: Ag-CN-H ₂ O System – 0.001M Ag, 0.0097M CN ⁻ , HSC Software.....	16
Figure 9: Ag-CN-H ₂ O System – 0.001M Ag, 0.0010M cyanide, Xue & Osseo (1985).....	17
Figure 10: Ag-S-CN-H ₂ O System – 0.001M Ag ₂ S, 0.1M cyanide, HSC Software.....	17
Figure 11: Ag-S-CN-H ₂ O System - 2.5E-5M Ag ₂ S, 0.002M CN (baseline conditions), HSC Software.....	18
Figure 12: Hg-CN-H ₂ O System – 0.001M Hg, 0.1M CN / HSC Software.....	21
Figure 13: Hg-S-CN-H ₂ O System – 0.001M HgS, 0.1M CN / HSC Software.....	21
Figure 14: Hg-S-CN-H ₂ O System – 2.5E-5M Hg, 0.002M CN / HSC Software.....	22
Figure 15: Silver Oxidation & Oxygen Reduction Polarography (Hiskey & Sanchez, 1990).....	24
Figure 16: Silver Limiting Current Density vs. (RPM) ^{1/2} & Cyanide Concentration (Li & Wadsworth, 1993)	25
Figure 17: Oxygen Reduction Model of Direct and Sequential Pathways (Wadsworth, 2000).....	27
Figure 18: Silver Oxidation vs. Direct and Sequential Oxygen Reduction, Polarography (Wadsworth, 2000)	28
Figure 19: Dependence of Mercury Sulfide Extractability on Solids Added (<i>Mikac et al, 2002</i>).....	35
Figure 20: Silver Sulfide Particle Size Distribution (PSA), by Mastersizer®.....	37
Figure 21: Heap Leach Residue Sample, Particle Size Analysis (PSA).....	39
Figure 22: Silver Sulfide Disc Sample (1-silver sulfide disc, 2-epoxy casing, 3-adapter, 4-threading).....	40
Figure 23: Potentiometric ("Potential") vs. Colorimetric ("UV") Titrations Comparison (Breuer et al., 2011)	43
Figure 24: Rotating Disc Leaching Diagram.....	47
Figure 25: Rotating Disc Experiment Set-up (1-heated water bath, 2-water level, 3-heating element, 4-bath water stirrer, 5-temperature controller, 6-45° flow blade, 7-Disc Rotator, 8-silver disc sample, 9-reactor vessel).....	49
Figure 26: Leach Vessel Geometry (" <i>Mixing and Mass Transfer in Hydrometallurgy</i> ", presentation by Dr. David Dixon).....	50
Figure 27: Silver Metal Dissolution vs. Time (0.5g/L NaCN, pH 11.0, 25°C, 600rpm, air).....	54
Figure 28: Reproducible Silver Sulfide Dissolution vs. Time - 2 hour results (0.10g/L NaCN, pH 10.5, 25°C, 600rpm, air).....	56
Figure 29: Reproducible Silver Sulfide Dissolution vs. Time, initial 20 minutes (0.10g/L NaCN, pH 10.5, 25°C, 600rpm, air).....	57
Figure 30: Silver Sulfide Dissolution vs. Time, Various Surface Treatments.....	58
Figure 31: Silver Sulfide Flux vs. Cyanide Concentration (0.025g/L, 0.05g/L, 0.10g/L, 0.25g/L NaCN pH 10.5, 25°C, 600rpm, air).....	60

Figure 32: Silver Sulfide Flux vs. Square Root Rotation Speed (300, 400, 600, 800, 1000rpm - 0.10g/L NaCN, pH 10.5, 25°C, air)	61
Figure 33: Silver Sulfide Flux vs. Dissolved Oxygen Concentration (N ₂ , air, O ₂ - 0.10g/L NaCN, pH 10.5, 25°C, 600rpm)	61
Figure 34: Silver Sulfide Flux vs. pH (pH 10.5, 11.0, 11.5 – 0.10g/L NaCN, 25°C, 600rpm, air)	62
Figure 35: Log(Silver Sulfide Flux) vs. Inverse of Temperature (20, 25, 30, 35°C - 0.10g/L NaCN, pH 10.5, 600rpm, air)	63
Figure 36: Silver Sulfide Dissolution vs. Time, Oxidants (0.10g/L NaCN, 25°C, 600rpm – hydrogen peroxide, ferricyanide).....	64
Figure 37: Parabolic Leaching Particle Diagram.....	66
Figure 38: Parabolic Leach Rate, Extraction Data Plot.....	67
Figure 39: Linear Leaching Particle Diagram.....	68
Figure 40: Linear Leaching Rate, Extraction Data Plot.....	69
Figure 41: Mercury Sulfide Dissolution vs. Time, α-HgS, β-HgS, and p-HgS (0.5g/L HgS, 1.0g/L NaCN, pH 11.5, 25°C, 700rpm, air)	69
Figure 42: Mercury Sulfide (Cinnabar) Dissolution vs. Time, 1g/L & 10g/L NaCN (0.5g/L HgS, pH 11.5, 25°C, air, 700rpm)	70
Figure 43: Mercury Sulfide (Metacinnabar) Dissolution vs. Time, 0.5g/L & 0.01g/L HgS (1g/L NaCN, 25°C, pH 11.5, 700rpm, air).....	71
Figure 44: Mercury Sulfide (Metacinnabar) Dissolution vs. Time, Stir Speed (0.5g/L HgS, 1g/L NaCN, 25°C, pH 11.5, air).....	72
Figure 45: Mercury Sulfide (β-HgS) Extraction vs. Time (1.0, 0.5, 0.25, 0.15, 0.10, 0.05, 0.025g/L NaCN – pH 11.5, 25°C, air)	73
Figure 46: Mercury Sulfide Linearized Extraction vs. Time (1.0, 0.5, 0.25, 0.15, 0.10, 0.05, 0.025g/L NaCN – pH 11.5, 25°C, air)	74
Figure 47: Mercury Sulfide Rate Constant vs. Cyanide Conc. (1.0, 0.5, 0.25, 0.15, 0.10, 0.05, 0.025g/L NaCN – pH 11.5, 25°C, air)	75
Figure 48: Mercury Sulfide Rate Constant vs. Dissolved Oxygen Concentration (O ₂ , air, N ₂ - 1g/L NaCN, pH 11.5, 25°C)	75
Figure 49: Mercury Sulfide Rate Constant vs. pH (pH 10.5, 11.0, 11.5 - 1 g/L NaCN, 25°C, air).....	76
Figure 50: Log(Mercury Sulfide Rate Constant) vs. Temperature ⁻¹ (25°C, 35°C, 40°C - 1 g/L NaCN, pH 11.5, air).....	77
Figure 51: Silver Extraction from Residue vs. CN Concentration (0.10, 0.25, 0.5g/L NaCN, pH 11.5, 25°C, air).....	79
Figure 52: Silver Extraction from Residue vs. Oxygen Content (sparged air, oxygen - 0.10g/L NaCN, pH 11.5, 25°C).....	80
Figure 53: Silver Extraction from Residue vs. pH (pH 10.5, 11.0, 11.5 – 0.1g/L NaCN, 25°C, air).....	80
Figure 54: Silver Extraction from Residue vs. Temperature (25°C, 35°C - 0.10 g/L NaCN, pH 11.5, air)	81
Figure 55: Mercury Extraction from Residue vs. CN Concentration (0.10, 0.25, 0.5 g/L NaCN, pH 11.5, 25°C, air).....	82
Figure 56: Mercury Extraction from Residue vs. pH (pH 10.5, 11.0, 11.5 - 0.10 g/L NaCN, 25°C, air).....	83

Figure 57: Mercury Extraction from Residue vs. Dissolved Oxygen Concentration (air, oxygen - 0.10 g/L NaCN, pH 11.5, 25°) 83

Figure 58: Mercury Extraction from Residue vs. Temperature (25°C, 35°C - 0.10 g/L NaCN, pH 11.5, air) 84

Figure 59: Silver Dissolution vs. Oxygen Concentration at Varying CN Concentrations (Senanayake, 2006) 86

Figure 60: Silver Sulfide Dissolution Rate vs. Cyanide Concentration in Ferricyanide (0.5g/L Fe as Fe(CN)₆³⁻, pH 11.5, 25°C, N₂, 600rpm - Xie, 2007) 87

Figure 61: Hypothesized Mercury Sulfide Reaction Pathway Diagram 93

List of Equations

Equation 1: Parabolic Rate Law by (Dutrizac, 1994)	29
Equation 2: Free Cyanide Concentration Calculation for Titration by Silver Nitrate.....	42
Equation 3: Levich Equation, Limited Current Density of Rotating Disc Electrode (Gileadi, 1993)	46
Equation 4: Levich Equation, Molar Flux Rate of Dissolving Disc	47
Equation 5: Critical Reynold's Number for Laminar Flow Around a Rotating Disc	48
Equation 6: Oxygen Diffusion in Solutions (Tromans, 1998)	62
Equation 7: Arrhenius Rate Law.....	63
Equation 8: Parabolic Leaching Extraction Equation	66
Equation 9: Parabolic Rate Constant for Constant Particle Size (r_0).....	67
Equation 10: Linear Leaching Extraction Equation	68
Equation 11: Dissociation Product of Mercury Sulfide	71
Equation 12: Parabolic Rate Constant Equation, k_2' (Peters, n.d.)	94

Nomenclature

i_L	(A/m ²)	limiting current
$J_{A,D}$	($\mu\text{mol}/\text{m}^2/\text{sec}$)	dissolution flux of reagent (A) or product (D)
ν	(cm/s ²)	kinematic viscosity
ω	(rad/s)	rotation speed
D	(cm/s ²)	diffusion coefficient
C^o	(mol/L)	bulk concentration
P_{80}	(μm)	diameter of which 80% of particles can pass
k_1	(s ⁻¹)	linear rate constant (Linear Leach equation)
k_2	(s ⁻¹)	parabolic rate constant (Parabolic Leach equation)
k_1'	(s ⁻¹ m ⁻¹)	linear rate constant of constant particle radius
k_2'	(s ⁻¹ m ⁻¹)	parabolic rate constant of constant particle radius
r_o	(cm)	Outer particle radius
r_c	(cm)	Unleached core radius
C_o	(mol/L)	Reagent concentration at outer particle surface (Shrinking Core model)
C_c	(mol/L)	Reagent concentration at unleached core surface (Shrinking Core model)
M_d	(mol/L)	Concentration of diffusing chemical species during Parabolic Leaching
M_s	(mol/L)	Concentration of reacting solute during Parabolic Leaching

Acknowledgements

I would like to thank the members of staff and the professors in the department of Materials Engineering at the University of British Columbia for their warmth, kindness and respect towards their students, both during my undergraduate and graduate studies. I would also like to thank my family and peers who have always been supportive and guided me to move forward.

I am truly grateful to my supervisor, Dr. David Dreisinger, for the opportunity to study under him in this prestigious program, for his guidance with technical expertise, and for teaching his student the virtues of optimism, persistence and integrity as an engineer. I would like to thank Dr. Berend Wassink for his uncompromising dedication to performing beyond expectations in his role as Technical Advisor, and also Dr. Peter Barr for providing me with a suitable lab area for my experiments. Lastly, I would like to thank the Newmont Mining Corporation for the research opportunity and sponsorship to pursue this project.

Dedication

I dedicate this work, first and foremost, to my Lord and Father in heaven who ensures that I may become a better man every day. “No temptation has overtaken you except such as is common to man; but God *is* faithful, who will not allow you to be tempted beyond what you are able, but with the temptation will also make the way of escape, that you may be able to bear *it*” (1 Corinthians 10:13, NKJV)

I also dedicate this work to my parents, Saeng-Bock Lee and Joong-Mi Lee, who have overcome unparalleled hardships to ensure that I would benefit from the finest opportunities that are available to me in Canada. Only now, as I begin to make significant decisions in life as an adult, do I begin to appreciate their great gift of love. My gratitude also extends to my two sisters, Jung-Eun Lee and Young-Eun Lee, who have always been at my side as both friends and advisors in my life.

1 Introduction

Unexpectedly low silver recoveries were realized from the heap leach pads at the Yanacocha Mine in Peru, operated by the Newmont Mining Corporation. Silver recoveries averaged 9% from run-of-mine ores when leached with 90ppm NaCN solutions while gold recoveries exceeded 85% (Acar, 2010). As silver prices have increased significantly in recently years, this represents a significant economic loss. Higher silver recoveries could be achieved from Yanacocha by raising the cyanide concentration, but this also resulted in a new issue of increased mercury extractions (Acar, 2010). This is both an environmental and economic setback as environmental regulations are becoming stricter surrounding international sales of mercury (W. E. Brooks, 2011). Consequently, producers of by-product mercury must seek domestic methods of storage, which can be costly. It would be more desirable, therefore, to conduct heap leaching under conditions where mercury liberation is suppressed while maximizing silver extractions.

Analysis of the Yanacocha's mineralization by Newmont identified acanthite (Ag_2S) and cinnabar (HgS) as the primary silver and mercury species, respectively (McComb & Thogerson, 2011). Much work has been published regarding the dissolution kinetics of metallic silver and gold in cyanide solutions by *Hiskey & Sanchez (1990)* and *Li & Wadsworth (1993)*, but the kinetics of silver sulfide has not been extensively reviewed. The oxidative dissolution kinetics of mercury sulfide has been investigated in oxygenated waters and corrosive solutions by *Holley et al (2007)* and *Mikac et al (2002)*, but not in cyanide solutions. It is known that metallic silver dissolves at approximately half the rate of gold in cyanide solutions, and the rate of silver

sulfide is expected to be lower (Xie & Dreisinger, 2007). However, a more accurate knowledge of the reaction kinetics of these species and their rate controlling mechanisms is integral to understanding the challenges associated with precious metal extraction from the Yanacocha ores.

2 Background Information

2.1 Markets, Economics and Resources

2.1.1 Silver Uses and Market Trends

The global production of silver increased by 5% between 2009 and 2010 to 23,100t while consumption increased by 21%. This illustrates a significant shortage of supply and a considerable economic opportunity for silver producers (B. W. E. Brooks, 2010). U.S. demand for silver coins, industrial applications, and jewellery also increased by 21%, 19%, and 11%, respectively (W. E. Brooks, 2010), which reveals that silver is valued in a diverse range of markets including financial investment, consumer products, and aesthetics. The only decreasing market was the once-great photography industry, which dropped by 14% due to competition from digital technology (W. E. Brooks, 2010).

Silver uses are increasing in medical, biocidal, and electronic applications due to its antibacterial and conductive properties. Applications of silver includes flat screen televisions, heating elements in automobile windows, water purification systems, silver-backed mirrors, and printed electronics (B. W. E. Brooks, 2010). In particular, silver uses in the photovoltaic cell industry are growing where consumption increased by 72% in 2010 to 1500t due to increasing consumer interest in solar panels in light of rising energy prices (B. W. E. Brooks, 2010). Nano-silver is sought after in textiles and shoes as an antibacterial agent, and silver-based disinfectants are used as an environmentally sensitive alternative in care centres and food processing facilities (B. W. E. Brooks, 2010).

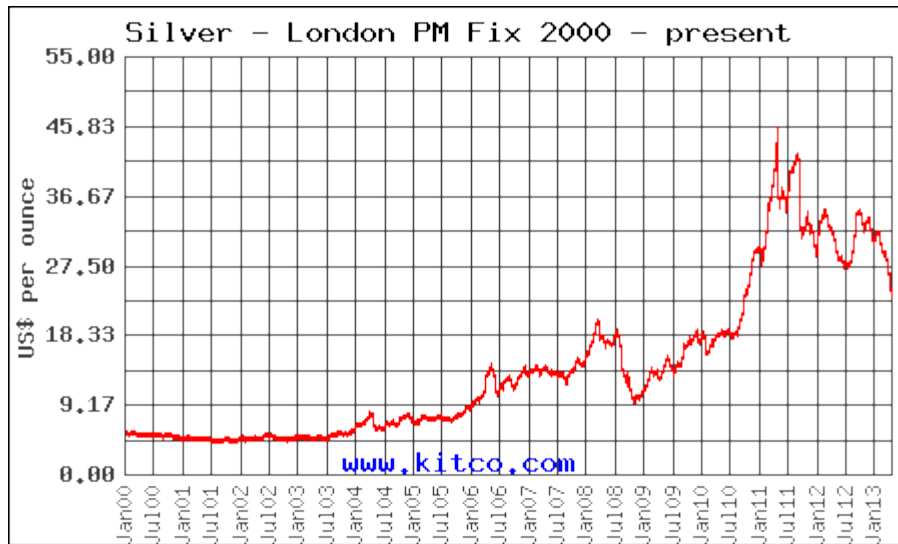


Figure 1: Multi Year Silver Prices, 2000-2013 (Kitco, 2013)

In recent years, the price of silver rose from an average of ~US\$5/oz prior 2003. A peak price of US\$47.81/oz was reached in March of 2011 before stabilizing to the current rate of below US\$30.00/oz (Figure 1).

2.1.2 Silver Sources and Mineralogy

The average silver concentration in the earth's crust is estimated to be 0.075 parts per million (ppm), ranking 65th in abundance which is just below mercury and 19 times higher than gold (Butterman & Hilliard, 2004). Globally, only one-quarter of silver is produced from principle silver deposits while the remainder is a by-product of other extractive processes. For example, in 2001 only 14% of the silver mined in the United States was obtained from primary silver ores, whereas 39% came from gold ores, 10% from copper and copper-molybdenum ores, and 37% from lead, zinc, and lead-zinc ores (Butterman & Hilliard, 2004).

Silver is always present in gold ores, but it is also commonly found in sulfide deposits of copper, lead, and zinc. Among the base metals, it is most commonly found with galena (PbS) and chalcopyrite (CuFeS₂) where it may be present as inclusions or substitutes of base-metal atoms in mineral lattices (Butterman & Hilliard, 2004). Silver is particularly rich in the oxidized regions of sulfide deposits and sometimes form small pockets that exceed thousands of grams per ton (Butterman & Hilliard, 2004). In gold ores, silver is often alloyed as gold electrum or present as discrete silver minerals (Butterman & Hilliard, 2004).

Currently, Mexico is the leading producer of silver, recently attaining that status when production increased by 34% from 3,640t in 2009 to 4,411t in 2010 (B. W. E. Brooks, 2010). Peru and China are the second and third biggest producers having supplied 3,640t and 3,500t, respectively, in 2010. Other notable producers include Argentina, Australia, and Bolivia which produced 123t, 1,864t, and 1,259t annually, respectively (B. W. E. Brooks, 2010).

2.1.3 Mercury Market Trends

Currently, mercury is predominantly used in small-scale gold-recovery operations as an amalgamating agent (W. E. Brooks, 2011). Due to this unique application, mercury prices have remained high following gold's recent strong economy (Salazar & McNutt, 2012). It is also used largely by the chlorine-caustic industry and in consumer products such as energy-efficient light bulbs, but consumption from these industries are slowly declining (W. E. Brooks, 2011). As a result, the average price of mercury in 2011 rose to US\$1,950 per flask (unit flask = 34.5 kg of

metallic mercury), which was substantially higher than US\$1,075 in 2010 and US\$600 in 2009 (Salazar & McNutt, 2012).

Traditionally, mercury was used in thermometers, barometers, tilt-switches, oscillators, fluorescent light bulbs, batteries, and in paints as an antifungal agent (Jasinski, 1994). However, mercury uses in consumer products have decreased in order to control its discharge into landfills. Historically, high mercury losses were observed from the chlorine-caustic industry where it was used as the preferred cathodic connector losses declined from 0.12kg Hg/(mt chlorine) to 0.04kg/(mt chlorine) through the adoption of new technologies (Jasinski, 1994).

2.1.4 Mercury Environmental Regulations

Since the early 1970s, the U.S. Environmental Protection Agency (EPA) established numerous powerful legislations to drastically reduce the industrial discharge of mercury. The “Clean Air Act” of 1970, “Federal Water Pollution Control Act” of 1972, and the “Resource Conservation and Recovery Act” of 1978 were all intended to mitigate the environmental release of mercury (Jasinski, 1994). Although the measures were extreme, positive responses were observed from industry. In 1991, the EPA requested over 600 U.S. companies to reduce the discharge of mercury and 17 other toxic substances by 33% by the end of 1992. This goal was achieved one year early and a 34% decrease was achieved by the end of 1991 (Jasinski, 1994).

More recently, America’s Mercury Export Ban Act of 2008 (MEBA) will prohibit the sale and transfer of elemental mercury outside of the U.S. starting January 1, 2013 (W. E. Brooks, 2010).

This, along with similar restrictions enforced by the European Union, are pressuring the global availability of mercury and causing its value to rise (Salazar & McNutt, 2012). As a negative side-effect, it is expected that discontinued mercury mines in third-world countries may be re-commissioned in order to supply mercury to their small-scale gold operations (W. E. Brooks, 2010).

2.1.5 Mercury Sources and Mineralogy

Cinnabar (α -HgS, red) is the most abundant naturally occurring mercury species in the western coast of North America (Eurick, 2000; Holley et al, 2007). The average mercury concentration in the earth's crust is estimated to be 0.08ppm, which can reach up to 100ppm (mg/kg) near regions of recent volcanic activity and tectonic boundaries (Eurick, 2000; Jasinski, 1994). Mercury is commonly found with gold and silver deposits and can often be used as a geochemical tracer in exploration (Eurick, 2000). Mercury is also found in base metal deposits such as copper, zinc, and lead. Typical concentrations in copper ores are ~0.5ppm and ~9ppm in gold ores (Jasinski, 1994). High mercury concentrations are also observed in fossil fuel deposits where the average mercury concentrations are 0.21ppm in coal and as much as 3.5ppm in crude oil (Jasinski, 1994).

In gold processes, mercury liberation occurs during the thermal pre-treatment (eg, pre-roasting of an ore or concentrate) or mercury is extracted via cyanide leaching (Eurick, 2000; Jasinski, 1994). The resulting soluble mercury-cyanide are co-recovered in the gold-silver product, which must be separated using retorts and condensers (Eurick, 2000). Sufficient mercury is produced

in this way that it could satisfy the current global demand (Salazar & McNutt, 2012). Dedicated mercury operations have mostly diminished on a global scale. Domestically, the McDermitt Mine in Humboldt County, Nevada, was famously the last mercury mine until its closure in November 1990 (Jasinski, 1994). In North America, deposits in Alaska and Nevada are particularly rich with mercury. Internationally, China, Kyrgyzstan, Mexico, Peru, Russia, Slovenia, Spain, and Ukraine are major suppliers of mercury (Salazar & McNutt, 2012).

2.1.6 Mercury Toxicology

Mercury is toxic in any form, but elemental mercury, inorganic mercuric salts, and organic mercury are the most accessible forms to humans. The three differ by their interactions with the body, subsequent biotransformation, and clinical symptoms (Broussard, 2002).

Elemental mercury is liquid at room temperature and possesses a high vapour pressure. It primarily enters the body through inhalation of vapours from which 70-80% of the dosage will be absorbed. By comparison, only 3% absorption occurs dermally and less than 1% of ingested elemental mercury is absorbed by the gastrointestinal (GI) tract (Broussard, 2002). Elemental mercury is also lipid-soluble (fat soluble) which makes it highly mobile in the body. It can pass through the blood-brain barrier and into the central nervous system and the placenta where it will be trapped upon oxidizing. Inorganic alkyl-mercuric salts are water soluble and 7-15% of the dosages can absorb through the skin and GI tract, but it is not lipid-soluble so its mobility is limited (Broussard, 2002). Also, due to its pre-oxidized state, it cannot pass easily through the blood-brain barrier, but its long retention time in the body allows it to accumulate in the central

nervous system and apply its toxic effects. Organic mercury is the most accessible to humans as it is the form that bio-accumulates in aquatic food chains (Mikac, Foucher, Niessen, & Fischer, 2002). Organic mercury is both water and lipid soluble, which will absorb easily in the GI tract and distribute uniformly in the brain, kidney, liver, hair, and skin (Broussard, 2002). Furthermore, organic mercury is able to cross the blood-brain barrier and into the placenta, attributing to neurological symptoms. Methylmercury has a high affinity for sulfhydryl groups and inhibits the activity of certain enzymes which may lead to motor dysfunctions (Broussard, 2002).

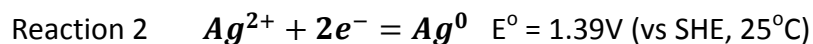
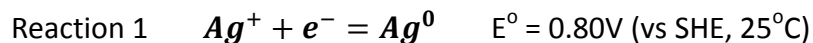
Chronic mercury exposures generally target the central nervous system where they inactivate proteins and enzymes causing degenerative changes, paralysis, and potentially death. Loss of motor skills, sensory malfunctions, and memory disturbances are common, even under acute exposures (Broussard, 2002). In Japan, the consumption of mercury-rich fish between 1953-1960 from contaminated waters resulted in an epidemic of children born with degenerative neurological disorders while the mothers demonstrated no symptoms (Broussard, 2002). In Iraq, between 1971 and 1972, the consumption of bread made from seed grains treated with fungicide containing methylmercury led to the death of 500 people and the hospitalization of 6,000 (Broussard, 2002). Near-complete recoveries from acute exposures are possible since the half-life of all mercury ranges from 40 to 64 days in the body, where excretion occurs mainly through feces (Broussard, 2002).

Naturally, marine mercury concentrations range from undetectable levels to 5.0mg/kg (average 0.2 to 0.5mg/kg), but contaminated freshwaters can contain up to 40mg/kg (Broussard, 2002). During the Japanese epidemic, methylmercury concentrations in the contaminated fish were between 10mg/kg to 30mg/kg (Broussard, 2002). It is estimated that a daily intake of 0.3mg of methylmercury will chronically poison a 70kg adult. Therefore, in the U.S., sales of fish with mercury concentrations exceeding 0.5mg/kg are prohibited. Workers are also protected from vaporous mercury by the threshold established by the American Conference of Government Industrial Hygienists (ACGIH) of $0.05\text{mg}/\text{m}^3$ over a continuous 40 hour work week. For comparison, the immediate volume surrounding an aliquot of elemental mercury can reach up to 2.4ppm mercury vapour (Broussard, 2002).

2.2 Chemical and Physical Properties

2.2.1 Silver Metal Properties

Elemental silver is a transition metal in Group 11 (IB) with an atomic number of 47, atomic weight of 107.87g/mol, melting point of 961.5°C, and a density of 10.49g/cm³ (Butterman & Hilliard, 2004). Natural silver is a mixture of 51.82% Ag-107 and 48.18% Ag-109, which are each stable isotopes (Butterman & Hilliard, 2004). Three main oxidation states of silver can exist where (0) is metallic, (+1) is the common ionic form in compounds due to its lower reduction potential (Reaction 1), and (+2) is less stable (Reaction 2). It has been reported that a (+3) state can exist, but only in the presence of strong oxidants and complexing agents (Butterman & Hilliard, 2004). The half-reaction of this fourth state could not be shown because the thermodynamic data is not available.

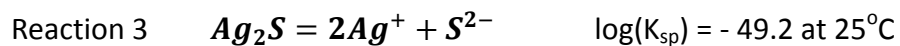


Physically, silver is highly reflective and the most malleable of metals. It is a good conductor of both heat and electricity and does not oxidize easily in the presence of oxygen. However, silver will tarnish in a sulfur environment (“Silver, Properties,” 2013).

2.2.2 Silver Sulfide Properties

Acanthite is the stable form of silver sulfide under atmospheric conditions. Acanthite possesses a monoclinic crystal structure with a density of 7.24g/cm³. Above 177°C, the structure will

change to a cubic argentite structure (“Acanthite, Properties,” 2013). Silver sulfide is virtually insoluble as shown by its dissociation constant in Reaction 3 (“Acanthite, Properties,” 2013).



Synthetic silver sulfide is a fine black powder that has a *flowing* quality which allows it to compact into dense shapes. Silver sulfide demonstrates good electrical conductivity, photoconductivity, and photographic sensitivity.

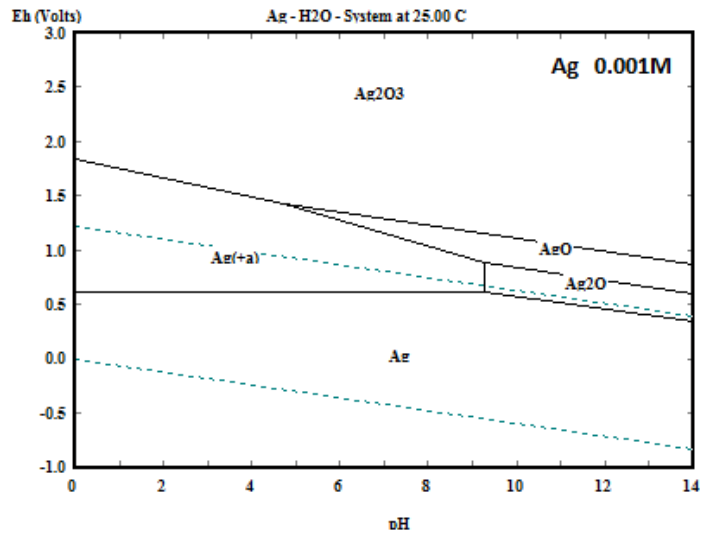
2.2.3 Silver-Cyanide-Sulfur Species

The predominant silver-cyanide complex was investigated through the construction of Pourbaix (Eh-pH) diagrams at varying cyanide concentrations using the HSC[®] software. The results of the HSC[®] calculations were compared to the work by *Xue & Osseo (1985)* for validation. A silver concentration of 0.001M and standard condition (25°C, 1 atm) were initially applied in order to remain consistent with *Xue & Osseo*. Table 1 lists the chemical reactions that were considered and compares the equilibrium constants used by *Xue & Osseo* and HSC[®].

An Ag-H₂O system Eh-pH diagram made from HSC[®] is shown in Figure 2, which closely matches a diagram published by *Xue & Osseo* in Figure 3 under the same conditions.

Table 1: Reduction Reactions for Ag-CN-H2O Eh-pH Diagrams

Reaction	<i>Xue & Osseo</i>	HSC
	log(K)	log(K)
$\text{Ag}^+ + \text{e}^- = \text{Ag}$	13.50	13.51
$\text{Ag}^{2+} + 2\text{e}^- = \text{Ag}$	46.98	47.06
$\text{Ag}_2\text{O} + 2\text{H}^+ + 2\text{e}^- = 2\text{Ag} + \text{H}_2\text{O}$	39.70	39.59
$\text{AgO} + 2\text{H}^+ + 2\text{e}^- = \text{Ag} + \text{H}_2\text{O}$	43.51	44.09
$\text{Ag}_2\text{O}_3 + 6\text{H}^+ + 6\text{e}^- = 2\text{Ag} + 3\text{H}_2\text{O}$	140.04	145.90
$\text{AgCN} + \text{e}^- = \text{Ag} + \text{CN}^-$	-2.16	-2.68
$\text{Ag}(\text{CN})_2^- + \text{e}^- = \text{Ag} + 2\text{CN}^-$	-6.90	-6.80
$\text{Ag}(\text{CN})_3^{2-} + \text{e}^- = \text{Ag} + 3\text{CN}^-$	-7.90	-8.81
$\text{AgCN} + \text{H}^+ + \text{e}^- = \text{Ag} + \text{HCN}$	7.05	6.54
$\text{Ag}(\text{CN})_2^- + 2\text{H}^+ + \text{e}^- = \text{Ag} + 2\text{HCN}$	11.52	11.64
$\text{Ag}(\text{CN})_3^{2-} + 3\text{H}^+ + \text{e}^- = \text{Ag} + 3\text{HCN}$	19.73	18.85



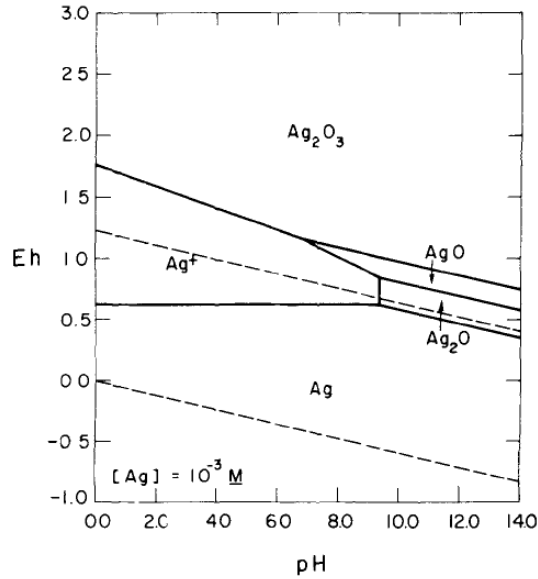


Figure 3: Ag-H₂O System – 0.001M Ag, Xue & Osseo (1985)

Figure 4 shows a Ag-S-H₂O system constructed by HSC[®] where the ratio of silver and sulfur concentrations represent Ag₂S. In the presence of sulfur, an Ag₂S region forms inside the Ag⁰ region at 0 < pH < 12. Comparison to a S-H₂O diagram in Figure 5 confirms that the Ag₂S region overlaps the S⁰ region.

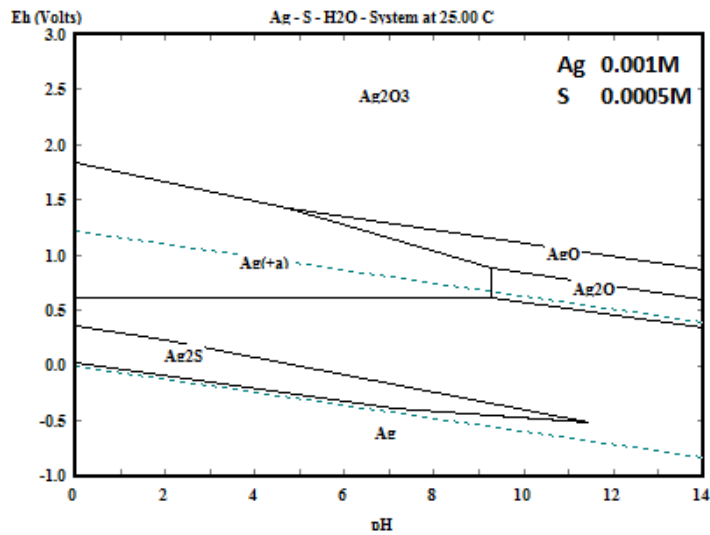


Figure 4: Ag-S-H₂O System – 0.001M Ag₂S, HSC Software

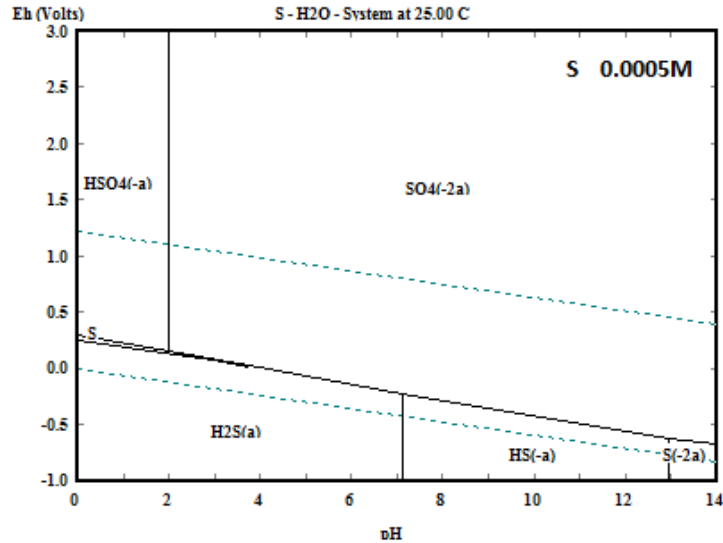


Figure 5: S-H₂O System - 5×10^{-4} M S, HSC Software

Figure 6 shows a Ag-CN-H₂O system at a cyanide concentration of 0.10M (~5g/L NaCN) which is similar to the diagram published by Xue & Osseo in Figure 7. Minor discrepancies are evident, which are attributed to the difference in equilibrium constants used in the two investigations as shown in Table 1. Both diagrams agree, however, that $\text{Ag}(\text{CN})_3^{2-}$ is the predominant silver-cyanide species for alkaline conditions of $\text{pH} > 10$.

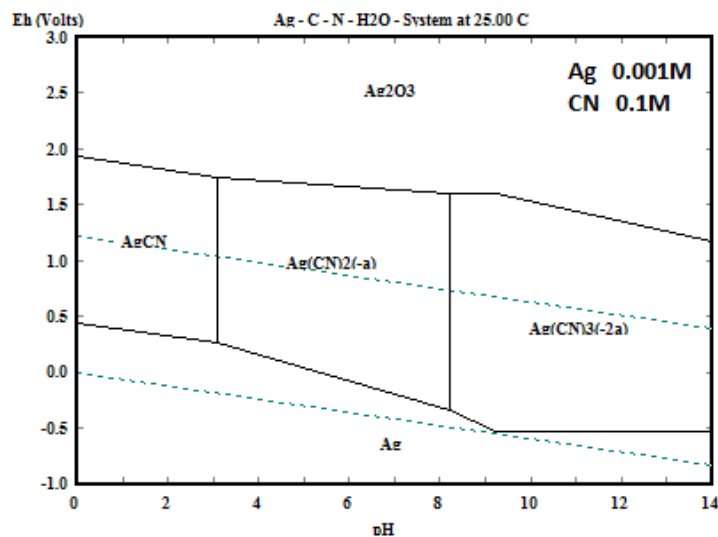


Figure 6: Ag-CN-H₂O System - 0.001M Ag, 0.1M CN, HSC Software

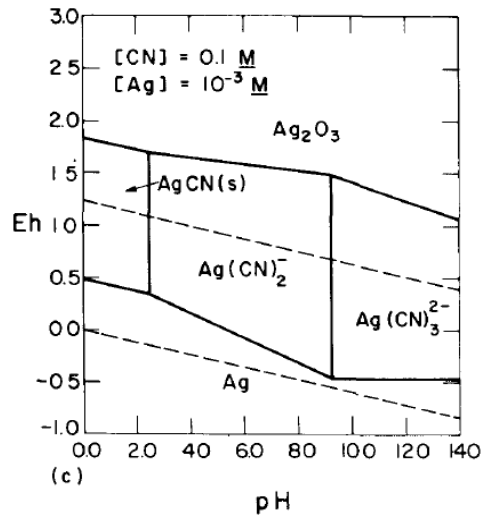


Figure 7: Ag-CN-H₂O System – 0.001M Ag, 0.1M CN⁻, Xue & Osseo (1985)

Li & Wadsworth (1993) and Xue & Osseo (1985) have both reported that $\text{Ag}(\text{CN})_2^-$ will predominate at cyanide concentrations below 0.10M CN⁻. In the current work, however, the Eh-pH diagrams generated by HSC[®] suggests that the transition from $\text{Ag}(\text{CN})_3^{2-}$ to $\text{Ag}(\text{CN})_2^-$ will occur when cyanide concentrations fall below around 0.0097M (~0.5g/L NaCN), as shown in Figure 8, which is much lower than the concentration reported by Li & Wadsworth.

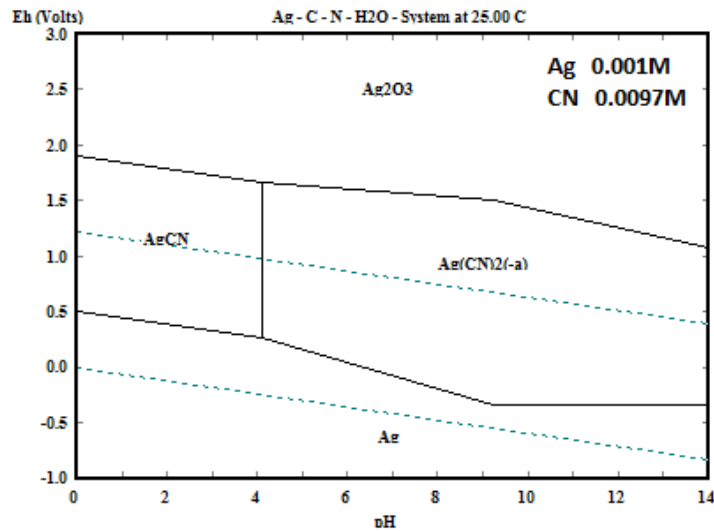


Figure 8: Ag-CN-H₂O System – 0.001M Ag, 0.0097M CN⁻, HSC Software

However, the dimensions of this diagram are still comparable to that of Xue & Osseo's work from a slightly lower concentration 0.001M CN⁻ shown in Figure 9.

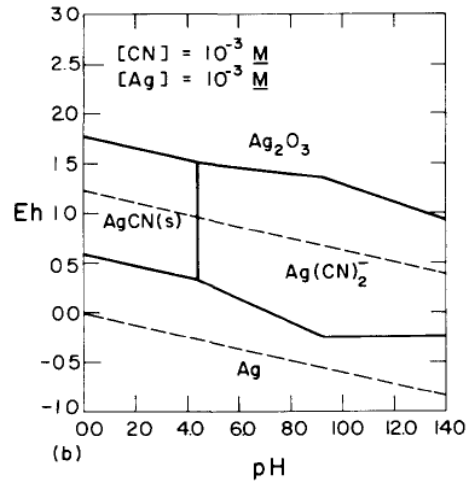


Figure 9: Ag-CN-H₂O System – 0.001M Ag, 0.0010M cyanide, Xue & Osseo (1985)

The Ag-S-CN-H₂O system is shown in Figure 10 which includes the Ag₂S, S⁰, HS⁻(aq), S²⁻(aq), SO₄²⁻(aq), HSO₄⁻(aq) and H₂S(aq) species. This diagram displays that Ag(CN)₃²⁻ will remain as the predominant silver-cyanide species under alkaline conditions when sulfur species are included.

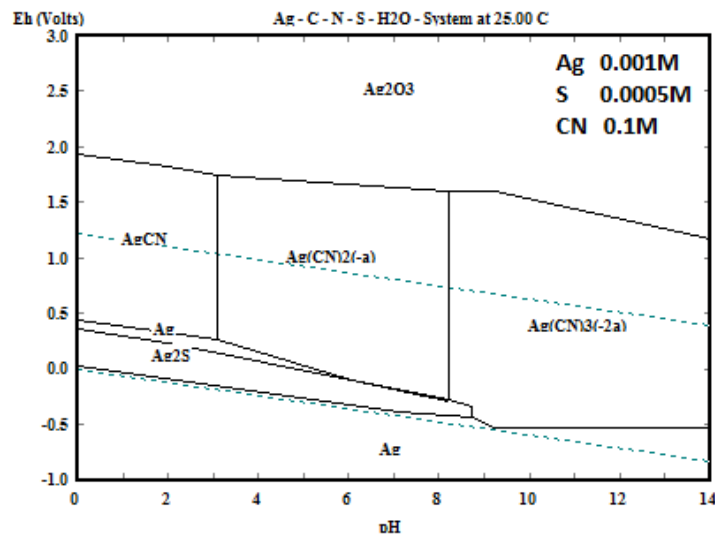


Figure 10: Ag-S-CN-H₂O System – 0.001M Ag₂S, 0.1M cyanide, HSC Software

Finally, an Eh-pH diagram is shown in Figure 11 at the actual typical cyanide and silver concentrations observed in the current experiments which were approximately 0.10g/L NaCN (~0.002M CN⁻) and 2.5ppm Ag (2.5x10⁻⁵M Ag), respectively. This diagram confirms that Ag(CN)₂⁻ is the predominant silver-cyanide species under these conditions. Therefore, Ag(CN)₂⁻ is accepted to be the only silver-cyanide complex.

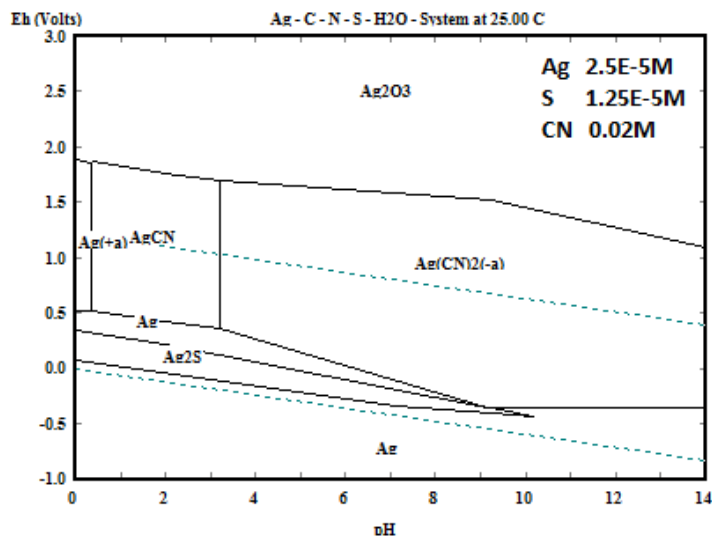
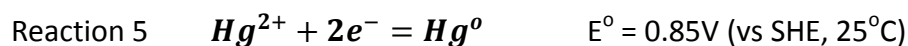
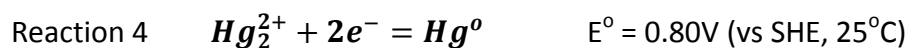


Figure 11: Ag-S-CN-H₂O System - 2.5E-5M Ag₂S, 0.002M CN (baseline conditions), HSC Software

2.2.4 Mercury Metal Properties

Mercury is a transition metal in Group 12 (IIB) on the periodic table with an atomic number of 80 and atomic mass of 200.59g/mol. Seven different isotopes of mercury occur in nature: mercury-196, mercury-198, mercury-199, mercury-200, mercury-201, mercury-202, and mercury 204 ("Mercury, Properties," 2013). The two possible oxidation states are mercurous (Reaction 4) and mercuric (Reaction 5). The stability of mercury's oxidation states is complex, and it has

been reported that Hg_2^{2+} will co-exist in equilibrium during the reduction of Hg^{2+} to Hg^0 (Serruya, Mostany, & Scharifker, 1999).

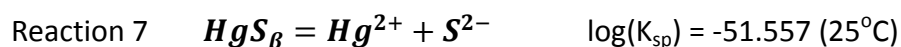
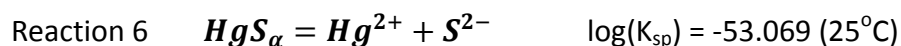


Mercury is a solid below -38.85°C , liquid at room temperatures, and boils at 365.6°C . It is silver-like in colour and has a density of $13.59\text{g}/\text{cm}^3$. Mercury's high electrical conductivity and high surface tension make it appealing to various industrial applications ("Mercury, Properties," 2013).

2.2.5 Mercury Sulfide Properties

Mercury sulfide has a density of $8.18\text{g}/\text{cm}^3$ and can exist as cinnabar and metacinnabar. Cinnabar ($\alpha\text{-HgS}$) is a hexagonal structured mineral that occurs naturally in the earth, which is red in colour. Above 345°C , the structure will change to a black metacinnabar ($\beta\text{-HgS}$) polymorph which possesses a sphalerite crystal structure. Pristine metacinnabar will revert back to cinnabar when cooled, but the presence of certain impurities (~0.3% iron, zinc, selenium) will make the conversion permanent which will not change back, even after cooling (Dickson & Tunnell, 1959).

Both cinnabar and metacinnabar are exceedingly insoluble as seen by the K_{sp} values in Reaction 6 and Reaction 7, respectively. The slightly lower solubility constant associated with metacinnabar indicates that it will be more soluble than cinnabar.



2.2.6 Mercury-Cyanide-Sulfur Species

The stability of mercury-cyanide complexes were investigated by *Penenman & Jones (1961)* and by *Ammar et al (1968)*. Table 2 lists the equilibrium constants of $HgCN^+$, $Hg(CN)_2$, $Hg(CN)_3^-$, and $Hg(CN)_4^{2-}$ as reported by *Penneman & Jones*. It is generally accepted that $Hg(CN)_4^{2-}$ is the most stable species, and higher cyanide-coordination complexes are considered to be uncommon.

Table 2: Mercury-Cyanide Complexes Stability Constants (Penneman & Jones, 1961)

Step-wise Reaction	Log(K) (20°C)	Log(β) (20°C)	Log(β) (30°C)
$Hg^{2+} + CN^- = HgCN^+$	18.0 ± 0.06	18.0 ± 0.06	-
$HgCN^+ + CN^- = Hg(CN)_2$	16.7 ± 0.06	34.7 ± 0.12	33.9
$Hg(CN)_2 + CN^- = Hg(CN)_3^-$	3.83 ± 0.02	38.53 ± 0.14	38.1
$Hg(CN)_3^- + CN^- = Hg(CN)_4^{2-}$	2.98 ± 0.03	41.51 ± 0.17	40.6

The stable species were further investigated using Pourbaix (Eh-pH) diagrams constructed with HSC®. A mercury concentration of 0.001M Hg and standard condition (25°C, 1 atm) were initially applied in order to remain consistent with the silver-cyanide species investigation in section 2.2.3.

The Hg-CN-H₂O system diagram shown in Figure 12 was constructed at a cyanide concentration of 0.1M CN⁻, which shows that Hg(CN)₄²⁻ is predominant for all pH above ~7.2.

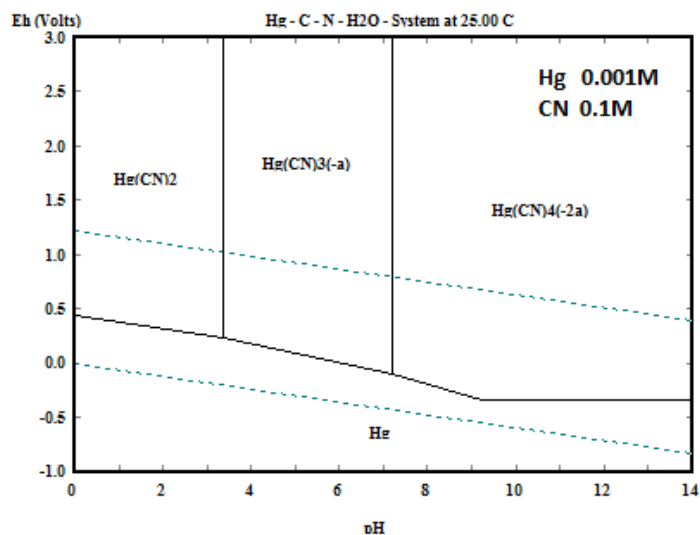


Figure 12: Hg-CN-H₂O System – 0.001M Hg, 0.1M CN / HSC Software

The Hg-S-CN-H₂O diagram is shown in Figure 13 which now includes HgS, S⁰, HS⁻(aq), S²⁻(aq), SO₄²⁻(aq), HSO₄⁻(aq), and H₂S(aq) species. At the same cyanide concentration of 0.1M CN⁻, Hg(CN)₄²⁻ remains as the predominant species above pH~7.2.

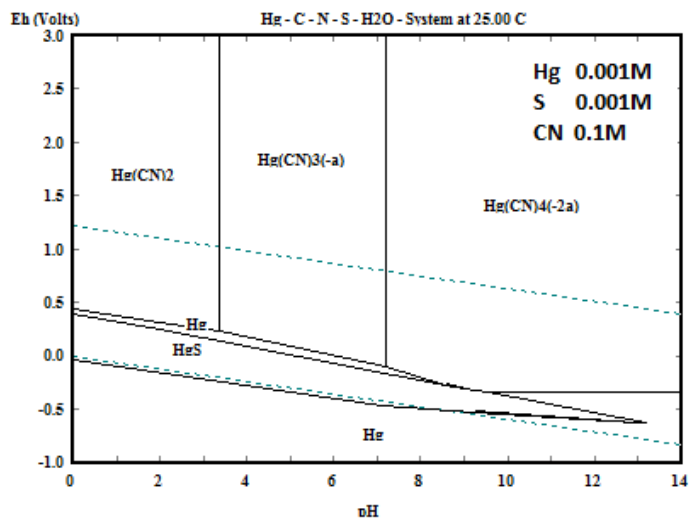


Figure 13: Hg-S-CN-H₂O System – 0.001M HgS, 0.1M CN / HSC Software

In the current study, typical cyanide and mercury concentrations of 0.10g/L NaCN (~0.002M CN⁻) and 5ppm Hg (~2.5x10⁻⁵M Hg) were observed, respectively. Figure 14 shows an Hg-S-CN-H₂O diagram constructed under these parameters, which again shows that Hg(CN)₄²⁻ is the predominant species, but the stable pH region has now changed from ~7.2 to ~8.8 at the lower cyanide concentration.

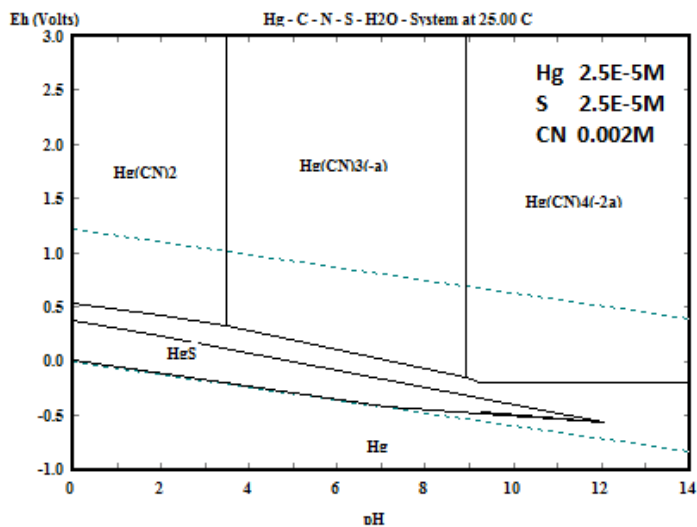


Figure 14: Hg-S-CN-H₂O System – 2.5E-5M Hg, 0.002M CN / HSC Software

2.3 Kinetics Studies

2.3.1 Dissolution Kinetics of Silver Metal

Numerous early studies have shown that the dissolution kinetics of silver in cyanide solutions are superior to gold, but conventional heap leaching data reveals that silver recoveries lag behind gold in actual practice (Hiskey & Sanchez, 1990).

The dissolution kinetics of silver metal in cyanide solutions was studied by *Hiskey & Sanchez (1990)* using an electrochemical rotating disc method. Anodic and cathodic polarization curves of silver oxidation and oxygen reduction were obtained separately from varying cyanide solutions, respectively, and then plotted together to graphically determine the dissolution current (i_d) at the point of intersection.

As seen in Figure 15, the intersections occur at the plateau-regions of the anodic curves at low cyanide concentrations ($<0.001\text{M CN}^-$), which is indicative of cyanide-transport limited kinetics. As cyanide concentrations increase, the intersections occur increasingly on the plateau-regions of the oxygen-reduction curve, indicating that the system changes to an oxygen-transport limited process. The diffusion coefficients of cyanide and of oxygen were reported to be $1.77 \times 10^{-5} \text{cm}^2/\text{sec}$ and $1.60 \times 10^{-5} \text{cm}^2/\text{s}$, respectively (Hiskey & Sanchez, 1990).

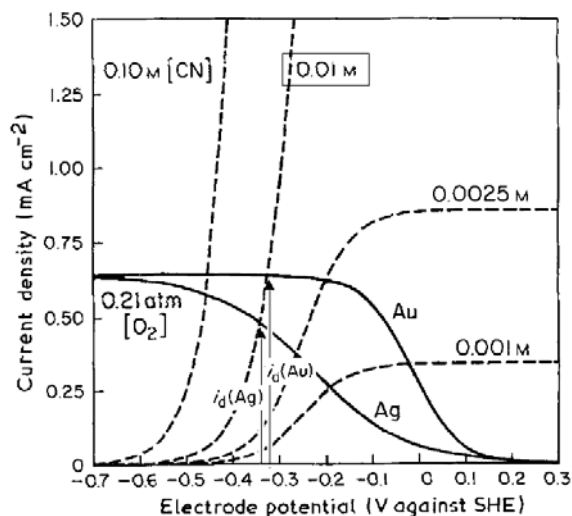


Figure 15: Silver Oxidation & Oxygen Reduction Polarography (Hiskey & Sanchez, 1990)

Hiskey & Sanchez (1990) also discussed the reduction mechanisms of oxygen on silver and gold substrates. Oxygen reduction on silver was explained by the Bridge Model (“bridge”) where a direct 4-electron transfer process occurs to immediately form hydroxides, whereas oxygen reduction on gold was explained by the Pauling Model (“end-on”) where a sequential 2-electron transfer process first forms peroxide intermediate products before reducing further to hydroxide. In the presence of lead (Pb) and bismuth (Bi), however, oxygen reduction on gold surfaces experiences a catalytic effect, which was attributed to a possible conversion from the “end-on” to the bridge mechanism (Hiskey & Sanchez, 1990). Conversely, oxygen reduction on silver changes from the bridge to the end-on mechanism as surface sites are blocked by Pb and Bi (Hiskey & Sanchez, 1990).

The dissolution kinetics of pure silver metal discs was investigated by Li & Wadsworth (1993) using a potentiodynamic rotating disc method in oxygen-free cyanide solutions. Limiting current densities were plotted against the square-root of rotation speeds and cyanide concentrations

to assess the reaction mechanism according to the Levich equation. This equation is later discussed in section 4.4.1. In Figure 16, *Li & Wadsworth* show that in all experiments, linear relationships are observed where the lines cross the origin, which is indicative of a pure cyanide-diffusion limited reaction mechanism (Li & Wadsworth, 1993). Furthermore, the activation energy of the system was determined to be 13.7 kJ/mol using the Arrhenius Rate equation and the cyanide diffusion coefficient to be $1.61 \times 10^{-5} \text{ cm}^2/\text{sec}$ at 24°C .

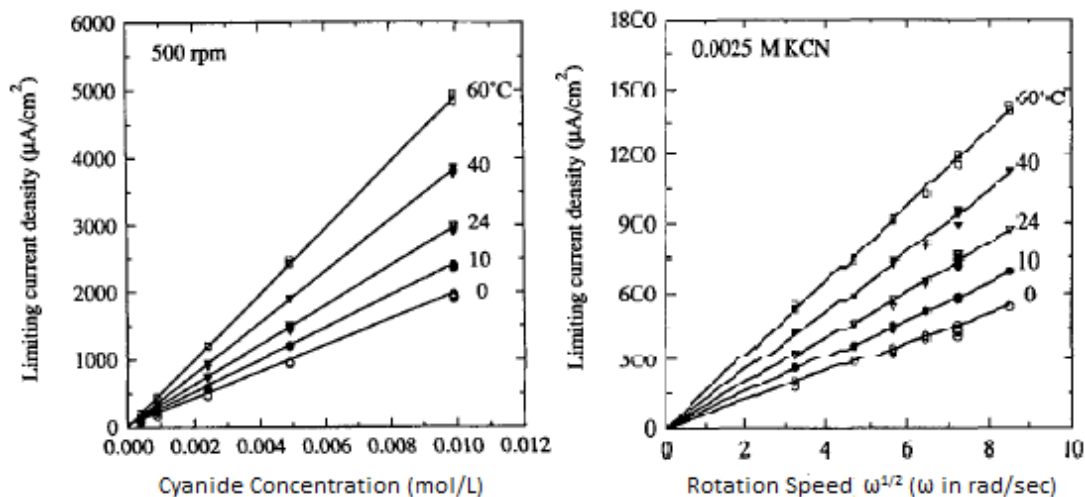
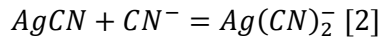


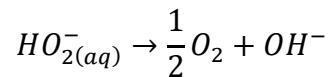
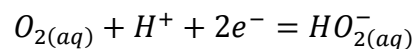
Figure 16: Silver Limiting Current Density vs. $(\text{RPM})^{1/2}$ & Cyanide Concentration (Li & Wadsworth, 1993)

Li & Wadsworth further reported that, in the absence of oxygen, the electrochemical dissolution of silver is a two-stage process as shown in Reaction 8, which consists of a [1] charge transfer step followed by a [2] heterogeneous chemical reaction. It was also reported that the reaction was simultaneously limited by two mechanisms: cyanide-diffusion and charge-transfer. However, the rate-limiting effects of the latter chemical reaction was considered to be negligible (Li & Wadsworth, 1993).

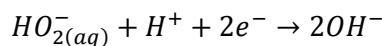
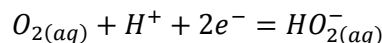


Reaction 8: Silver Dissolution in Two Stage - [1] Charge Transfer, [2] Complex Formation (Li & Wadsworth, 1993)

Wadsworth (2000) conducted an in-depth study of the reduction-pathways of oxygen on silver substrates which followed a similar study reviewed by *Hiskey & Sanchez (1990)*. In this study, two oxygen-reduction pathways were considered where both options were assumed to produce peroxides as an intermediate. A direct 2-electron (Reaction 9) and sequential 4-electron (Reaction 10) processes were thought to occur simultaneously which both contribute to the overall reaction. In the 'direct' process, the resulting peroxide chemically decompose to hydroxide, whereas the 'sequential' process occurs by two 2-electron transfer steps (*Wadsworth, 2000*). These are different from the oxygen reduction models considered by *Hiskey & Sanchez (1990)*, in which one of the chemical pathways assumed that peroxide intermediate production was distinctly absent.



Reaction 9: Direct 2-electron Transfer Pathway of Oxygen Reduction



Reaction 10: Sequential 4-electron Transfer Pathway of Oxygen Reduction

A rotating disc polarography technique was used to develop separate half-reaction polarographic curves of oxygen reduction (cathodic) and silver oxidation (anodic), which were overlapped to study the mixed current densities at the intersections. The possible reduction pathways are modelled in Figure 17, where the k_0 - k_4 route shows the 4-electron pathway, and the k_0 - k_2 and k_0 - k_3 routes show the possible 2-electron pathways (Wadsworth, 2000).

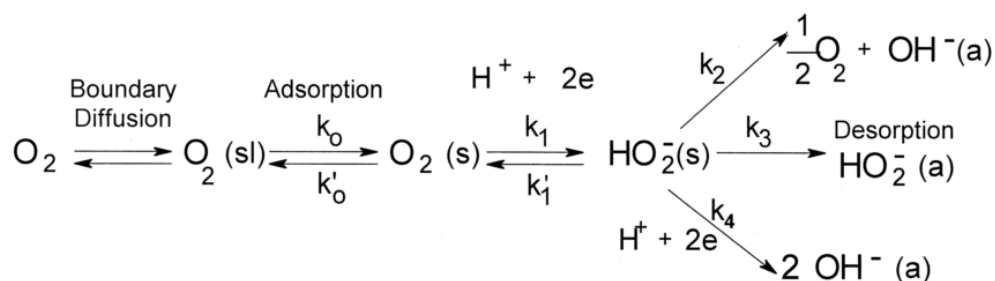


Figure 17: Oxygen Reduction Model of Direct and Sequential Pathways (Wadsworth, 2000)

The current-potential diagram published by *Wadsworth* is shown in Figure 18. Multiple anodic curves were produced at varying cyanide concentrations and compared to a single cathodic curve. The oxygen-reduction curve was separated into the 2-electron and 4-electron process components using a specially derived equation. In this way, it was possible to quantify the contributions of the two mechanisms to the overall redox reaction (Wadsworth, 2000).

Figure 18 shows that for cyanide concentrations around 490ppm NaCN ($>0.01\text{M CN}^-$), the 4-electron process (ie, “2nd wave”) is predominant (between markers *a* and *b*) (Wadsworth, 2000). The sequential 2-electron process (ie, “1st wave”) becomes completely dominant at cyanide concentrations below 25ppm (marker *c*).

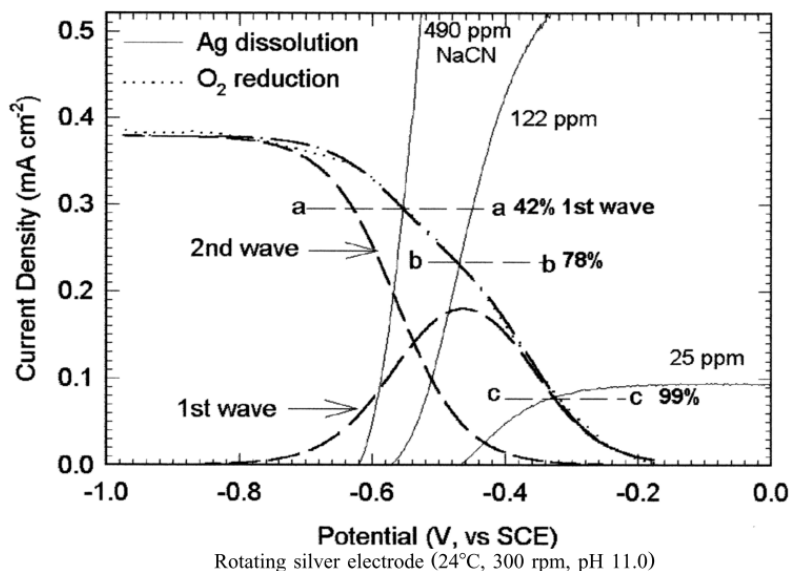


Figure 18: Silver Oxidation vs. Direct and Sequential Oxygen Reduction, Polarography (Wadsworth, 2000)

The experiments were repeated on gold surfaces where the 2-electron process was seen to be predominant at all cyanide concentrations (Wadsworth, 2000).

2.3.2 Dissolution Kinetics of Silver Sulfide

The dissolution kinetics of silver sulfide in acidic ferric chloride and ferric sulfate media were studied by *Dutrizac (1994)* where compressed silver sulfide discs were leached using a rotating disc electrode method. The dissolution current density of the reaction was monitored by analyzing for dissolved silver concentrations by Atomic Absorption Spectroscopy (AAS) from periodically obtained samples. Parabolic leaching rates were observed over leaching times of around 35 hours, which was attributed to passivation caused by a continuously thickening sulfur-rich layer on the surface. The presence of this layer was confirmed by XRD and SEM analyses, which began growing within 2 minutes of leaching (*Dutrizac, 1994*). In response, the

Parabolic Rate Law (Equation 1) was used to determine the parabolic rate constant, k , from the dissolution data, which was used to conduct kinetic studies. This is a different equation than the “Parabolic Leach equation” that is used later in the current work.

$$\left(\frac{\text{wt Ag Leached}}{\text{Area}}\right)^2 = kt$$

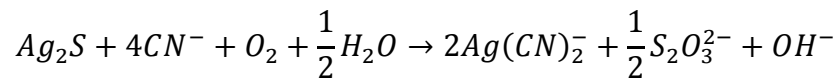
Equation 1: Parabolic Rate Law by (Dutrizac, 1994)

The leaching kinetics of silver sulfide in cyanide was studied by *Luna & Lapidus (2000)* using a stirred reactor method and a silver sulfide concentrate. A shrinking core leaching model was used to interpret the results. Silver extraction rates increased with cyanide concentrations from 0.001M to 0.3M NaCN. It also increased between air (21% O₂) and oxygen (100% O₂) environments, but the change was not proportional to the difference in oxygen contents (Luna & Lapidus, 2000).

It was determined that the reaction was limited by the slow oxidation rate of sulfide ions (Luna & Lapidus, 2000). This was determined by considering two possibilities of sulfur-oxidation routes which were that 1) sulfur oxidation is fast and reaches equilibrium and 2) its oxidation rate is slow compared to oxygen diffusion. The model devised by option (1) produced oxygen-diffusion limited scenarios at every cyanide concentration which disagreed with experimental data while option (2) matched all data under varying cyanide and oxygen concentrations, making it the valid option (Luna & Lapidus, 2000). Extraction rates decreased when the pulp

density was increased. This was attributed to an inadequate rate of oxygen-transfer to supply the increased demand by sulfide ions at the higher solids content (Luna & Lapidus, 2000).

Luna & Lapidus (2000) also published an overall reaction of silver sulfide dissolution in cyanide and oxygen. This was determined through a mass-balance of chemical species from an experiment employing pure Ag_2S in an oxygen-saturated cyanide solution. After a sufficiently long experiment, analyses revealed that thiosulfate ($\text{S}_2\text{O}_3^{2-}$) remained as the only detectable sulfur species. The final balanced equation is shown in Reaction 11.



Reaction 11: Silver Sulfide Dissolution in Oxygenated Cyanide Solutions (Luna & Lapidus, 2000)

Furthermore, Luna & Lapidus identified that peroxides are not formed as an intermediate product during the reduction of oxygen in the reaction of silver sulfide by using $\text{Ca}(\text{OH})_2$ as a sequestering agent. In gold extraction, the presence of Ca^{2+} inhibits the leaching kinetics by precipitating with peroxide as soon as it is formed as an intermediate product (Luna & Lapidus, 2000), as shown in Reaction 12.

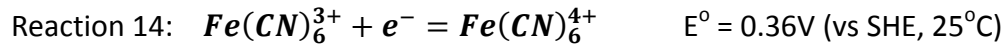
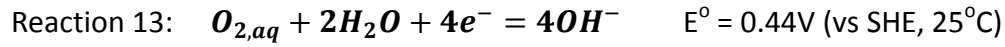


In the case of *Luna & Lapidus*, however, the presence of Ca^{2+} did not affect the extraction rates which indicates that peroxides are not formed (Luna & Lapidus, 2000).

Luna & Sanchez (2003) conducted an electrochemical study of silver sulfide oxidation kinetics in a cyanide solution. The goal was to produce current-potential curves of silver sulfide-oxidation and oxygen-reduction and to investigate the dissolution velocity based on the corrosion current density (I_{corr}) at the intersection. However, for any given potential, the anodic current of silver sulfide decreased with time which was considered to be caused by the accumulation of adsorbed chemical species on the electrode (Luna-Sánchez, González, & Lapidus, 2003). Therefore, a constant-sweep voltammetry method was not used, but a theoretical I-E graph was developed at time-zero by extrapolating the linear regions of the current-time (I-t) graphs, at constant potentials. The working electrode was a polyethylene syringe filled with a paste of 0.3g silver sulfide, 0.7g graphite powder, and a small amount of silicon oil for binding. The total exposed area was 0.0314cm^2 , of which $2.72 \times 10^{-3}\text{cm}^2$ was calculated as the actual silver sulfide area based on densities. Tests were conducted in a de-aerated solution (nitrogen) of 0.3 M cyanide at pH 10.6. A corrosion current of $I_{corr} = 3.0 \times 10^{-6}\mu\text{A}$ was obtained, which was translated into a dissolution rate of $28.5 \mu\text{mol Ag}_2\text{S}/\text{m}^2/\text{sec}$ based on the surface area (Luna-Sánchez et al., 2003). It was further observed that the shape of I-E curves changed with sampling times, which was considered to be caused by the formation of an extra diffusion layer from the accumulation of surface species. Therefore, it was deduced that silver sulfide oxidation was a diffusion-controlled process (Luna-Sánchez et al., 2003).

The dissolution kinetics of silver sulfide in cyanide solutions and ferricyanide as the oxidant was conducted by *Xie (2007)* using a rotating disc method. Despite oxygen's high reduction potential

(Reaction 13), its performance is limited by its low solubility and reactivity (Xie & Dreisinger, 2007). Ferricyanide possesses a lower potential (Reaction 14), but is much more soluble than oxygen which makes it a viable alternative oxidant (Xie & Dreisinger, 2007).



A compressed silver sulfide disc was leached in de-aerated leach solutions (by nitrogen) under varying cyanide and ferricyanide concentrations, pH, and rotation speeds. Dissolution rates were monitored by analyzing dissolved silver concentrations by Atomic Absorption Spectroscopy (AAS) from periodically obtained solution samples. At the baseline condition of 0.5g/L NaCN, 0.5g/L Fe^{3+} as ferricyanide, pH 11.5 and 600rpm a dissolution rate of 21 μ mol $Ag_2S/m^2/sec$ was observed (Xie & Dreisinger, 2007). This was a significant improvement over 13 μ mol $Ag_2S/m^2/sec$ that was observed in a regular air environment. Combining both ferricyanide and air in a dual oxidant experiment produced only a marginally higher rate of 22 μ mol $Ag_2S/m^2/sec$ (Xie & Dreisinger, 2007).

Furthermore, dissolution rates showed a linear relationship to the square-root of rotation speeds which confirmed that silver sulfide dissolution in cyanide-ferricyanide solutions to be a diffusion-controlled process according to the *Levich* equation (Xie & Dreisinger, 2007). The activation energy was calculated to be 6.7kJ/mol using the Arrhenius rate equation on dissolution rates obtained at varying temperatures between 25°C-55°C, which was sufficiently

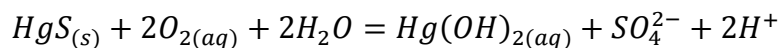
low to satisfy a thermodynamic condition for mass-transport limited reaction (Xie & Dreisinger, 2007). Negligible changes occurred with varying pH between 10 and 12 and a continually decreasing relationship was observed against cyanide concentrations up to 0.5g/L (Figure 60, section 6.1.3). A near-linear relationship was seen against ferricyanide concentrations up to 0.75g/L Fe^{3+} (as ferricyanide). It was deduced that the reaction was diffusion-controlled by both cyanide and ferricyanide, but not hydroxide (Xie & Dreisinger, 2007).

2.3.3 Dissolution Kinetics of Mercury Sulfide

Cinnabar is the most common natural form of mercury sulfide, whereas metacinnabar is usually formed by the precipitation of dissolved anthropogenic mercury in the presence of metallic impurities. As such, they possess different soluble properties and require separate considerations. Kinetic studies of elemental mercury and mercury sulfides in cyanide solutions are scarce. Therefore, kinetic studies of mercury sulfide in water and chloride solutions are used as reference.

The oxidative dissolution rates of cinnabar and metacinnabar in aerated water were investigated by *Holley et al (2007)*. Air was sparged in conical flasks containing mercury sulfide and de-ionized water while oscillated gently at 100rpm on a shaking table. Specific surface areas of the cinnabar and metacinnabar reagents (powders) were determined by N_2 Adsorption to be $1.28 \pm 0.06 \text{m}^2/\text{g}$ and $2.76 \pm 0.04 \text{m}^2/\text{g}$, respectively (Holley et al., 2007). Consistent dissolved oxygen concentrations of $\sim 55 \text{mg/L O}_2$ were achieved from the aeration in every experiment (Holley et al., 2007). Experiments lasted approximately 350 hours and final solutions were

analyzed for sulfate concentrations by Ion-Chromatography (Holley et al., 2007). Sulfate was considered to be a stoichiometric proxy for mercury concentration according to the following reaction (Holley et al., 2007):



Reaction 15: Mercury Sulfide Oxidation in Oxygenated Water (Holley et al, 2007)

However, the direct analysis of dissolved mercury from a select few experiments revealed that mercury and sulfur dissolution rates did not match the ratio suggested in Reaction 15. Voltammetric experiments revealed that, while the *initial* dissociation of HgS correctly follows the reaction, Hg^{2+} ions will re-adsorb onto unreacted cinnabar and metacinnabar surfaces, resulting in a non-stoichiometric net dissolution rate (Holley et al., 2007). Therefore, sulfate was still considered to be a reliable proxy of the true dissolution rate of HgS rather than directly analysing for Hg^{2+} concentrations (Holley et al., 2007). At a solids concentration of 0.10M HgS, cinnabar showed higher dissolution rates than metacinnabar at $2.64\text{-}6.16\mu\text{mol}(\text{SO}_4^{2-})/\text{m}^2/\text{day}$ and $1.20\text{-}1.90\mu\text{mol}(\text{SO}_4^{2-})/\text{m}^2/\text{day}$, respectively. At an increased solids concentration of 0.43M HgS, the sulfate concentration remained the same as the 0.10M HgS experiment, suggesting that dissolution rates are independent of pulp density (Holley et al., 2007).

The dissolution of cinnabar, metacinnabar, and a mercury sulfide precipitate was investigated by Mikac et al (2002) in hydrochloric acids. 1-2mg of mercury sulfide was mixed with 20mL of 1M and 6M HCl solutions in Teflon vials and then gently stirred for 24 hours in a natural air

atmosphere. Mercury concentrations were determined by Cold Vapour Atomic Fluorescence Spectroscopy (CV-AFS). In 1M HCl, all extractions were negligible, but at 6M HCl extractions increased to 90% from the HgS precipitate, 50% from metacinnabar, and 15% from cinnabar. The difference in extractabilities was attributed to the varying compositions of amorphous structures in the three mercury sulfides, where the precipitate was presumed to be the most amorphous and cinnabar to be the most crystalline (Mikac et al., 2002). Experiments conducted at decreasing pulp densities from 0.5g/L to 0.01g/L HgS revealed that extractions increased exponentially when expressed as a percent, as shown in Figure 19.

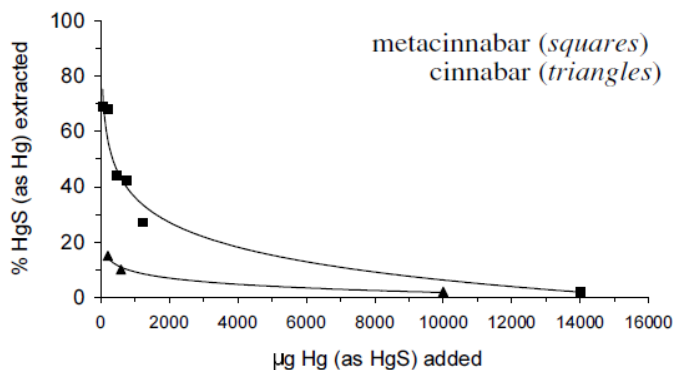


Figure 19: Dependence of Mercury Sulfide Extractability on Solids Added (Mikac et al, 2002)

The extraction of mercury from metacinnabar increased by as much as 70% and the increase from cinnabar was 15%, which also demonstrated that the extractability of metacinnabar is more effected by pulp density than cinnabar (Mikac et al., 2002).

3 Research Objectives

The objective of this work was to study the dissolution kinetics of pure silver sulfide and mercury sulfide in cyanide solutions under atmospheric conditions and to use this information to understand the silver and mercury extraction rates from the Heap Leach Residue.

The experimental technique involved direct leaching of silver and mercury sulfide in oxygenated cyanide solutions rather than the electrochemical methods used in many prior studies. It was hoped that the results of this work would therefore be more directly related to cyanidation practice. Experiments were conducted at varying cyanide concentration, pH, dissolved oxygen concentration, and temperature. The ranges for each variable were selected to be relevant to the Yanacocha operation. The rotating disc electrode and stirred reactor experimental techniques were used for the investigation of the leaching of synthetic silver sulfide and mercury sulfide. The results were then compared to the cyanidation of a Heap Leach Residue obtained from the Yanacocha Mine.

4 Experimental Set-up

4.1 Materials

4.1.1 General Reagents

All reagents used were of analytical grade. Sodium cyanide was obtained from Fisher Science as pellets. Sodium hydroxide solutions were obtained from Sigma Aldrich as two normalized concentrations of 0.1N and 1.0N. Standard 1000mg/L solutions of silver and mercury were also obtained from Sigma Aldrich and diluted to desired concentrations for calibrating the Atomic Absorption Spectroscopy instrument. All solutions were prepared with de-ionized water.

4.1.2 Silver Sulfide Reagent

Synthetic silver sulfide (Premion® brand) of 99.998% purity was obtained from Alfa Aesar. The as-received silver sulfide was black and granular, which were ~1-2mm in diameter and crumbled easily under finger-tip pressure. Acanthite structure was confirmed by XRD analysis and the granules were ground in a mortar-and-pestle to a size passing a 500-mesh screen.

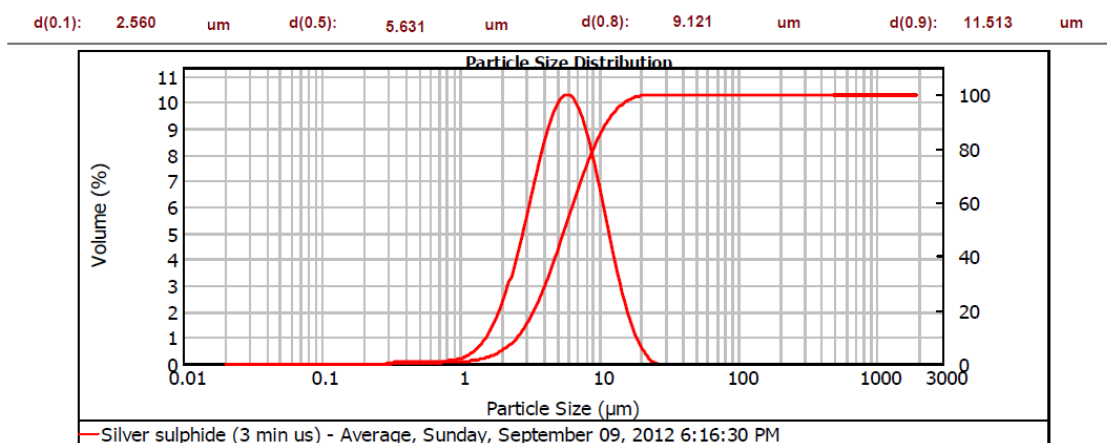


Figure 20: Silver Sulfide Particle Size Distribution (PSA), by Mastersizer®

A particle size analysis (PSA) was conducted by a Mastersizer™ instrument. Figure 20 shows that 80% of the particles were less than 9.8µm in diameter ($P_{80}=9.8\mu\text{m}$, or $9.8 \times 10^{-4}\text{cm}$).

4.1.3 Mercury Sulfide Reagent

Pure synthetic cinnabar ($\alpha\text{-HgS}$, red) and metacinnabar ($\beta\text{-HgS}$, black) mercury sulfide samples were obtained from Alfa Aesar. The as-received cinnabar was a bright-red powder that had a paste-like quality that smeared easily onto surfaces. The as-received metacinnabar was also a fine powder and matte-black in colour. Texturally, it did not smear as easily as cinnabar, making it easier to handle. Both cinnabar and metacinnabar were used directly without further grinding.

A third metacinnabar precipitate ($p\text{-HgS}$, black) was prepared by adding a 10% molar excess of sodium sulfide (Na_2S) into mercuric chloride (HgCl_2) in an alkaline 10g/L sodium cyanide solution. The presence of cyanide ensured that all mercury remained completely dissolved before sulfide was added. An XRD analysis confirmed that the $p\text{-HgS}$ possessed a metacinnabar structure.

4.1.4 Heap Leach Residue Composite

A 2kg composite of Heap Leach Residue was received from the Yanacocha Mine's spent residue. An analysis conducted by Newmont Mining reported that acanthite (Ag_2S) was the only silver mineral present in both the Leach Residue and run-of-mine ore (McComb & Thogerson, 2011). It was reported that 1.8% of the acanthite was exposed and leachable at a particle size of -10 mesh sieve passing (2mm), which increased to 81% when ground to 120µm (Acar, 2010).

Mercury in the Heap Leach Residue was reported to be 69.8% cinnabar (HgS) and 30.2% velikite (CuHgSnS₄) which mostly occupies the rim-regions surrounding sulfide grains and that 37.4% of the mercury is exposed at the analyzed size of -10 mesh (McComb & Thogerson, 2011). The average experimentally determined head assays of silver and mercury in the Leach Residue sample are shown in Table 3 (Comprehensive analysis available in Appendix B). Silver concentrations were highly consistent in every experiment, but considerable variations were observed in mercury concentrations.

Table 3: Experimentally Analyzed Silver and Mercury Concentrations in Leach Residue

	g/t	Variance (%)
Silver	13.87	±1.3%
Mercury	7.94	±18.0%

The received Leach Residue sample from Yanaochca consisted of 2-10 cm wide aggregates. The entire batch was ground using a rod mill and dried in a low-temperature oven at 60°C. Figure 21 shows the results of a dry-sieve particle size analysis, which reveals a P₈₀ particle size of 77µm (ie, 0.0077cm).

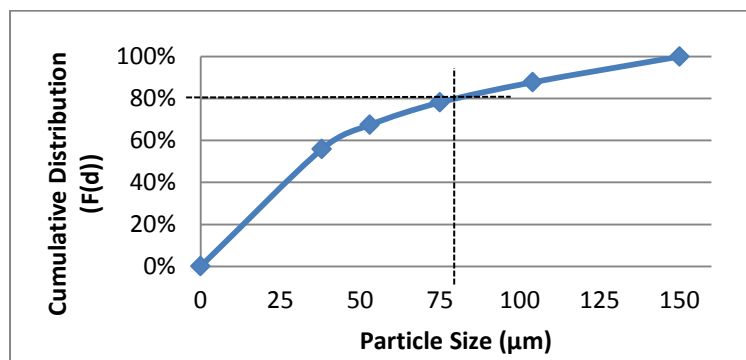


Figure 21: Heap Leach Residue Sample, Particle Size Analysis (PSA)

4.2 Equipment

4.2.1 Compressed Silver Sulfide Discs

Trial experiments revealed that reproducible results could not be obtained when the silver sulfide discs were reused, such that new discs were required for each experiment. Therefore, meticulous care was taken to ensure that the discs were geometrically consistent in each experiment. The matter of 'non-reproducible results' is discussed in more detail later in section 5.2.1.

Approximately 2 grams of silver sulfide powder was pressed in a steel cylindrical mould using a 6-ton hydraulic press into discs measuring 1.925cm in diameter and 1.1 ± 0.1 mm in thickness. Disc densities were $5.75\pm 0.25\text{g/cm}^3$ which is within 76-83% of natural acanthite. The discs were glued onto stainless steel adapters (Figure 22, 3) and encased in Cold Cure[®] epoxy. A thin resin cushion was present between the adapter and the disc to ensure that any electrical contacts were eliminated (Figure 22, #2). After the resin had cured, the casing was trimmed into a uniform shape with an outer diameter of 2.6 ± 0.2 cm.

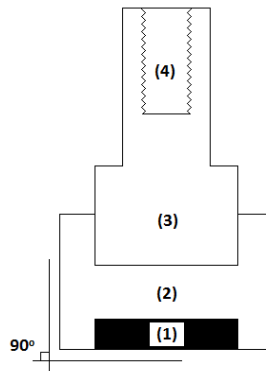


Figure 22: Silver Sulfide Disc Sample (1-silver sulfide disc, 2-epoxy casing, 3-adapter, 4-threading)

The bottom surface was treated with successively finer grades of carbide paper (320, 600, 800, 1200 grit) to expose just one reacting surface of the silver sulfide disc. Finally, the surface was polished to a mirror-like finish on a felt pad using a 1 μ m diamond polishing abrasive. Extensive care was taken to position the disc centrally, to distribute weights evenly, and to maintain a horizontal surface to minimize sources of hydrodynamic interferences.

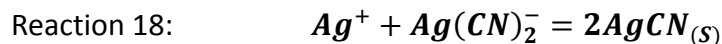
4.2.2 Hardware and Equipment

A constant temperature water bath was assembled by resting an electrical heating element inside a water-filled 15L stainless steel tub. Temperature was controlled by a Traceable[®] temperature controller, which was accurate to $\pm 0.5^{\circ}\text{C}$. Water in the bath was circulated by light mechanical stirring. pH measurements were conducted using a Accumet Basic AB15 pH meter and dissolved oxygen concentrations were measured with the YSI Model 59 meter and YSI 5739 probe. Both of these instruments were calibrated daily.

4.3 Analytical Methods

4.3.1 Titration of Free Cyanide, Colorimetric

Free cyanide concentrations were determined by colorimetric titration using a standard silver nitrate titrant and a p-dimethylaminobenzylidene rhodanine indicator. In this method, an aliquot of the cyanide sample is mixed with an excess of the rhodanine which forms a translucent yellow solution. Then, as the silver nitrate is added, Ag^+ preferentially combines with cyanide forming a colourless $Ag(CN)_2^-$ complex as shown in Reaction 16. After all of the cyanide is consumed, any additional Ag^+ forms an Ag-Rh complex with the rhodanine (Rh) as seen in Reaction 17, which forms a magenta pink. In high excess of Ag^+ , AgCN solids are formed as shown in Reaction 18, resulting in a white suspension (Breuer, Sutcliffe, & Meakin, 2011).



Subsequently, the free cyanide concentration is calculated according to Equation 2 using the known concentration of silver in the titrant, volume of titrant used, and the initial volume of the sample.

$$[CN]_{free} = \frac{2 V_{AgNO_3} [AgNO_3]_{titrant}}{V_{CN\ sample}}$$

Equation 2: Free Cyanide Concentration Calculation for Titration by Silver Nitrate

In this work, titrant of 0.0179M silver nitrate and indicator of 0.4g/L p-dimethylaminobenzylidene-rhodanine dissolved in acetone were used. Silver concentration in the titrant was confirmed in advance by potentiometric titration against a standard sodium chloride (NaCl) solution. Since cyanide concentrations were often very low, the titrant was diluted by 5-50 times in order to increase the volume of titrant used, which assisted with recording volumes more accurately. For the analysis, the titrant was diluted by 5-50 times as necessary in order to assist with volume readings. 5-10mL aliquots of cyanide samples were mixed with 1-2 drops of the indicator and stirred continually with a ½-inch magnetic stir-bar while the titrant was added from a volumetric burette. This method exhibited a 6% coefficient of variance with a mean of 0.101g/L NaCN when tested with 0.10g/L NaCN solutions.

Alternately, a potentiometric titration method is available. However, this is more time-consuming and it is shown in Figure 23 by *Breuer et al (2011)* that the accuracy of colourimetric titration is comparable to that of a potentiometric method.

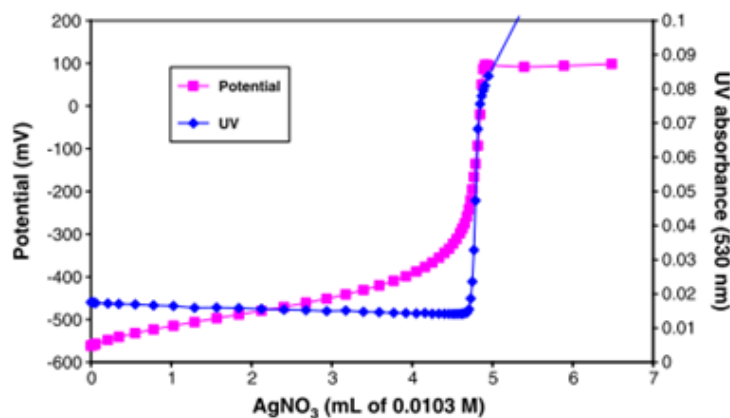


Figure 23: Potentiometric ("Potential") vs. Colorimetric ("UV") Titrations Comparison (Breuer et al., 2011)

4.3.2 Atomic Adsorption Spectroscopy (AAS)

A Varian® AA240 Atomic Absorption Spectroscopy instrument was used to determine silver and mercury concentrations from samples obtained from the pure silver sulfide and mercury sulfide experiments and again for dissolved silver Heap Leach Residue experiments. However, the detection range was inadequate for the analyses of mercury from the Leach Residue. An air-acetylene flame was used with characteristic wavelengths of 328.1nm and 253.7nm silver and mercury detections, respectively. The instrument was calibrated before each use against 4-5 reference solutions of known metal concentrations. Reference solutions were diluted from standard solutions of 1000mg/L silver or mercury. To matrix-match with the leach samples, silver reference solutions were digested in 0.25g/L NaCN and mercury in 1.0g/L NaCN, both at pH>11. However, it was found that cyanide and pH variations did not observably affect the detection accuracies. The coefficient of variance for silver analysis was between 1-3% when assessed with 1, 2, 3, and 4mg/L Ag solutions. Mercury demonstrated a coefficient of 5% when assessed with a 5mg/L Hg solution. Approximately 4-5mL samples were required for each AAS analysis. Samples obtained for silver analysis from the rotating disc experiments were diluted by 12.5 times in order match the optimum detection range of AAS for silver. Dilution was unnecessary for samples obtained for mercury analysis since its optimum detection level is much higher than that of silver.

4.3.3 Cold Vapour Atomic Adsorption (CVA-Hg)

Cold Vapour Atomic Adsorption (CVA-Hg) was used for the determination of mercury in samples from the Heap Leach Residue experiments. CVA-Hg is a highly sensitive method of

detecting low concentrations of mercury. The analyses were conducted by Inspectorate Labs, a certified assay lab in Richmond, B.C.

4.3.4 Metallographic Techniques (SEM/EDS, XRD, XPS)

Secondary Electron Micrograph (SEM) and Energy Dispersive X-Ray Spectroscopy (EDS) were used to conduct elemental analyses of minerals and to view surface structures (Hitachi S-3000N SEM). X-Ray Diffraction (XRD) was used to characterise crystal structures of solid samples (Rigaku Multiflex X-Ray Defractometer).

X-ray Photoelectron Spectroscopy (XPS) was used to determine the elemental composition of a thin product-layer that was suspected to grow on the surface of silver sulfide discs (Leybold Max200 X-ray Photoelectron Spectroscopy). The elemental mapping capability of SEM/EDS was inadequate for this task due to its deeper energy penetration which caused it to detect signals from inside of the disc rather than from the surface. By contrast, XPS uses focused x-rays to photoionize individual atoms at depths on the order of 10Å (0.1nm), which results in a higher detection resolution. Due to its precise energy distribution, it is also capable of identifying valence states of atoms (Ohya, Inai, Nisawa, & Itoh, 2008). XPS was used successfully to determine the surface species of leached arsenopyrite minerals by *Costa et al (2002)* (Costa, Botelho do Rego, & Abrantes, 2002).

4.4 Experimental Methods

4.4.1 Silver Sulfide - Rotating Disc Experiment

Rotating Disc Experiment Theory

In rotating disc experiments, mass transport to the disc's surface is uniform and the parameters are well defined making it possible to attain highly reproducible results in mass transport-controlled systems (Gileadi, 1993). This method is frequently used in electrochemical studies of solid metals, but due to its simplicity it can be adapted to chemical experiments for a wide range of materials, provided that the sample can be shaped into uniform discs. If the solution flow around the disc is laminar, the diffusion-limited current density, i_L (C/s·cm²), can be explained using the *Levich* equation shown in Equation 3 where n is the number of electrons transferred (mol e⁻), F is Faraday's constant (96,485 C/mol e⁻), D is the diffusion coefficient (cm²/s), ν is the kinematic viscosity of the solution (cm²/s), ω is the angular velocity of the disc (radians/s), and C_A^o is the bulk concentration of reagent (mol/L) (Gileadi, 1993).

$$i_L = 0.62 \cdot nF \cdot D^{\frac{2}{3}} \cdot \nu^{-\frac{1}{6}} \cdot \omega^{\frac{1}{2}} \cdot C^o$$

Equation 3: Levich Equation, Limited Current Density of Rotating Disc Electrode (Gileadi, 1993)

Figure 24 illustrates the dissolution mechanism of a rotating disc sample. If the transport of reagent A through a solution film of thickness δ is rate-limiting, then i_L will be a function of the diffusion coefficient, D_A , and concentration C_A^o . In non-electrochemical experiments, the rate is more conveniently expressed as a molar flux of reagents towards the disc, J_A (mols of A /s·cm²). This is now stoichiometrically proportional to the outward dissolution rate of product D , J_D

(mols of D/s·cm²), according to the general reaction $aA + bB = cC + dD$. The overall expression for J_D is shown in Equation 4.

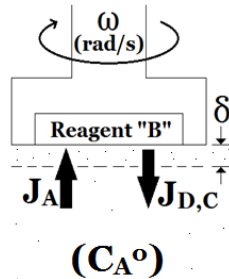


Figure 24: Rotating Disc Leaching Diagram

$$J_D = J_A \cdot \left(\frac{d}{a}\right) = 0.62 \cdot D_A^{\frac{2}{3}} \cdot \nu^{-\frac{1}{6}} \cdot \omega^{\frac{1}{2}} \cdot C_A^o \cdot \left(\frac{d}{a}\right)$$

Equation 4: Levich Equation, Molar Flux Rate of Dissolving Disc

In chemical experiments, it is more accurate to measure the dissolution rate of products from the disc than it is to monitor the changes in the bulk concentration of reagent A. Therefore, using Equation 4, the rate-limiting effects of the reagent (A, B) can be investigated by studying the dissolution rate of the products (D, C).

In order to maintain laminar flow, the Reynold's number must remain below a critical value of $N_{Re} = 10,000$. This is accomplished by adjusting the rotation speed (ω , rad/sec) according to Equation 5, where r (cm) is the radius of the disc, ν is the kinematic viscosity of the solution (cm²/s), and ω is the rotation velocity (rad/s) (Gileadi, 1993). For an assumed ν of 0.01cm²/s

(dilute aqueous solutions) and a disc radius of 1.3cm (as used in the current work), a maximum velocity of 5600rpm is permitted for laminar conditions.

$$N_{Re} = \frac{\omega r^2}{\nu} < 10,000$$

Equation 5: Critical Reynold's Number for Laminar Flow Around a Rotating Disc

The lower rotation velocity limit is breached when the mass-transport rate through the rotational diffusion layer is low compared to natural convection that would occur in a stagnant solution. This is generally considered to be 400rpm for small discs (Gileadi, 1993).

Experimental Set-up

1000mL polyethylene beakers were used as leaching vessels for rotating disc experiments with silver sulfide. This plastic material was considered to be less susceptible to reacting with the reagents. To prepare the leach solutions, a sufficient amount of sodium hydroxide was first added to 500mL of de-ionized water to raise the pH to ~9.5. As the vessel sat in a preheated water bath, sodium cyanide was added and gentle mechanical stirring was applied for 20 minutes while further sodium hydroxide was added to raise the pH to the desired level. Experiments were initiated once the silver sulfide discs entered the solution while set in its rotating motion. The vessels were left uncovered to maximize the solution's access to air.

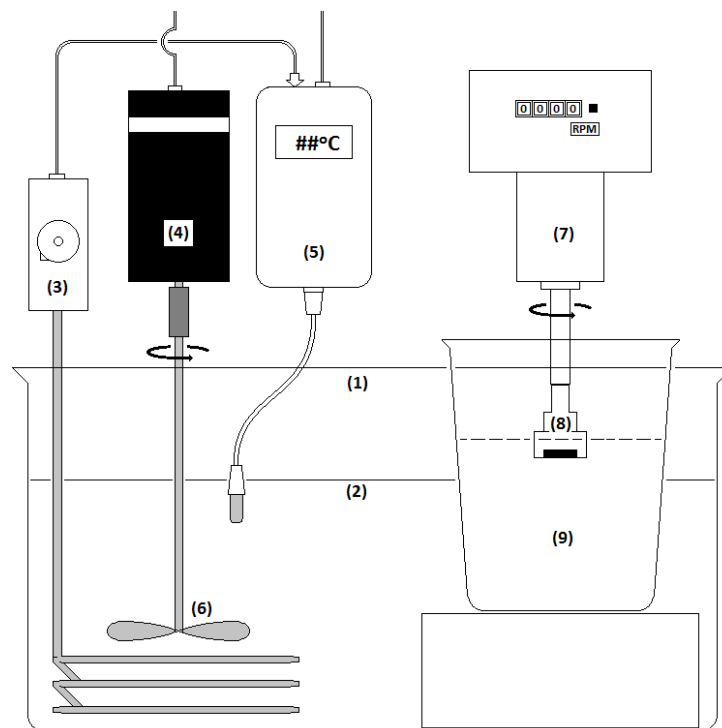


Figure 25: Rotating Disc Experiment Set-up (1-heated water bath, 2-water level, 3-heating element, 4-bath water stirrer, 5-temperature controller, 6-45° flow blade, 7-Disc Rotator, 8-silver disc sample, 9-reactor vessel)

For experiments employing oxygen and nitrogen environments, pure nitrogen or oxygen gases were sparged through a fine gas-dispersion tube for 20 minutes during the stirring time in order to achieve maximum dispersion. The gases were continually fed during the experiments and the vessels were covered with a plastic wrap to prevent solution losses from splashing caused by the bubbling effect. The bubbles were sufficiently small and feed-rate low that hydrodynamic interferences were not experienced.

Experiments lasted 2 hours where 5mL samples were obtained at 5, 10, 15, 20, 25, 30, 40, 60, and 120 minutes. The total acquired volume was large, but dissolution rates were calculated from only the initial 25 minutes, by which time less than 5% of the volume was removed, which

did not significantly affect the rate calculations. Dissolved oxygen concentrations and pH were monitored periodically and sodium hydroxide was added as required.

4.4.2 Mercury Sulfide – Stirred Reactor Experiment

1500mL Pyrex glass beakers were used for all stirred reactor experiments with mercury sulfide. The heavier glass construction made these more stable under vigorous mixing. However, glass (silica) is soluble in alkaline solutions which consumes hydroxides and affects the stability of pH over time. To compensate, the baseline pH for mercury sulfide and Leach Residue experiments was set at 11.5 to ensure that decrease in pH over time was small compared to the initial level. pH was also monitored frequently and hydroxide added as required.

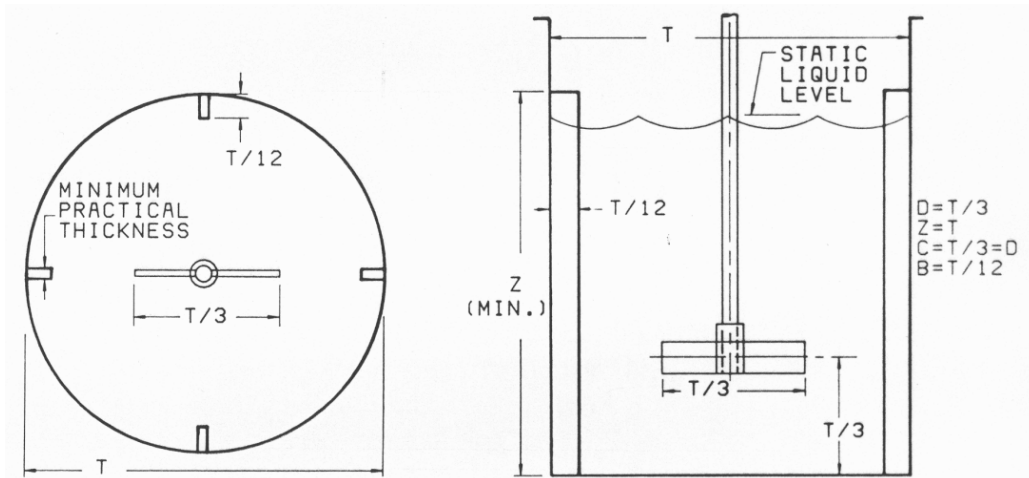


Figure 26: Leach Vessel Geometry (*"Mixing and Mass Transfer in Hydrometallurgy"*, presentation by Dr. David Dixon)

All glass beakers were fitted with four 1cm wide polycarbonate baffles according to the dimensions suggested in Figure 26. Mixing blades were 45°-pitched, flow-type and 1.75 inches

in diameter. The blades were positioned $\frac{1}{2}$ " from the bottom of the vessels and spun at 1000rpm to ensure that all solids remained fully suspended.

To prepare the leach solutions, a sufficient amount of sodium hydroxide was first added to 1000mL of de-ionized water to raise the pH to ~ 11 . As the vessel sat in the preheated water bath, sodium cyanide was added and gentle mechanical stirring was applied for 20 minutes while further sodium hydroxide was added to raise the pH to the desired level. Experiments were initiated once the mercury sulfide was added. Initially, high evaporative losses were observed due to the vigorous mixing. Therefore, the vessels were covered with loose-fitting rubber lids that provided sufficient air access and reduced evaporative solution losses.

For experiments employing nitrogen and oxygen, the gases were fed into the solution for 20 minutes through a $\frac{1}{4}$ " polyethylene tube during the initial stirring time to maximize gas saturation. A fine gas-dispersion tube was not used because sufficient mixing was provided by the vigorous stirring action. The gases were continually fed from under the mixing blades during the experiments. The experiments lasted 48 hours and samples were obtained at 6, 12, 24, 36, and 48 hours, which were passed through $0.45\mu\text{m}$ syringe filters to remove solids. Dissolved oxygen concentrations and pH were periodically monitored and cyanide concentrations were determined by colorimetric titration.

4.4.3 Leach Residue – Stirred Reactor Experiment

For the leaching experiments with Heap Leach Residue (Leach Residue), 1000mL Pyrex glass beakers were used, which were fitted with baffles in the same manner as the mercury sulfide experiments in section 4.4.2.

The preparation of leach solutions was synonymous with the mercury sulfide experimental procedures, except that the solution volumes depended on what would produce a 10wt% pulp density. The Leach Residue sample was separated into 52g to 56g portions by the cone-and-quarter method, which required between 420mL and 450mL of leach solutions. Stirring was applied at 1200rpm to ensure that all solids remained in full suspension.

Experiments lasted 48 hours and samples were obtained for both silver and mercury analyses. Sample volumes of 5mL were obtained for silver analysis at 1, 2, 4, 6, 12, 24, 36, and 48 hours and additional 5mL samples were obtained for mercury analysis at 6, 12, 24, 36, and 48 hours. The samples were filtered through a 6µm inline filter and again through a 0.45µm syringe filter to remove all solids. At the end of the leaching test, the remaining solids were separated from the filtrate through 6-inch diameter #42 filter papers, washed in 4 bed-volumes of deionized water, dried at 40°C for twelve hours, and then submitted for analysis of silver and mercury contents to Inspectorate Lab (certified analytical lab in Richmond, B.C.). Unlike the silver sulfide and mercury sulfide experiments, an equal volume of fresh leach solution was added to replace the obtained samples. This was done to maintain high solution levels to prevent excessive

splashing which would result in high evaporative losses. Extractions of silver and mercury were calculated based on the individual head assays of each experiment.

5 Experimental Results

5.1 Silver Metal Results

5.1.1 Silver Rotating Disc - Validation of Method

Rotating disc experiments were conducted with pure silver metal in order to validate the experimental method by cross-referencing with past published results. Silver discs were cut-out from 99.999% pure silver bullion and prepared for rotating disc experiments in the same manner as silver sulfide discs as outlined in section 4.2.1. Two experiments were conducted at 0.5g/L NaCN, pH 11.0, 25°C, and 600rpm. The leach vessels were not covered to allow sufficient access to air.

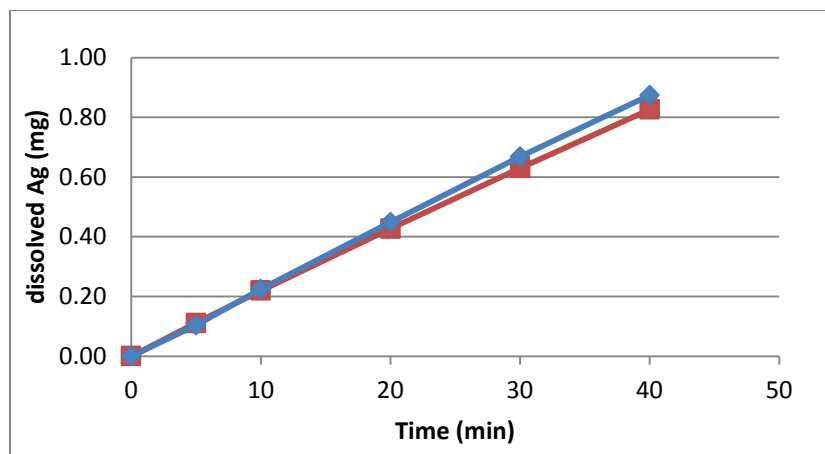


Figure 27: Silver Metal Dissolution vs. Time (0.5g/L NaCN, pH 11.0, 25°C, 600rpm, air)

The results in Figure 27 show a high level of reproducibility and linearity up to, and exceeding, 40 minutes. From the slopes, the average dissolution flux was calculated as $41.9\mu\text{mol Ag}/\text{m}^2/\text{sec}$. This is comparable to the $50.8\mu\text{mol Ag}/\text{m}^2/\text{sec}$ that was obtained from the

polarographic curve published by *Hiskey & Sanchez* in Figure 15. This confirms that the current set-up is consistent and reliable.

5.2 Silver Sulfide Results

5.2.1 Silver Sulfide & Non-linear Dissolution Rates

Figure 28 shows non-linear dissolution rates that were obtained from three experiments conducted at 0.10g/L NaCN, pH 10.5, 25°C, and 600rpm in an air environment for 2 hours. The rate is initially linear, but gradually decreases between 30-60 minutes until severely decreased slopes are attained between 60-120 minutes. It was also observed that reproducible results could not be obtained from a disc when it was reused. In some cases, as much as 40% of the disc's thickness was removed to expose a fresh surface, but the resulting dissolution rates were lower and non-linear. Therefore, new discs were used for each experiment.

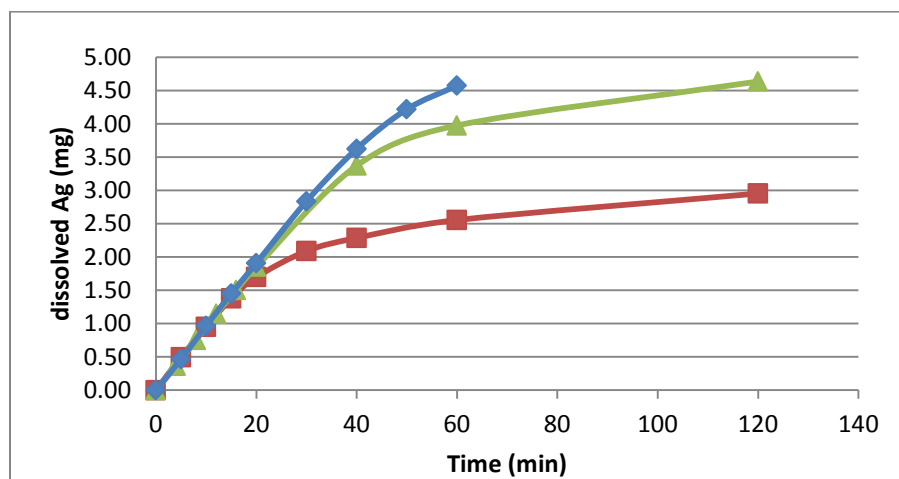


Figure 28: Reproducible Silver Sulfide Dissolution vs. Time - 2 hour results (0.10g/L NaCN, pH 10.5, 25°C, 600rpm, air)

It is hypothesized that the decreasing dissolution rates are the result of saturation caused by dissociated sulfide ion which suppresses the forward reaction. It is also believed that the silver sulfide particles are modified by the re-adsorption of product species which makes the discs less reactive when re-used. If these species are sufficiently mobile, they may infiltrate the

porous channels in the disc and affect the inner structure of the discs as well. The rate-limiting effect of sulfide-saturation during silver sulfide extraction is reported by *Luna & Lapidus (2000)*, and the time-dependent adsorption of chemical species on silver sulfide electrodes and its inhibiting effects on dissolution were discussed by *Luna & Sanchez (2003)*. This is further discussed in section 6.1.4.

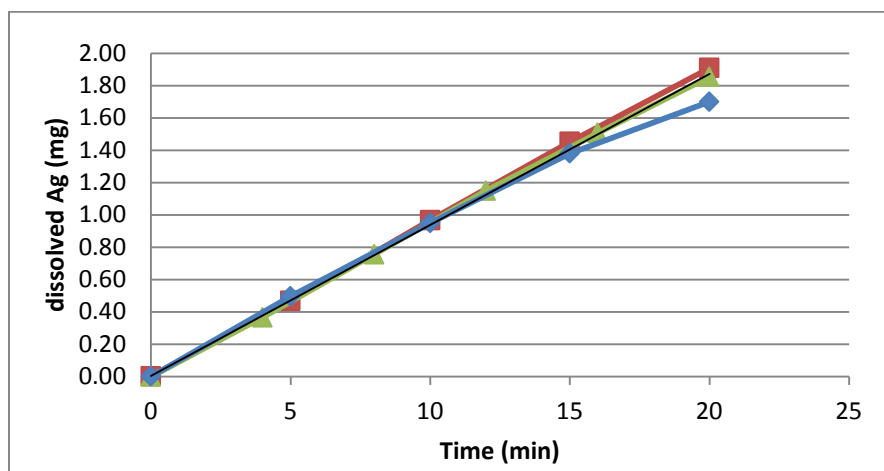


Figure 29: Reproducible Silver Sulfide Dissolution vs. Time, initial 20 minutes (0.10g/L NaCN, pH 10.5, 25°C, 600rpm, air)

Therefore, only the initial 20-30 minutes of leaching has been considered for calculating the dissolution rates. This is shown in Figure 29, where highly reproducible slopes are observed with an average dissolution rate of $23.9 \mu\text{mol Ag}_2\text{S}/\text{m}^2/\text{sec}$ and a coefficient of variance of 7.4%. This is comparable to a rate of $28.5 \mu\text{mol Ag}_2\text{S}/\text{m}^2/\text{sec}$ observed by *Luna & Sanchez (2003)* and $12.5 \mu\text{mol Ag}_2\text{S}/\text{m}^2/\text{sec}$ by *Xie (2007)*. All subsequent kinetic data were attained from the initial 20-30 minutes of the experimental data.

5.2.2 Silver Sulfide Particle Size Distribution and Disc Treatment

The particle size of silver sulfide and the coarseness of aggregates in the metallurgical polishing solutions significantly affected the dissolution rates. Three combinations were tested: 1) 500-mesh passing silver sulfide particles & 6 μ m polish, 2) 400-mesh passing & 1 μ m polish, 3) 500-mesh passing & 1 μ m polish. It was observed that at 400-mesh passing, silver sulfide particles of $P_{80}=16\mu$ m were produced, and 500-mesh produced $P_{80}=9.8\mu$ m. Both of the 1 μ m and 6 μ m polishing solutions contained diamond abrasives. The results of all three combinations are shown in Figure 30.

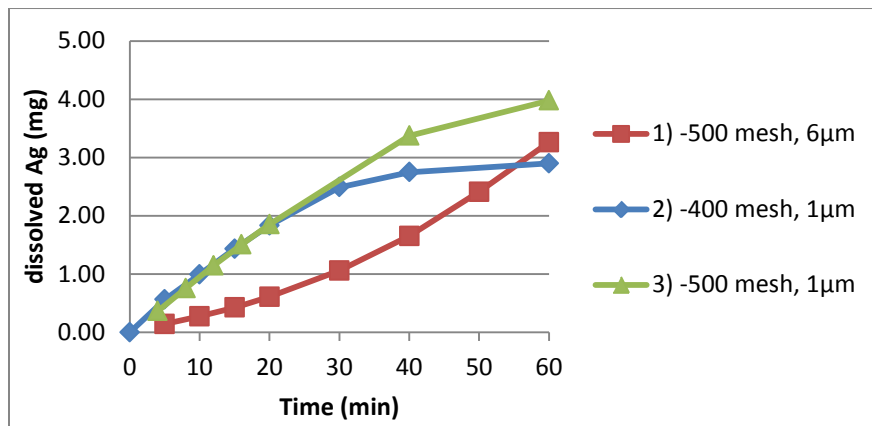


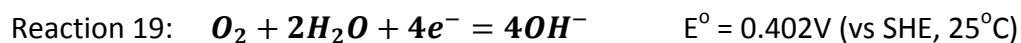
Figure 30: Silver Sulfide Dissolution vs. Time, Various Surface Treatments

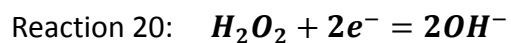
From discs made with the 9.8 μ m silver sulfide powder and polished with the coarse 6 μ m solution, convex dissolution curves were observed (Figure 30, combination 1). Repeated experiments produced similar shapes, but were inconsistent in scale. It is hypothesized that, since the two particles are similar in size, the coarse polishing aggregates stripped the silver sulfide particles from the surface rather than shearing them to flatness. This would result in a microscopically rough texture that would encourage hydrodynamic interferences.

Either of the discs made from the 9.8 μm or 16 μm silver sulfide demonstrated desirable and similar dissolution rates when polished with the 1 μm solution (Figure 30, combinations 2 & 3). A small difference, however, was that the initial linear region endured longer when the finer 9.8 μm silver sulfide particle was used (Figure 30, combination 3). This may be because the smaller particles are able to achieve a denser structure. Therefore, all successive discs were made from the $P_{80} = 9.8\mu\text{m}$ silver sulfide powder (-500 mesh) and polished with the 1 μm diamond solution.

5.2.3 Silver Sulfide Dissolution Kinetics Results

In the rotating disc study of silver sulfide, a baseline leaching condition of 0.10g/L NaCN, pH 10.5, 25°C, 600rpm, and air atmosphere was selected, which approximates the heap leach conditions at the Yanacocha Mine. Dissolution rates were investigated at varying cyanide concentrations, pH, rotation speeds, oxygen concentrations, and temperatures. Dissolved oxygen concentrations were measured in each experiment, which was consistent to within 5.5-6.5mg/L O_2 under the natural air environment. The application of ferricyanide and hydrogen peroxide as alternative oxidants were also investigated. Ferricyanide was used successfully by *Xie (2007)* to improve the dissolution kinetics of silver sulfide. Hydrogen peroxide is a powerful oxidant with a much higher reduction potential than oxygen, as compared in Reaction 19 and Reaction 20. The array of leaching conditions is shown in Table 4, consisting of 18 variations.





$E^\circ = 0.937V$ (vs SHE, 25°C)

Table 4: Conditions of Silver Sulfide Rotating Disc Experiments

baseline					
Sodium Cyanide (g/L NaCN)	0.10g/L	0.025g/L	0.05g/L	0.15g/L	0.25g/L
Rotation Velocity (RPM)	600rpm	300rpm	400rpm	800rpm	1000rpm
Oxygen Content	Air	Oxygen	Nitrogen		
pH	10.5	11.5	11.0		
Temperature (°C)	25°C	35°C	30°C	20°C	
Additional Oxidants	-	Ferricyanide	Hydrogen Peroxide		

Figure 31 shows a linear relationship between the dissolution rates of silver sulfide and cyanide concentrations.

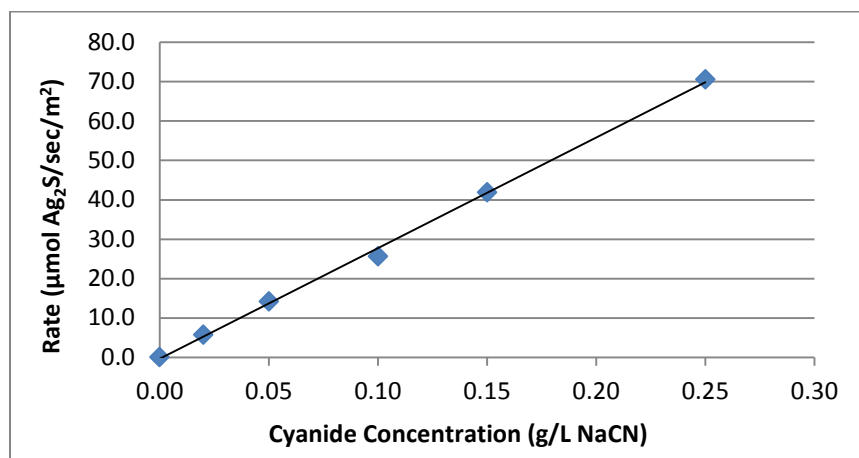


Figure 31: Silver Sulfide Flux vs. Cyanide Concentration (0.025g/L, 0.05g/L, 0.10g/L, 0.25g/L NaCN pH 10.5, 25°C, 600rpm, air)

Likewise, Figure 32 shows a linear relationship between the dissolution rates and the square-root of rotation speeds. The y-intercepts are nearly zero in both figures, which is characteristic of a *pure* mass-transport control according to the Levich equation (Equation 4, section 4.4.1). Had the intercept been greater than zero, a mixed-control would be suspected.

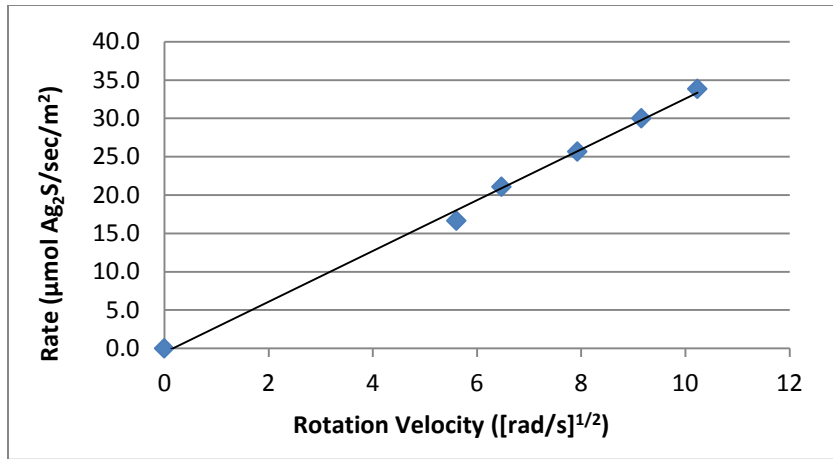


Figure 32: Silver Sulfide Flux vs. Square Root Rotation Speed (300, 400, 600, 800, 1000rpm - 0.10g/L NaCN, pH 10.5, 25°C, air)

Figure 33 shows a nonlinear relationship between the dissolution rates and oxygen concentrations. A more significant change occurs when the oxygen concentration decreases under nitrogen-sparging compared to increasing the oxygen concentration by oxygen-sparging. However, the overall influence of oxygen on silver sulfide dissolution is small, indicating a low dependence.

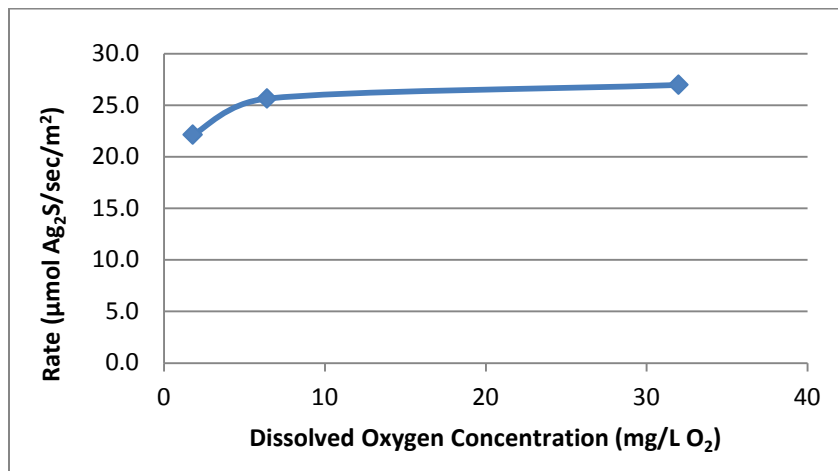


Figure 33: Silver Sulfide Flux vs. Dissolved Oxygen Concentration (N₂, air, O₂ - 0.10g/L NaCN, pH 10.5, 25°C, 600rpm)

The dissolved oxygen concentrations were measured as 1.8mg/L O₂ and 6.4mg/L O₂ under nitrogen-sparging and unsparged air atmosphere, respectively. The dissolved oxygen concentration under oxygen-sparging exceeded the detection limit of the instrument (>20mg/L O₂), so it was calculated using the oxygen diffusion model by *Tromans* (Equation 6) to be 32.4mg/L O₂.

$$c_{\text{aq}} = P_{\text{O}_2} \exp \left\{ \frac{0.046T^2 + 203.35T \ln(T/298) - (299.378 + 0.092T)(T - 298) - 20.591 \times 10^3}{(8.3144)T} \right\}$$

Equation 6: Oxygen Diffusion in Solutions (Tromans, 1998)

Figure 34 shows a quasi-linear relationship between the dissolution rates and pH between 10.5 and 11.5. The overall impact of pH is also small as the rate changes by less than 11% between the minimum value and the maximum.

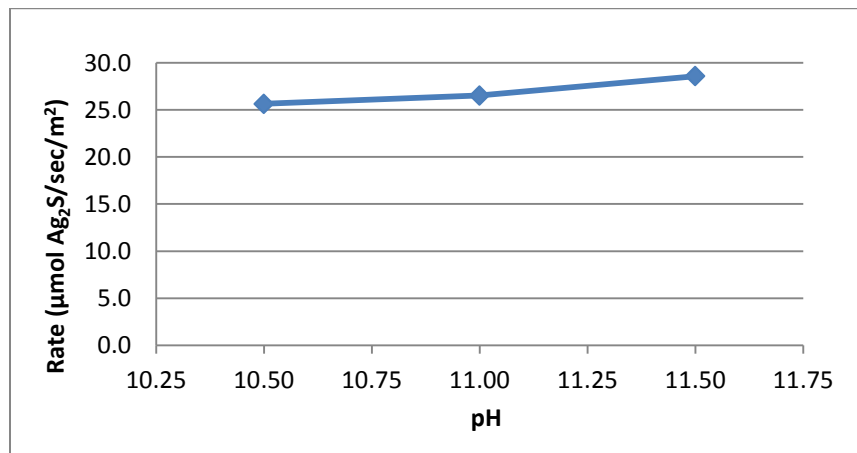


Figure 34: Silver Sulfide Flux vs. pH (pH 10.5, 11.0, 11.5 – 0.10g/L NaCN, 25°C, 600rpm, air)

The dissolution rates obtained under varying temperatures were used to calculate the activation energy of the reaction. In Figure 35, the logged-values of dissolution rates are plotted against the inverse of temperatures, which exhibit a linear relationship. The activation energy was calculated from the slope using the Arrhenius Rate Law (Equation 7), where k_T is the rate constant, A is a pre-exponential constant, E is the activation energy (kJ/mol), R is the universal gas constant (8.314kJ/mol/°K), and T is temperature (1/K x 1000). Example calculations are shown in Appendix A. The activation energy was determined to be 5.15kJ/mol, which satisfies the criteria for a mass-transport limited mechanism of less than <20kJ/mol.

$$k_T = A \cdot \exp\left(-\frac{E}{RT}\right)$$

Equation 7: Arrhenius Rate Law

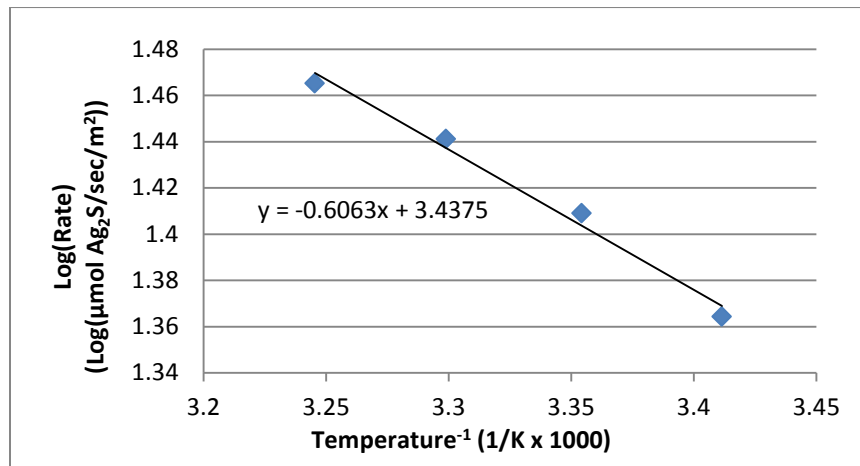


Figure 35: Log(Silver Sulfide Flux) vs. Inverse of Temperature (20, 25, 30, 35°C - 0.10g/L NaCN, pH 10.5, 600rpm, air)

Figure 36 shows the effects of adding potassium ferricyanide ($K_3Fe(CN)_6$) and hydrogen peroxide (H_2O_2) as additional oxidants. Ferricyanide induces a modest increase to the

dissolution kinetics, but hydrogen peroxide does not cause a significant impact. A ferricyanide concentration of 0.004M was used, which was scaled-down according to cyanide concentrations from the highest ferricyanide concentration employed by Xie (ie, 0.50g/L NaCN, 1g/L Fe^{3+} as $\text{Fe}(\text{CN})_6^{3-}$). The 0.01M hydrogen peroxide concentration was selected by multiplying the dissolved oxygen concentration under pure-oxygen saturation according to Equation 6 by a factor of ten.

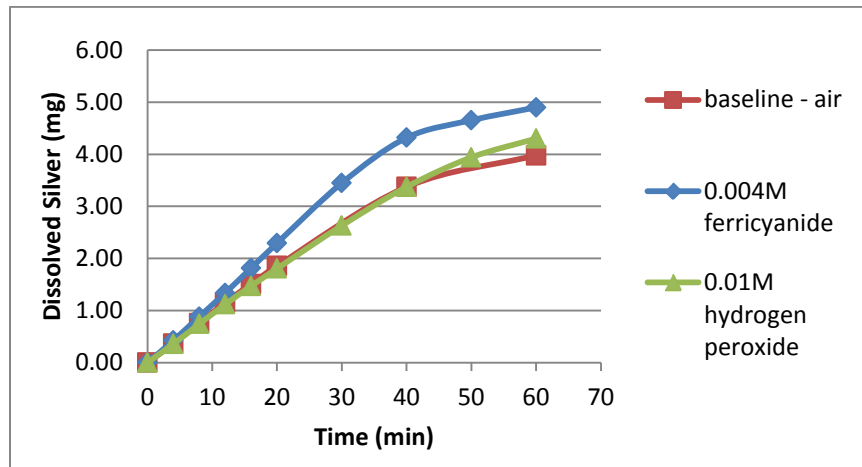


Figure 36: Silver Sulfide Dissolution vs. Time, Oxidants (0.10g/L NaCN, 25°C, 600rpm – hydrogen peroxide, ferricyanide)

5.3 Mercury Sulfide Results

5.3.1 Mercury Sulfide Dissolution & Shrinking Core Model

Kinetic experiments of mercury sulfide were conducted using a stirred reactor method and the reaction rates were studied using the Parabolic Leaching and the Linear Leaching equations in Equation 8 and Equation 10 (Peters, n.d.) which are shown below. In this way, the rate-limiting mechanism of mercury sulfide dissolution was determined and rate-constants were obtained and used as kinetic indicators.

The equations are based on a shrinking-core leaching model which assumes that the reacting particle shrinks internally and leaves behind a porous product layer at its original diameter. In a Parabolic Leaching scenario, the reaction rate is limited by the transport rate of reagents through the product layer while the chemical reaction rate at the surface is fast by comparison. Therefore, the reagent concentration, C_o (C_{bulk}), drops to nearly zero at the core's boundary (C_c) as shown in Figure 37.

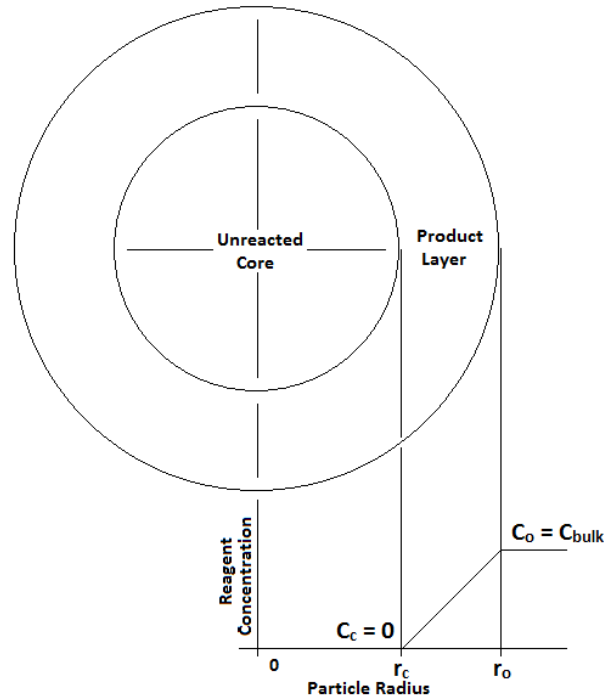


Figure 37: Parabolic Leaching Particle Diagram

Parabolic leaching is confirmed if the extraction data satisfies the relationship in Equation 8 and produces a linear plot as demonstrated in Figure 38, where X is the fraction of unreacted material, k_2 is a parabolic rate constant ($\text{cm}^2 \cdot \text{s}^{-1} \cdot M_d \cdot M_s^{-1}$), r_o is the radius of the original particle (cm), and t is time (sec). Units of M_d and M_s are described in the nomenclature.

$$1 - \frac{2}{3}X - (1 - X)^{\frac{2}{3}} = \frac{k_2}{r_o^2} \cdot t$$

Equation 8: Parabolic Leaching Extraction Equation

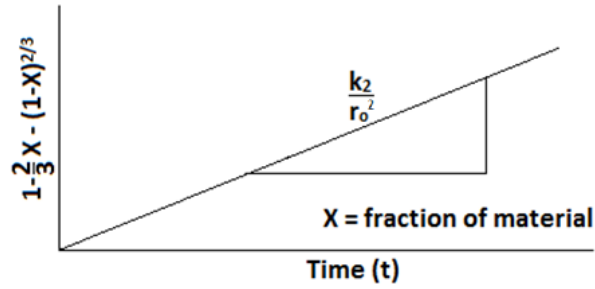


Figure 38: Parabolic Leach Rate, Extraction Data Plot

In the current work, only a single size of mercury sulfide was tested. Therefore, k_2' ($s^{-1} \cdot M_d \cdot M_s^{-1}$) was obtained as the rate indicator rather than k_2 , which assumes a constant initial particle size as shown in Equation 9.

$$k_2' = \frac{k_2}{r_0^2}$$

Equation 9: Parabolic Rate Constant for Constant Particle Size (r_0)

In a Linear Leaching scenario, reagent transport through the porous product layer is sufficiently fast that the rate of chemical reaction at the particle surface is rate limiting. This is shown in Figure 39 where the reagent concentration remains nearly unchanged at the core's surface and an excess of reagent is available at all times.

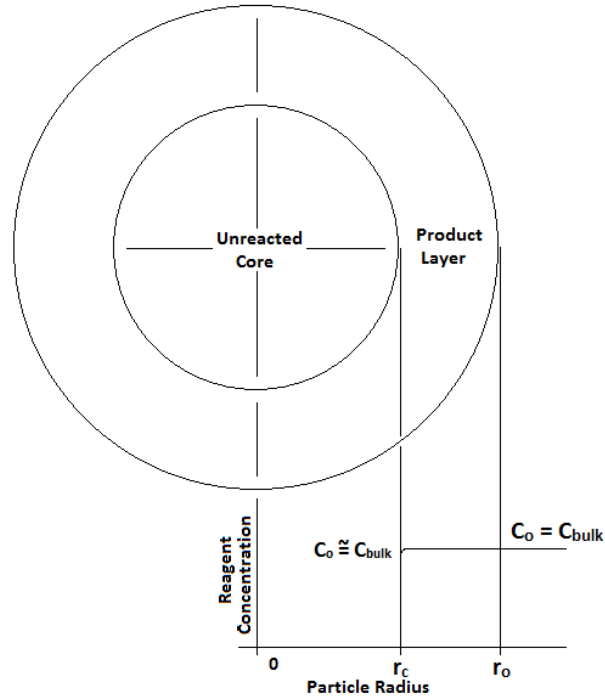


Figure 39: Linear Leaching Particle Diagram

Linear leaching is confirmed if the extraction data satisfies the relationship in Equation 10 to produce a linear plot as shown in Figure 40 where k_1 is the linear rate constant and X , r_o and t are synonymous with the parabolic equation (Equation 10). Again, k_1' was obtained rather than k_1 which assumes a constant r_o .

$$1 - (1 - X)^{\frac{1}{3}} = \frac{k_1}{r_o} \cdot t$$

Equation 10: Linear Leaching Extraction Equation

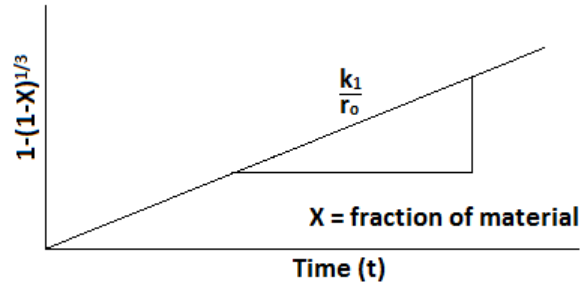


Figure 40: Linear Leaching Rate, Extraction Data Plot

5.3.2 Mercury Sulfide Solubility

Relative Solubilities of Cinnabar, Metacinnabar, and HgS Precipitate

The relative soluble properties of cinnabar (α -HgS, red), metacinnabar (β -HgS, black), and the HgS precipitate (p-HgS, black) were first investigated. Stirred reactor experiments were conducted for 48 hours at 0.5g/L HgS, 1g/L NaCN, and pH 11.5 under exposed air and mixing speed of 700rpm. In Figure 41, the highest extraction of 4.0% is observed from the p-HgS, followed by 0.95%, for β -HgS and <0.01% for α -HgS.

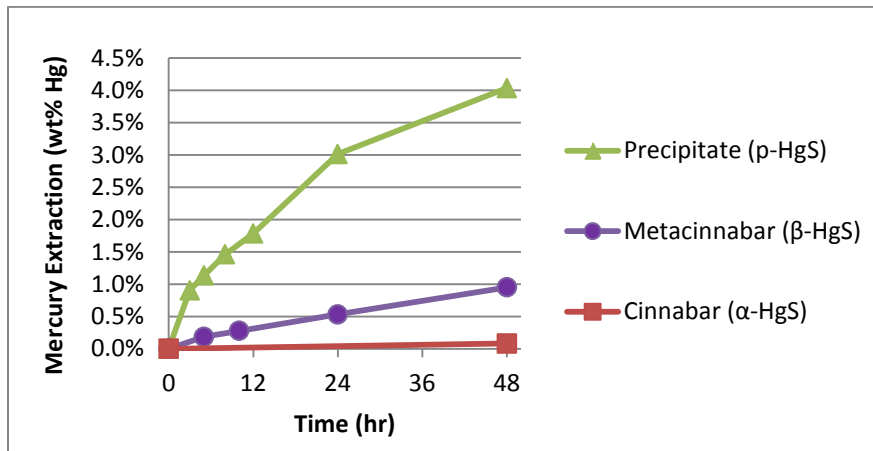


Figure 41: Mercury Sulfide Dissolution vs. Time, α -HgS, β -HgS, and p-HgS (0.5g/L HgS, 1.0g/L NaCN, pH 11.5, 25°C, 700rpm, air)

However, despite having demonstrated the highest solubility, further investigations with β -HgS were discontinued. It was deemed that reproducing the morphology of this reagent accurately for replicate studies in the future would be difficult.

High Cyanide Concentration Leaching of Cinnabar (α -HgS)

Cinnabar demonstrated the lowest solubility, so it was leached again at a higher cyanide concentration of 10g/L NaCN. Figure 42 shows that extraction increased to 0.19%, but this is still very low compared to β -HgS and α -HgS extractions.

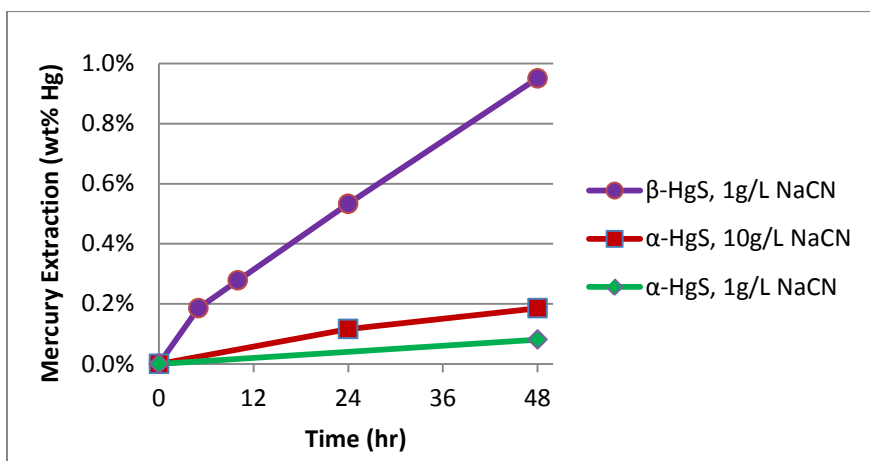


Figure 42: Mercury Sulfide (Cinnabar) Dissolution vs. Time, 1g/L & 10g/L NaCN (0.5g/L HgS, pH 11.5, 25°C, air, 700rpm)

As such, for the purposes of this work it was concluded that α -HgS is practically insoluble under normal cyanide leaching conditions and that further investigations were not necessary. Therefore, kinetic investigations were only conducted with metacinnabar (β -HgS) which demonstrated both high extractability and purity.

High Solids Concentration Leaching of Metacinnabar (β -HgS)

The impact of leaching metacinnabar at a lower solids (pulp) concentration was investigated. In this study, the total dissolved mercury concentrations were studied rather than the percent-extractions, as this is more relevant to the solubility-product relationship shown in Equation 11 of Reaction 7 (ie, $HgS_{\beta} = Hg^{2+} + S^{2-}$). The terms $a_{Hg^{2+}}$, $a_{S^{2-}}$, and a_{HgS} represent chemical activities.

$$K_{sp} = \frac{a_{Hg^{2+}} \cdot a_{S^{2-}}}{a_{HgS}} = [Hg^{2+}][S^{2-}]$$

Equation 11: Dissociation Product of Mercury Sulfide

Figure 43 shows that mercury dissolution rates increase with pulp concentration from 0.01g/L HgS to 0.5g/L HgS and dissolved mercury concentrations were 0.14mg/L Hg and 4.1mg/L after 48 hours, respectively. The change in extraction is nearly proportional to the pulp concentration of mercury sulfide, so it appears that the reaction rates are proportional to the exposed surface area of the solids.

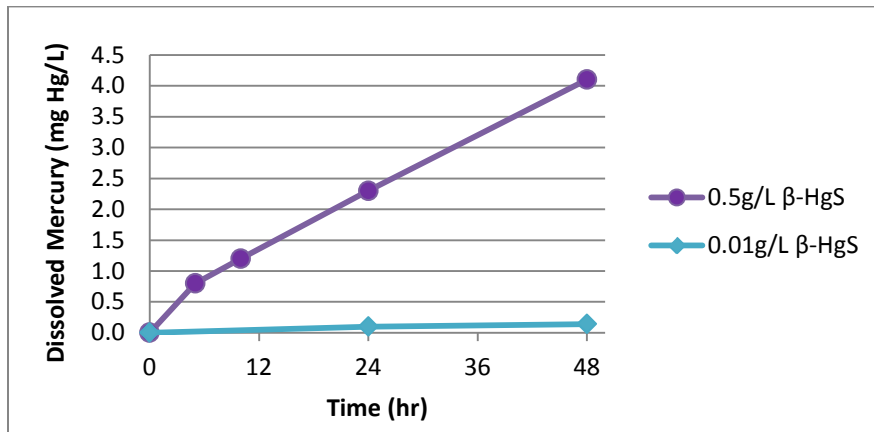


Figure 43: Mercury Sulfide (Metacinnabar) Dissolution vs. Time, 0.5g/L & 0.01g/L HgS (1g/L NaCN, 25°C, pH 11.5, 700rpm, air)

Effects of Stir Speeds

Different stir speeds were investigated to confirm that “good mixing” conditions were established, where the reaction is no longer dependence on the stirring rates. Figure 44 shows that the extraction rates at 700rpm and 1000rpm are nearly the same, which indicates that the reaction is independent of stir speeds in this range. However, to ensure that full suspension of solids are maintained, the speed of 1000rpm was adopted for all kinetic experiments with mercury sulfide.

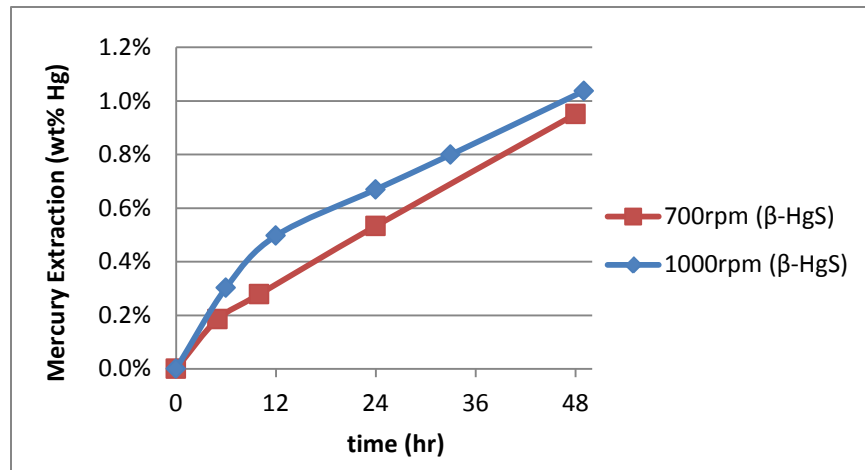


Figure 44: Mercury Sulfide (Metacinnabar) Dissolution vs. Time, Stir Speed (0.5g/L HgS, 1g/L NaCN, 25°C, pH 11.5, air)

5.3.3 Mercury Sulfide Kinetic Results

For the stirred reactor experiments of mercury sulfide (metacinnabar), a baseline leaching condition of 1.0g/L sodium cyanide, pH 11.5, 25°C, and air environment was chosen. Dissolved oxygen concentrations were measured in each experiment, which was consistent between 6.5mg/L to 7.5mg/L O₂ under a natural air environment. A high cyanide concentration was selected to increase mercury extractions which would be more accurately detected by AAS.

High pH was applied to to minimize the relative pH fluctuations over long experiment times. Experiments were conducted under varying cyanide concentration, oxygen content, pH, and temperature. The array of leaching conditions is listed in Table 5, consisting of 14 combinations.

Table 5: Conditions of Mercury Sulfide (Metacinnabar) Stirred Reactor Experiments

Baseline								
Cyanide (g/L NaCN)	1.0	0.02	0.05	0.10	0.25	0.50	1.0	2.0
Oxygen Content	Air	Nitrogen	Oxygen					
pH	11.5	10.5	11.0					
Temperature	25°C	35°C	40°C					

Nonlinear dissolution rates were observed from all mercury sulfide experiments, to which either the Parabolic Leaching equation (Equation 8, section 5.3.1) or the Linear Leaching equation (Equation 10, section 5.3.1) were applied to obtain rate constants. Figure 45 shows the original mercury sulfide (metacinnabar) extraction curves that were obtained at varying cyanide concentrations.

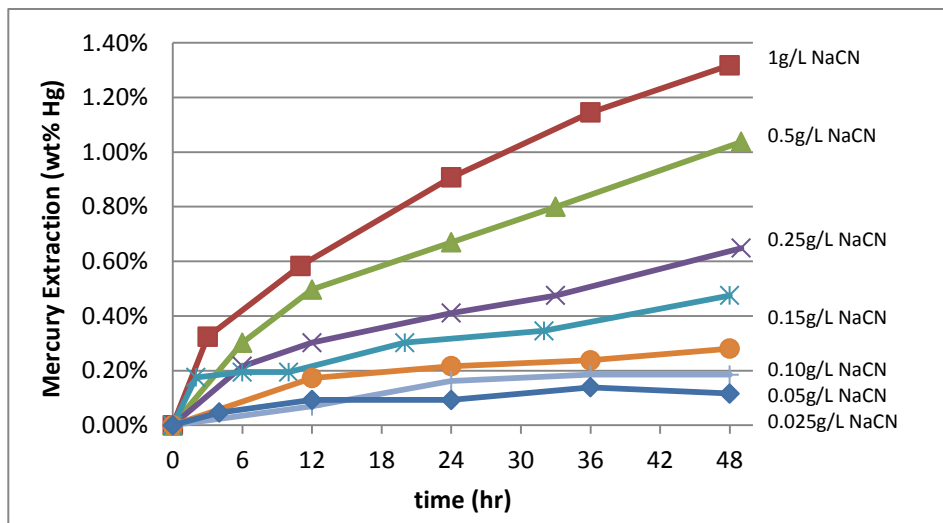


Figure 45: Mercury Sulfide (β -HgS) Extraction vs. Time (1.0, 0.5, 0.25, 0.15, 0.10, 0.05, 0.025g/L NaCN – pH 11.5, 25°C, air)

It was found that applying the Parabolic Leach equation produced linear relationships as shown in Figure 46, while the Linear Leach equation still resulted in curved lines (Linear Leach application not shown). According to the shrinking-core leaching theory from section 5.3.1, this indicates that mercury sulfide extraction is distinctly a parabolic process where the rate is controlled by diffusion of chemical species through a porous product layer. This layer is most likely to be a sulfur or polysulfide substance.

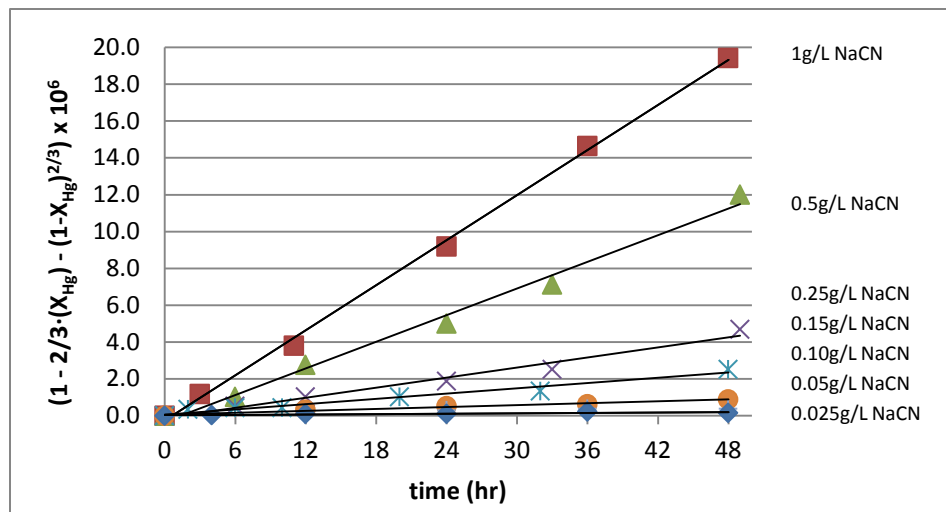


Figure 46: Mercury Sulfide Linearized Extraction vs. Time (1.0, 0.5, 0.25, 0.15, 0.10, 0.05, 0.025g/L NaCN – pH 11.5, 25°C, air)

The parabolic rate constants (k_2') were obtained from the linear slopes and plotted against cyanide concentrations, which shows a linear relationship in Figure 47.

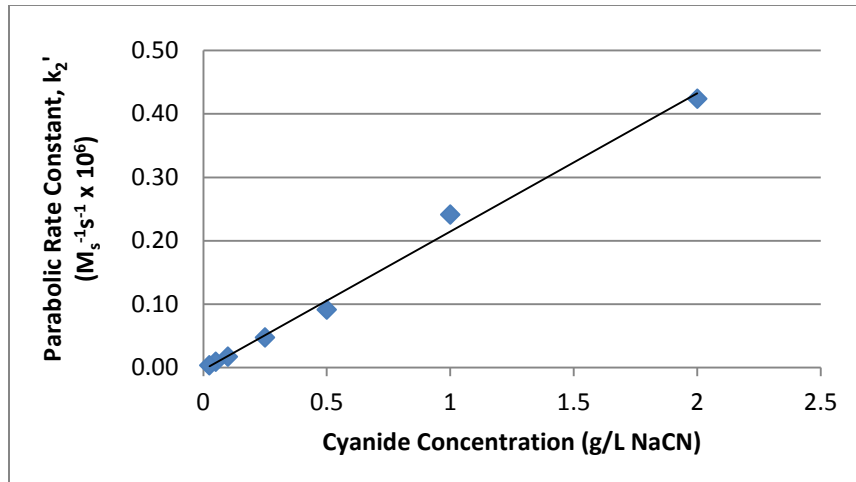


Figure 47: Mercury Sulfide Rate Constant vs. Cyanide Conc. (1.0, 0.5, 0.25, 0.15, 0.10, 0.05, 0.025g/L NaCN – pH 11.5, 25°C, air)

Likewise, the Parabolic Leaching equation corresponded to other mercury sulfide extraction data, and the Linear Leaching equation continued to relate poorly, so only the parabolic scenario was investigated. In Figure 48, a nonlinear relationship is shown between the parabolic rate constants and dissolved oxygen concentrations.

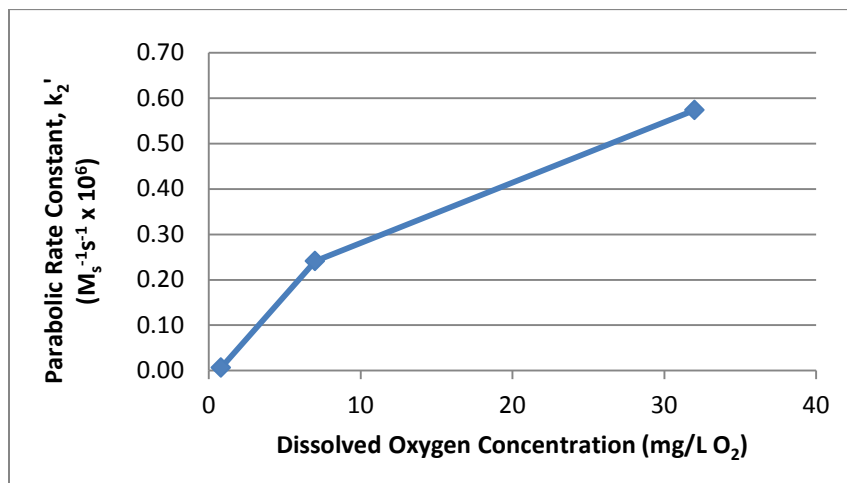


Figure 48: Mercury Sulfide Rate Constant vs. Dissolved Oxygen Concentration (O₂, air, N₂ - 1g/L NaCN, pH 11.5, 25°C)

Decreasing the oxygen concentration has a greater impact than increasing it, which is analogous to the silver sulfide work (section 5.2.3). Also, this kind of non-linear relationship is indicative of the reaction becoming less dependent on oxygen at higher concentrations. However, the overall influence of oxygen is considerably high, such that mercury sulfide extraction never appears to be fully independent oxygen. Oxygen concentrations were measured to be 0.6mg/L O₂ and 7.0mg/L O₂ under nitrogen-sparging and the air environment, respectively. The concentration under oxygen-sparging exceeded the instrument's limit and was calculated as 32.4mg/L O₂ by *Tromans'* oxygen diffusion model (Equation 6). Figure 49 shows a quasi-linear relationship between the parabolic rate constants and pH.

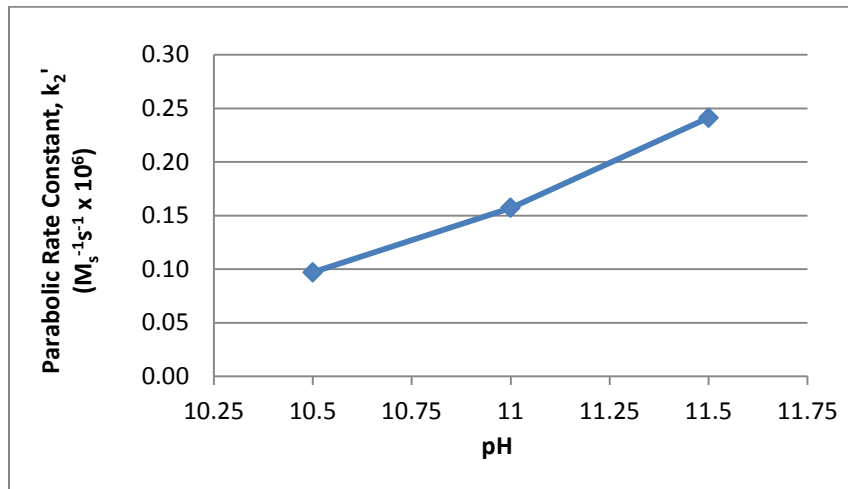


Figure 49: Mercury Sulfide Rate Constant vs. pH (pH 10.5, 11.0, 11.5 - 1 g/L NaCN, 25°C, air)

The parabolic rate constants obtained under varying temperatures were used to determine the activation energy using the Arrhenius Rate Law. Figure 50 shows a linear line applied to the logged-value of rate constants against the inverse of leaching temperatures ($1/K \times 1000$), from

which the average activation energy was calculated to be 5.81kJ/mol. This satisfies the thermodynamic condition for mass-transport control of <20kJ/mol, but the line fits poorly.

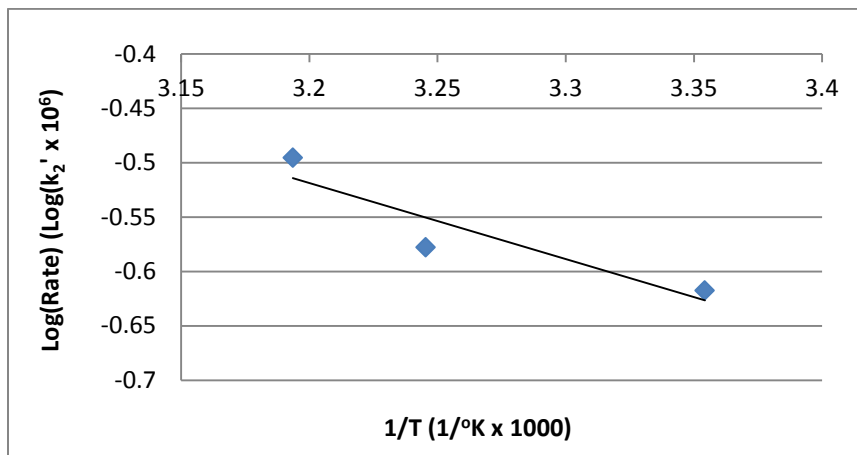


Figure 50: Log(Mercury Sulfide Rate Constant) vs. Temperature⁻¹ (25°C, 35°C, 40°C - 1 g/L NaCN, pH 11.5, air)

It was considered that two conflicting slopes may co-exist that represent different reaction mechanisms. Therefore, activation energies were calculated again between 25°C-35°C and 35°C-40°C to be 3.05kJ/mol and 13.19kJ/mol, respectively, which confirm that the condition for mass-transport control is still satisfied.

5.4 Leach Residue Results

Leaching experiments were conducted on Yanacocha’s leached residue rather than the run-of-the-mine ore. This was preferred because the aim of this research was to increase extractions from the unleached silver species that could not be extracted under Yanacocha’s existing leaching conditions. It is hoped that the newly discovered leaching conditions may be applied to the spent leach tailings at Yanacocha to further recover silver while simultaneously avoiding the excessive release of mercury.

5.4.1 Leach Residue Experimental Conditions

Leach Residue samples from the Yanacocha Mine were tested by stirred reactor experiments. A baseline condition of 0.10g/L sodium cyanide, pH 11.5, 25°C, and air environment was selected, where the lower cyanide concentration reflects the leaching conditions applied at Yanacocha, while the high pH ensured that relatively consistent hydroxide concentrations are maintained during the long experiment times (48 hours). Experiments were conducted under varying cyanide concentrations, oxygen concentrations, pH, and temperature at a constant pulp density of 10wt% residue. The array of leaching conditions tested is listed in Table 6 which consists of 7 combinations.

Table 6: Conditions for Heap Leach Residue (Source: *Yanacocha Mine*) Stirred Reactor Experiments

	Baseline		
Cyanide Concentration (g/L NaCN)	0.10 g/L	0.25 g/L	0.50 g/L
pH	11.5	11.0	10.5
Oxygen Content (gas purge)	Air	Oxygen	
Temperature (°C)	25°C	35°C	

The extraction rates of silver and mercury were both examined from each experiment. Due to irregular shapes realized from many of the extraction curves, mathematical models were not applied to the data. Instead, investigations proceeded with only qualitative comparisons of extraction rates.

5.4.2 Leach Residue & Silver Extraction

Figure 51 shows that silver extraction rates increase with cyanide concentrations, but the relationship is not proportional. Extraction curves at 0.25g/L NaCN and 0.5g/L NaCN are nearly the same.

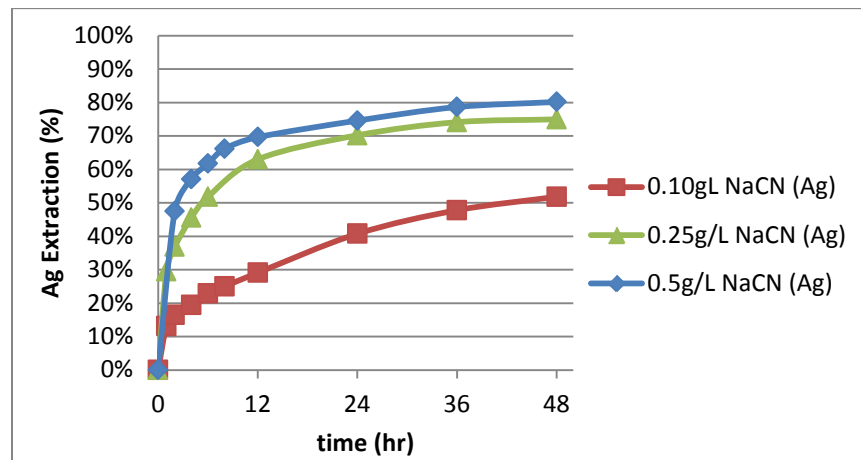


Figure 51: Silver Extraction from Residue vs. CN Concentration (0.10, 0.25, 0.5g/L NaCN, pH 11.5, 25°C, air)

Figure 52 shows that the silver extraction rate increases under oxygen-sparging compared to a regular air environment. However, the change is not proportional to the increase in oxygen content.

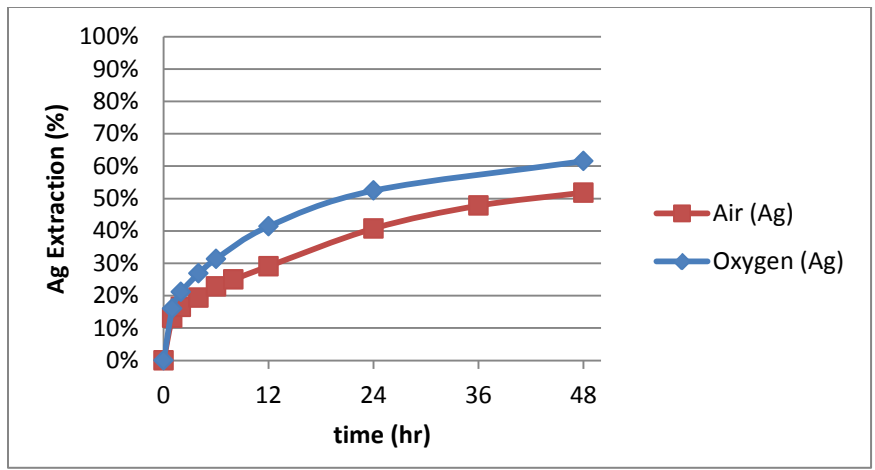


Figure 52: Silver Extraction from Residue vs. Oxygen Content (sparged air, oxygen - 0.10g/L NaCN, pH 11.5, 25°C)

As seen in Figure 53, silver extraction results from varying pH were compared only within the initial 12 hour timeframe the rate decreases with increasing pH. At later times (>12 hour) the extraction curves decreased rapidly and began to overlap, making it difficult to conduct discerning analyses among the results. It is believed that the earlier region represents the true dissolution rate of the metals that is not interfered by secondary effects of product-species.

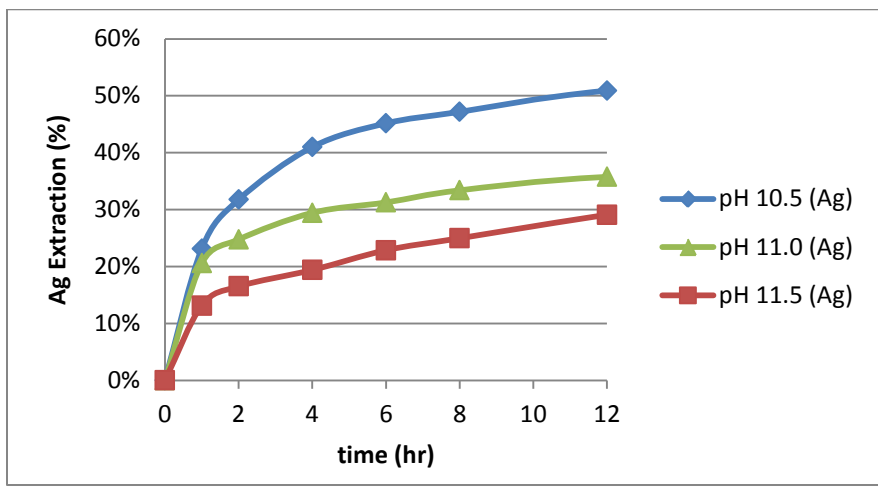


Figure 53: Silver Extraction from Residue vs. pH (pH 10.5, 11.0, 11.5 – 0.1g/L NaCN, 25°C, air)

Figure 54 shows that the increase in silver extraction was marginal when temperature was increased from 25°C to 35°C. This is consistent with the findings from the rotating disc experiments with pure silver sulfide where the influence of temperature was small and resulted in a low value of activation energy.

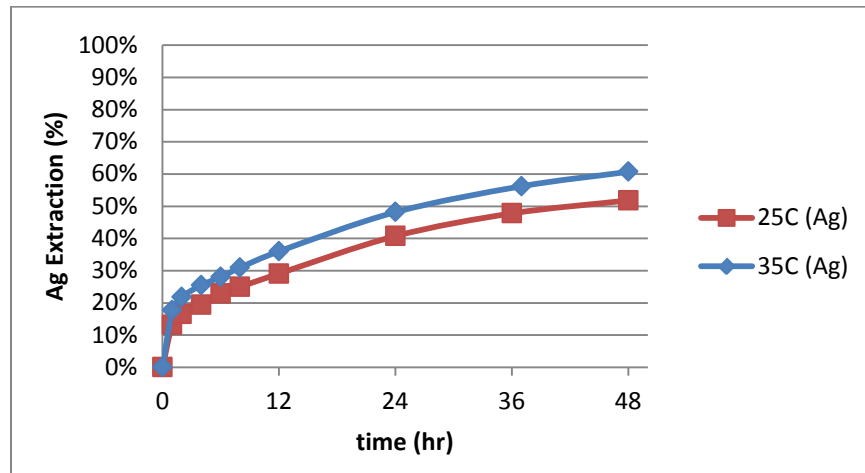


Figure 54: Silver Extraction from Residue vs. Temperature (25°C, 35°C - 0.10 g/L NaCN, pH 11.5, air)

5.4.3 Leach Residue & Mercury Extraction

Figure 55 shows that mercury extraction rates decrease with increasing cyanide concentrations. This is contrary to the pure mercury sulfide experiments in section 5.3.3 where dissolution rates had distinctly increased. However, it must be considered that the mercury concentration measurements from these experiments were very near the detection limit of the analytical method (Hg-CVA), where precise results are difficult to obtain. Considering, then, that the error range of the analyses was high, the extraction results appear to be too low and close together (7.4%- 17.9%) to ascertain a precise relationship to cyanide concentration. Therefore, it is only

perceived from these results that mercury extraction is not significantly affected by cyanide, and that further investigations are required before a conclusive relationship can be interpreted.

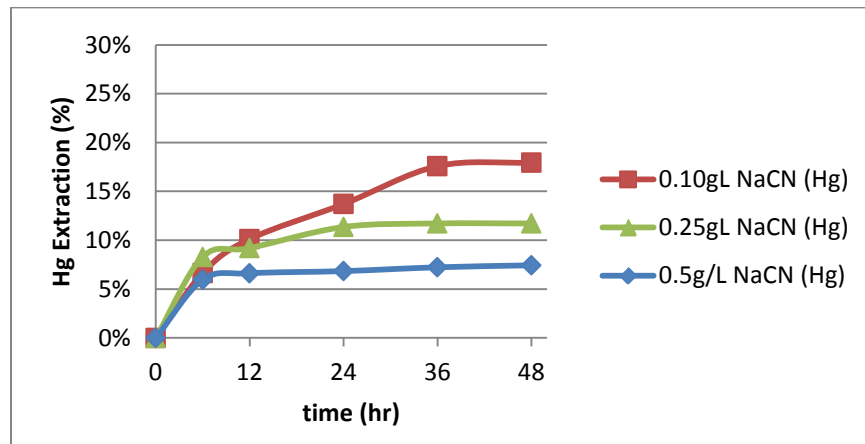


Figure 55: Mercury Extraction from Residue vs. CN Concentration (0.10, 0.25, 0.5 g/L NaCN, pH 11.5, 25°C, air)

Figure 56 shows the relationship between mercury extraction and pH. Similar mercury extraction rates are observed at pH 10.5 and pH 11.5 and a significantly lower rate is observed at pH 11.0. It must be noted, however, that the Leach Residue used in the pH 11.0 experiment contained a higher mercury concentration of 8.50g/t Hg compared to 6.69g/t Hg and 6.55g/t Hg in the pH 10.5 and pH 11.5 experiments, respectively, which may have affected the reaction kinetics. This is significant because *Mikac et al (2002)* reported that mercury sulfide extraction in chloride solutions decreased rapidly with increasing pulp densities (section 2.3.3, Figure 19). A complete list of mercury head assays is available in Appendix B. Therefore, the result at pH 11.0 is disregarded for this analysis, and from the remaining two results it is determined that pH has an insignificant impact on mercury extraction from the Leach Residue. Again, further investigations are recommended.

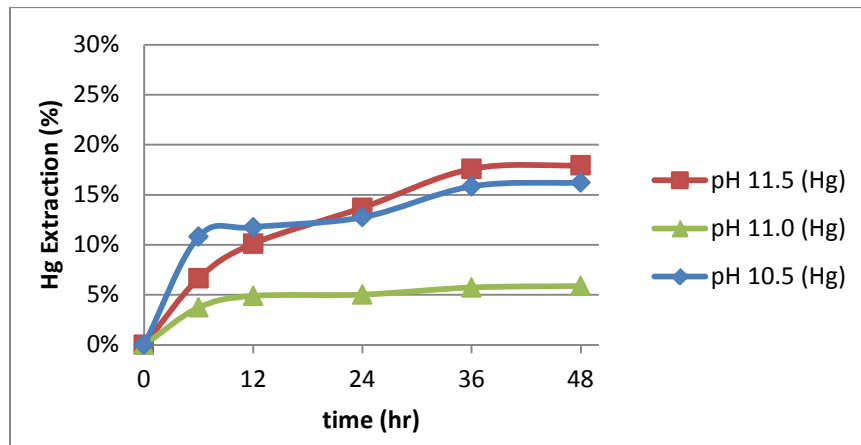


Figure 56: Mercury Extraction from Residue vs. pH (pH 10.5, 11.0, 11.5 - 0.10 g/L NaCN, 25°C, air)

Figure 57 shows that mercury extraction rates increase with oxygen concentration, but the increase is not proportional. Also, extraction in the oxygen environment is *delayed* and begins to increase only after ~6 hours.

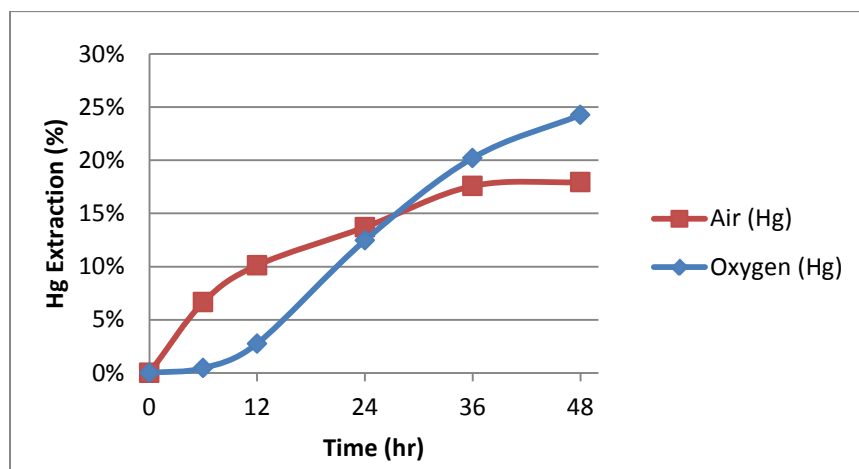


Figure 57: Mercury Extraction from Residue vs. Dissolved Oxygen Concentration (air, oxygen - 0.10 g/L NaCN, pH 11.5, 25°)

Again, this may be due to the inhibiting effects of a higher mercury concentration found with the Leach Residue used in the oxygen-sparged experiment of 9.67g/t Hg compared to 6.44g/t in the other. However, judging by the difference in steepness of slopes, it appears that the overall impact of oxygen is distinctly significant. This is analogous to the pure mercury sulfide experiments (section 5.3.3) where oxygen concentration also had a significant influence.

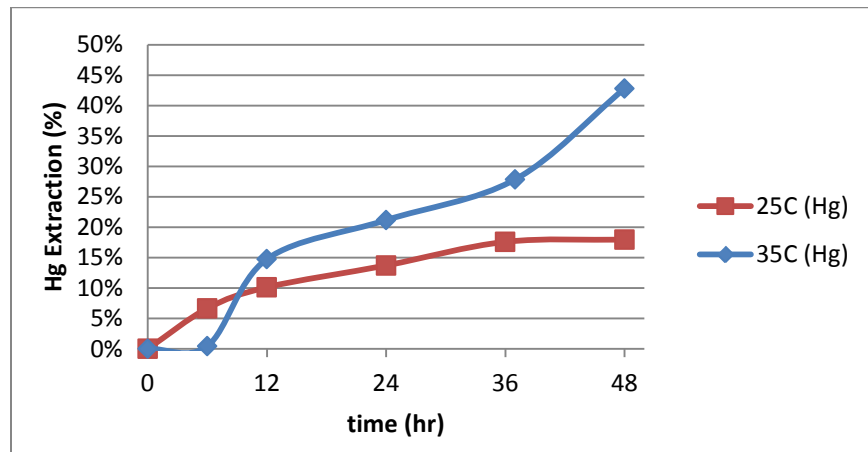


Figure 58: Mercury Extraction from Residue vs. Temperature (25°C, 35°C - 0.10 g/L NaCN, pH 11.5, air)

Figure 58 shows that a temperature change from 25°C to 35°C also has a considerable impact on mercury extraction. This is contrary to the mercury sulfide (metacinnabar) experiments where a very mild response was seen as a result of temperature changes.

6 Discussion

6.1 Dissolution Kinetics of Silver Sulfide

6.1.1 Silver Sulfide Rate Controlling Mechanism

The results of pure silver sulfide dissolution kinetics are available in section 5.2.3. According to the Levich equation, the linear relationships that were observed against cyanide concentrations and the square-root of rotation speeds in Figure 31 and Figure 32 are indicative of a cyanide mass-transport limited reaction. Also, the fact that the linear line passes through the origin is characteristic of a *pure* mass-transport limited process, where surface reaction rates do not affect the overall rate. The calculated activation energy of 5.15kJ/mol from Figure 35 is also sufficiently low below the criteria of <20kJ/mol to confirm the presence of a mass-transport limited process.

6.1.2 Silver Sulfide & Cyanide, Oxygen and pH Effects

In Figure 31, a strong linear relationship is seen between the silver discs' dissolution rates and cyanide concentrations. By contrast, very little impact is observed from changes in dissolved oxygen concentrations as shown in Figure 33, and Figure 34 shows that pH inflicts very little change to the dissolution rate as well. These results indicate that cyanide is the dominant rate-limiting component and that the reaction is nearly independent of oxygen and hydroxide diffusion. *Xie (2007)* also observed a weak association between pH and silver sulfide dissolution, and *Luna & Lapidus (2000)* reported about the marginal influence of oxygen-concentration.

Based on the reaction stoichiometry of silver sulfide in cyanide reported by *Luna & Lapidus (2000)* shown in Reaction 11, it was initially expected that oxygen would greatly affect the dissolution kinetics. However, this was not the case and the lack of its influence was further investigated. Figure 59 shows a series of silver-dissolution versus oxygen-concentration curves from rotating disc experiments of elemental silver (Senanayake, 2006). The lines become increasingly non-linear as cyanide concentrations decrease below 5mM (~0.25g/L NaCN), which indicates a transition from an oxygen-diffusion limited mechanism to cyanide-diffusion for the pure silver system. If we assume that this is also true of *silver sulfide*, then the reaction would be expected to be independent of oxygen-diffusion at the considerably lower cyanide concentration of 0.10g/L (~2mM CN⁻) in the current work, which may explain why oxygen demonstrates so little influence on its kinetics.

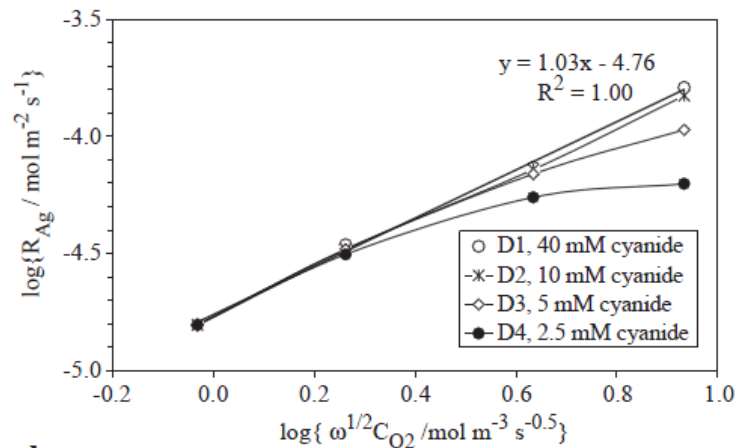


Figure 59: Silver Dissolution vs. Oxygen Concentration at Varying CN Concentrations (Senanayake, 2006)

6.1.3 Silver Sulfide & Ferricyanide, Hydrogen Peroxide

Ferricyanide and hydrogen peroxide have been investigated as additional oxidants to atmospheric air to improve the dissolution kinetics of silver sulfide. However, the results in Figure 36 (section 5.2.3) show that neither oxidant is significantly effective. Figure 60, published by *Xie (2007)*, shows that silver sulfide dissolution becomes increasingly independent of cyanide at high cyanide concentrations in de-aerated cyanide-ferricyanide solutions, which is characterized by its continually decreasing slope. *Xie* had already established that pH did not significantly influence the kinetics and ferricyanide was the only other component (no oxygen), so it is expected that the rate controlling mechanism will transition to ferricyanide-diffusion at high cyanide concentrations, which may be why *Xie* experienced a significant improvement to the kinetics when 0.5g/L NaCN was used (high concentration). By contrast, ferricyanide would be less effective at the lower cyanide concentration of 0.10g/L NaCN in the current work.

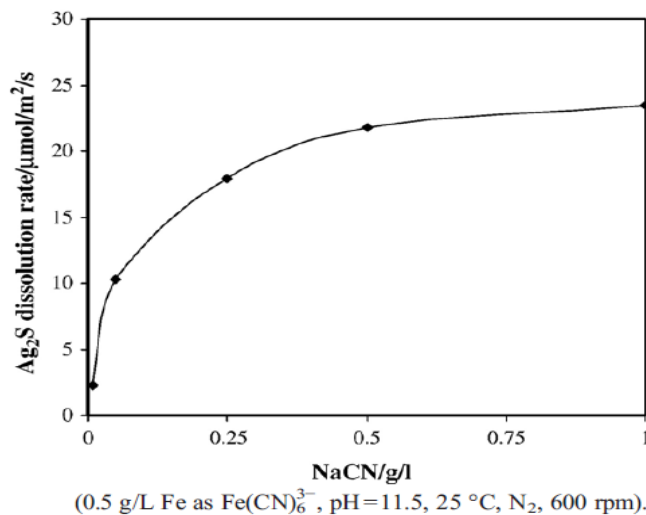


Figure 60: Silver Sulfide Dissolution Rate vs. Cyanide Concentration in Ferricyanide (0.5g/L Fe as Fe(CN)₆³⁻, pH 11.5, 25°C, N₂, 600rpm - *Xie, 2007*)

With regard to the low effectiveness of hydrogen peroxide, it was suggested by *Luna & Lapidus* that oxygen-reduction on silver sulfide does not produce peroxide intermediates. Therefore, since peroxide is not involved in the reaction, it is conceivable that the presence of excess hydrogen peroxide would not provide an additional driving force for silver sulfide's dissolution reaction. By contrast, hydrogen peroxide would be expected to benefit gold-dissolution kinetics, since oxygen-reduction on gold substrates follows a sequential 2-electron pathway where hydrogen peroxide *is* formed as an intermediate product, as discussed by *Hiskey & Sanchez (1990)*.

6.1.4 Silver Sulfide & Sulfide Oxidation Limited Kinetics

The decreased dissolution rates realized from the silver sulfide rotating disc experiments beyond 30 minutes of leaching are thought to be caused by the saturation of un-oxidized sulfide ions from the dissolution of silver sulfide which would effectively suppress the forward kinetics of the overall reaction. It was reported by *Luna & Lapidus (2000)* that silver sulfide extraction was limited by the slow oxidation rate of sulfides, which was determined by matching experimental data to a shrinking-core based model (detailed in section 2.3.2). *Luna & Sanchez (2003)* also discussed sulfide-saturation limited kinetics, where it was observed that silver sulfide dissolution rates increased in the presence of lead nitrate, which is a known catalyst for sulfide-oxidation. Due to the low solubility of silver sulfide, even a small accumulation of sulfide could saturate the solution and inhibit dissolution rates. Therefore, it is expected that sulfide saturation may be a rate controlling factor, particularly at later leaching times (>30 minutes) when dissolution rates decreased nearly to plateau-levels.

Also, it was discussed in section 5.2.1 that consistent dissolution rates could not be obtained when silver sulfide discs were re-used. Even when fresh surfaces were exposed by removing ~40% of the original thickness, dissolution rates became lower and more non-linear than before. It is suspected that silver sulfide's solubility was affected by contamination from the sulfide-saturated solution. *Luna & Sanchez (2003)* also observed that the dissolution of silver sulfide decreased over time due to the adsorption of chemical species on the electrode which was suspected to be *modifying* the surfaces. In the current work, SEM imaging of a leached disc's surface and cross-section did not reveal any visual evidence to suggest that chemical films or surface-modifications had occurred. Also, elemental analysis by SEM/EDS showed that the silver-to-sulfur ratio remained unchanged in the internal structures of unleached and leached discs. However, elemental analysis by XPS revealed a distinct increase in the sulfur-to-silver ratio from 0.46:1 on unleached surfaces to 0.63:1 on leached surface, indicating sulfur-enrichment. It was also identified by XPS that S^{2-} was the predominant valence state of sulfur, but the identity of the counterbalancing anion is uncertain. Due to the hyper-sensitivity of XPS analysis, however, the energy signals which resemble S^{2-} may have been detected from the outer-most electron shells of individual sulfur atoms, which can depend on the random orientation of crystals. Therefore, it must not be accepted with absolute certainty that S^{2-} is the *only* valence state of sulfur on the disc's surface, and it must also be considered that other forms may exist.

Compared to SEM/EDS, XPS demonstrates an exceptionally low analytical depth (~6 μ m vs. 10 \AA) which makes it more reliable in this application, and the detected sulfur is limited only to the

surface layer and not the entire disc. However, the metallographic results do not provide conclusive evidence that this contamination was strictly a sulfur-based cause, but merely suggests that sulfur may have been involved in the process. It is only certain at this point that the entire silver sulfide disc became less soluble after leaching, even in the internal structures that appeared not *physically* exposed, but the cause is not well understood. Further investigations are required before exact conclusions can be drawn.

6.2 Dissolution Kinetics of Mercury Sulfide

6.2.1 Mercury Sulfide Rate Controlling Mechanism

The results of pure mercury sulfide (metacinnabar) experiments are shown in section 5.3.3. Application of the Parabolic Leach equation confirmed that mercury sulfide extraction is controlled by the diffusion of chemical species through a product layer. The diffusing species was later identified to be cyanide. A diffusion-limited mechanism was confirmed again from the calculated activation energies of 3.05kJ/mol between 25°C-35°C and 13.16kJ/mol between 35°C-40°C, both of which satisfy the condition for mass-transport control of <20kJ/mol.

6.2.2 Mercury Sulfide & Sulfide Oxidation Limited Kinetics

Sulfide-oxidation limited kinetics was also considered in the silver sulfide studies in section 6.1.4. Similar to silver sulfide, mercury sulfide possesses an exceedingly low K_{sp} of 8.51×10^{-54} . Therefore, it was suspected that its dissolution kinetics may also be limited by the saturation of dissociation products, Hg^{2+} and S^{2-} , and its rate controlled by the subsequent reaction rates of mercury-cyanide complexation and sulfide oxidation, respectively.

Therefore, an experiment was conducted at a lower pulp concentration of 0.01g/L β -HgS to investigate the following hypothesis: if sulfide-saturation is rate limiting, then saturation of dissociated species would occur regardless of the solids content and the dissolution rates would remain unchanged at the lower pulp concentration. However, if the reaction is controlled by charge-transfer and/or reagent-diffusion, then the reaction rate would only be dependent on

the leachable surface area of mercury sulfide, so the dissolution rates would increase with pulp concentration. This assumes that the dissociation of HgS to Hg^{2+} and S^{2-} is rapid.

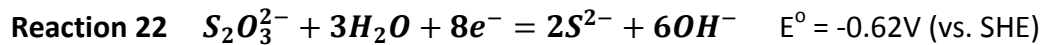
The results shown in Figure 43 in section 5.3.2 demonstrated that dissolution rates decreased at the lower pulp concentration. This suggests that the system is not saturated with sulfides during leaching, and that the reaction kinetics is limited only by the reaction mechanisms occurring at the surface of the individual mercury sulfide particles.

6.2.3 Mercury Sulfide & Cyanide, Oxygen and pH Effects

In a typical rate-limited reaction, changes made to only one leaching condition would significantly impact the overall kinetics, while the others are not very influential. However, mercury sulfide extraction demonstrates strong relationships to all three leaching parameters (ie, cyanide concentration, oxygen concentration and pH) which mislead the interpretation. The oxidation kinetics of sulfide was considered in order to explain this phenomenon.

Breuer et al (2008) studied the oxidation kinetics of sulfides and reported that both thiocyanate (SCN^-) and thiosulfate ($\text{S}_2\text{O}_3^{2-}$) were produced as oxidation products in aerated cyanide solutions, and that the total oxidation rate decreased when the oxygen concentration decreased (Breuer, Jeffrey, & Hewitt, 2008). In silver sulfide systems, *Xie (2007)* proposed that thiosulfate is not always formed directly from the oxidation of sulfide-ions, but also from the subsequent oxidation of thiocyanate by oxygen. The reactions proposed by *Xie* are shown in Reaction 21 and Reaction 22. These reactions actually suggests that thiocyanate formation is more

favourable than thiosulfate, but both *Xie* and *Luna & Lapidus (2000)* have observed thiosulfate as significant oxidation products in the cyanidation of silver sulfide, where *Luna & Lapidus* observed thiosulfate as the *only* sulfur-product after 24 hours of leaching tests. This suggests that both cyanide and oxygen may be simultaneously active in oxidizing sulfides.



Therefore, in mercury sulfide systems, it is suspected that thiocyanate is the initial sulfur product, which may further oxidize to form thiosulfate in the presence of oxygen. The hypothesized reaction pathway of mercury sulfide is illustrated in Figure 61.

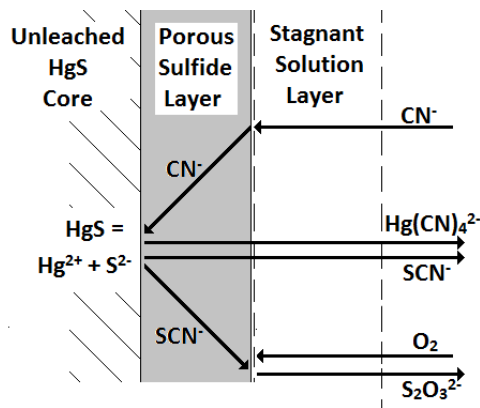


Figure 61: Hypothesized Mercury Sulfide Reaction Pathway Diagram

It was already established in section 6.2.1 that a porous product layer is formed on the mercury sulfide particles by application of the Parabolic Leach equation. The illustration in Figure 61 suggests that cyanide would diffuse through the porous layer and reacts with the dissociated

Hg^{2+} and S^{2-} at the unleached core boundary, forming $\text{Hg}(\text{CN})_4^{2-}$ and thiocyanate (SCN^-). These products will exit back through the product layer and into the bulk solution where thiocyanate could undergo further oxidation with oxygen to form thiosulfate ($\text{S}_2\text{O}_3^{2-}$). The rate of oxidation may also be accelerated at high pH which was suggested by *Luthy et al (1979)*. It is thought that this subsequent oxidation of thiocyanate is where oxygen and pH contribute to increasing the extraction kinetics of mercury sulfide.

The parabolic rate constant (k_2') is a linear function of the rate-limiting reagent's concentration as seen in Equation 12, where D_i' , ν , f_ν , r_o are constant values. A linear relationship is observed in Figure 47 between mercury sulfide extraction and cyanide concentrations up to 2g/L NaCN. This confirms that cyanide is, in fact, a diffusing species through the product layer according to the Parabolic Leach equation and the expression for the parabolic rate constant in Equation 12.

$$k_2' \cdot t = \frac{8\pi D_i' (C_c - C_o)}{3\nu f_\nu r_o^2} \cdot t$$

Equation 12: Parabolic Rate Constant Equation, k_2' (Peters, n.d.)

Figure 48 shows a nonlinear relationship against oxygen concentration which, based on Equation 12, indicates that it does not diffuse through the product layer. However, oxygen still greatly affects the dissolution rate of mercury sulfide, which is assumed to be oxidizing thiocyanate to thiosulfate as demonstrated in Figure 61. Synonymously, *Breuer et al (2008)* reported that the rate of sulfide-oxidation increased in cyanide solutions when pure oxygen

was introduced, and that the production rate of thiosulfate also increased as a result where only thiocyanate was produced before at lower oxygen concentrations.

Figure 49 shows that mercury sulfide dissolution is also significantly affected by pH. This is synonymous with *Luthy et al (1979)* regarding the increase in polysulfide oxidation rates with increasing pH from 8.5-12 in cyanide solutions (Luthy & Bruce, 1979).

Therefore, the experimental results comply with the concept that the reaction is limited by the diffusion of cyanide, and that the reaction is made faster at higher oxygen concentration and pH as expressed in Figure 61.

6.3 Dissolution Kinetics Heap Leach Residue, Yanacocha Mine

6.3.1 Leach Residue Silver Extraction & Cyanide, Oxygen and pH

The silver extraction results from the Yanacocha Leach Residue are shown in section 5.4.2. Silver extraction increased with cyanide concentrations, but the changes were not proportional. The extraction rates at 0.25g/L NaCN and 0.50g/L NaCN are nearly the same, which suggests that the reaction becomes less dependent of cyanide at higher concentrations.

In pH investigations, the extraction rates decreased with increasing pH, which could be explained by considering the oxygen reduction mechanism on silver sulfide. In section 6.1.3, *Luna & Lapidus* suggested that, during the dissolution of silver sulfide, oxygen reduces to hydroxide without forming peroxide intermediates. Therefore, it is believed that at higher pH, the excess of hydroxides suppresses the forward reaction of oxygen reduction which decreases the overall dissolution rate.

Under oxygen sparging the silver extraction rates increased, but the increase was not proportional. The influence of oxygen concentration was also small on pure silver sulfide from rotating disc experiments. These results are both synonymous with the work by *Luna & Lapidus (2000)*, where it was observed that silver extractions increased under oxygen-sparging, but the change was not proportional to the increased oxygen content.

Overall, silver extractions from the Yanacocha Heap Leach Residue are nearly analogous to the kinetic studies of pure silver sulfide, with the exception of the pH-relationship which was

reversed. In summary, silver extraction from the Leach Residue appears to increase with lower pH and increases with cyanide concentrations. Higher oxygen concentration assists with extraction, but the benefits realized may be too small to justify the economics of supplying it.

6.3.2 Leach Residue Silver Extraction & Sulfide Saturation

It was observed that all silver extraction data from the Leach Residue exhibited a common shape, where rapid silver dissolution is observed in the initial 1-2 hours, followed by a gradual decrease between 3-8 hours. Beyond 12 hours, all rates stabilize and adopt the same slope, regardless of the leaching condition, and none of the extractions reached 100%. This behaviour suggests that the reaction is limited by the saturation of dissociation products from the Leach Residue. Saturation-limited kinetics was discussed first in section 5.4.3.

It is thought that, initially, the Leach Residue dissociates freely until the solubility limit is reached and the forward reaction begins to be suppressed, resulting in a gradual decrease in the extraction rate. After this, extraction rates attain constant rates which are governed by the rate of disposal of the saturating species by oxidation, resulting in the shallower slopes seen beyond 12 hours. A similar sulfide-saturation (and oxidation) limited kinetics was also considered in the pure silver sulfide dissolution kinetics, which is discussed in section 6.1.3. This phenomena appears to be less of an issue in the later-discussed mercury extraction, but was commonly considered in silver kinetic studies of both the residue and the analytical reagent.

6.3.3 Leach Residue Mercury Extraction & Cyanide, Oxygen and pH

The extraction results of mercury from the Yanacocha Heap Leach Residue are shown in section 5.4.3. Extraction rates decreased with increasing cyanide concentration, which is contrary to the study conducted by Newmont Mining where mercury extraction reportedly increased with cyanide concentrations (Acar, 2010). However, it was deemed that the detection accuracy of mercury and the calculated extraction rates were not sufficiently reliable to ascertain a distinct relationship between mercury extraction and cyanide concentrations. Therefore, it was assessed that cyanide has a generally weak influence on mercury extraction rates.

Under varying pH, the lowest extraction was observed at pH 11.0 and higher extractions were observed at both pH 10.5 and pH 11.5. However, the residue used for the pH 11.0 experiment contained a higher mercury content of 8.5g/t Hg compared to 6.44g/t and 6.69g/t Hg for the other experiments, which may have inhibited the results. *Mikac et al (2007)* and *Luna & Lapidus (2000)* have both discussed the rate-inhibiting effects of higher solid concentrations in mercury sulfide and silver sulfide systems, respectively. Therefore, the pH 11.0 experiment was considered to be an outlier and it was deduced from the remaining two experiments that pH has a marginal impact on mercury extractions from the Leach Residue.

Mercury extraction increased considerably under oxygen-sparging, although the change was not proportional. The significant impact of oxygen is synonymous with the pure mercury sulfide experiments where dissolved oxygen concentrations inflicted a considerable impact on the dissolution rates. Extraction from the Leach Residue was also considerably affected by the

temperature increase from 25°C to 35°C, but this was not the case in pure mercury sulfide experiments.

In many ways, mercury extraction from the Leach Residue did not resemble the kinetic experiments using pure mercury sulfide. It is apparent that mercury extraction is not particularly responsive to cyanide concentrations and pH, but it is strongly influenced by both oxygen and temperature. However, these results only provide a qualitative perspective, and further investigations are necessary to confirm the exact leaching relationships. Considering that mercury analysis can be inaccurate at low concentrations, much higher pulp densities are recommended for future tests.

7 Conclusion

The dissolution kinetics of silver sulfide and mercury sulfide in cyanide solutions were investigated through rotating disc and stirred reactor experimental methods, respectively. The results were compared to experimental extraction results of a Heap Leach Residue sample provided from the Yanacocha Mine. In all experiments, the effects of varying cyanide concentrations, pH, oxygen concentration, and temperature were investigated. For the pure silver sulfide work, the effects of hydrogen peroxide and ferricyanide as additional oxidants were also tested.

The rotating disc method proved to be a reliable method of attaining reproducible dissolution rates from silver sulfide discs. However, non-linear results occurred during long experiments due to a suspected inhibition of kinetics caused by saturation of dissociated sulfide products. This issue was circumvented by calculating the dissolution rate only from the initial 20-30 minutes of leaching and using fresh silver sulfide discs for each experiment. The results were explained by the Levich equation to determine the rate-limiting mechanism. It was assessed that silver sulfide dissolution is controlled by the mass-transport of cyanide, but nearly independent of oxygen concentration and pH. The addition of hydrogen peroxide and ferricyanide were not highly effective for improving the kinetics.

Mercury sulfide investigations were conducted by the stirred reactor method, and the shrinking-core Parabolic Leach equation was used to obtain rate constants as kinetic indicators (k_2'). Three HgS species were initially considered that possess different crystal structures:

cinnabar, metacinnabar, and a mercury sulfide precipitate. Preliminary leaching tests confirmed that cinnabar is practically insoluble in cyanide solutions, but that metacinnabar demonstrates a moderate solubility. The precipitate demonstrated the highest solubility, but it was not used in further experiments because its morphology would be difficult to reproduce for replicate experiments. Thus, kinetic studies were only conducted using metacinnabar. Kinetic studies of mercury sulfide (metacinnabar) revealed that its reaction is limited by the diffusion of cyanide through a porous product layer by applying the Parabolic Leach equation. Mercury sulfide extraction was also strongly influenced by oxygen and pH, which was thought to be due to their contribution in oxidizing sulfide and thiocyanate to thiosulfate.

Silver extraction from the Yanacocha Leach Residue increased with cyanide concentration, oxygen concentration, and temperature, which was analogous to the pure silver sulfide experiments. However, the relationship to pH was reversed where the highest extraction was observed at the lowest pH. Mercury extractions from the Leach Residue were not significantly affected by cyanide concentration and pH, which is contrary to the observations from the pure mercury sulfide experiments. However, extraction rates increased considerably under oxygen-sparging, which is analogous to the mercury sulfide experiments.

From this work, the dissolution and extraction kinetics of pure silver sulfide and mercury sulfide in cyanide media have been thoroughly investigated, but numerous discrepancies were observed between the experimental results of pure materials and the Leach Residue. This was particularly true for the mercury dissolution investigations. It is believed that complex mineral

interactions may be affecting the extraction kinetics in the residue, and further investigations are required to understand these mechanisms in detail. Furthermore, it is felt that the dissolution kinetics of mercury and mercury sulfide may be complex and further investigations are strongly recommended.

References

- Acanthite Properties. (2013). *Mindat.org*. Retrieved March 21, 2013, from <http://www.mindat.org/min-10.html>
- Acar, S. (2010). *Silver Deportation of Two Minera Yanacocha Silver Study Samples* (pp. 1–60). Denver, Colorado.
- Breuer, P. L., Jeffrey, M. I., & Hewitt, D. M. (2008). Mechanisms of sulfide ion oxidation during cyanidation. Part I : The effect of lead (II) ions. *Minerals Engineering, 21*, 579–586.
- Breuer, P. L., Sutcliffe, C. a., & Meakin, R. L. (2011). Cyanide Measurement by Silver Nitrate Titration: Comparison of Rhodanine and Potentiometric End-points. *Hydrometallurgy, 106*, 135–140.
- Brooks, W. E. (2010). *2010 Minerals Yearbook, Silver*.
- Brooks, W. E. (2010). *2010 Minerals Yearbook, Mercury*.
- Brooks, W. E. (2011). *2011 Minerals Yearbook, Mercury*.
- Broussard, L. A. (2002). *The Toxicology of Mercury. Laboratory Medicine* (Vol. 33, pp. 614 – 625). New Orleans.
- Butterman, W. C., & Hilliard, H. E. (2004). *USGS Mineral Commodity Profiles - Silver* (pp. 5–40).
- Costa, M. C., Botelho do Rego, A. M., & Abrantes, L. M. (2002). Characterization of Natural and an Electro-oxidized Arsenopyrite: A Study on Electrochemical and X-ray Photoelectron Spectroscopy. *International Journal of Mineral Processing, 65*(2), 83–108
- Dickson, F., & Tunnell, G. (1959). The Stability Relations of Cinnabar and Metacinnabar. *Journal of Mineralogical Society of America, 44*, 471–487.
- Dixon, D. G. (2000). *Modeling of Leaching Reactors (Short Coarse Slides)*. Vancouver, B.C.
- Dutrizac, J. E. (1994). The Leaching of Silver Sulphide in Ferric Ion Media. *Hydrometallurgy, 35*, 275–292.
- Eurick, G. M. (2000). *The Management of Mercury in the Modern Gold Mining Industry* (pp. 1–9). Reno, NV.
- Gileadi, E. (1993). *Electrode Kinetics for Chemists, Chemical Engineers and Material Scientists* (pp. 83 – 92). Wiley-VCH.
- Hiskey, J. B., & Sanchez, V. M. (1990). Mechanistic and kinetic aspects of silver dissolution in cyanide solutions. *Journal of Applied Electrochemistry, 20*, 479–487.

- Holley, E., McQuillan, J., Craw, D., Kim, J., & Sander, S. (2007). Mercury mobilization by oxidative dissolution of cinnabar (α -HgS) and metacinnabar (β -HgS). *Chemical Geology*, 240(3-4), 313–325.
- Jasinski, S. (1994). *The Materials Flow of Mercury in the United States* (pp. 1–27).
- Kitco. (2013). 2000-2013 Multi Year Silver Chart. *Kitco Metals Inc.* Retrieved from http://www.kitco.com/scripts/hist_charts/yearly_graphs.plx
- Li, J., & Wadsworth, M. (1993). Electrochemical Study of Silver Dissolution in Cyanide Solutions. *The Electrochemical Society*, 140(7), 7–13.
- Luna, R. M., & Lapidus, G. T. (2000). Cyanidation kinetics of silver sulfide. *Hydrometallurgy*, 56(2), 171–188.
- Luna-Sánchez, R. M., González, I., & Lapidus, G. T. (2003). A Comparative Study of Silver Sulfide Oxidation in Cyanide Media. *Journal of The Electrochemical Society*, 150(8), D155 – D161.
- Luthy, R. G., & Bruce, S. G. (1979). Kinetics of Reaction of Cyanide and Reduced Sulfur Species in Aqueous Solution. *Environmental Science & Technology*, 13(12), 1481–1487.
- McComb, M., & Thogerson, J. (2011). *Silver Characterization by SEM/MLA of a Yanacocha Spent Heap Leach Metallurgical Composite* (pp. 1–15). Englewood, Colorado.
- Mercury Properties. (2013). *Chemistry Explained - Foundations and Applications, Advameg, Inc2.* Retrieved March 21, 2013, from <http://www.chemistryexplained.com/elements/L-P/Mercury.html#ixzz2Az2UOfqr>
- Mikac, N., Foucher, D., Niessen, S., & Fischer, J.-C. (2002). Extractability of HgS (cinnabar and metacinnabar) by hydrochloric acid. *Analytical and Bioanalytical Chemistry*, 374(6), 1028–1033.
- Ohya, K., Inai, K., Nisawa, A., & Itoh, A. (2008). Emission statistics of X-ray induced photoelectrons and its comparison with electron- and ion-induced electron emissions. *Nuclear Instruments and Methods in Physics*, 266(4), 541–548.
- Penneman, R. A., & Jones, L. H. (1961). Infra-red Absorption Studies of the Aqueous Cyanide Complexes of Mercury, Cadmium, and Zinc. *Journal of Inorganic & Nuclear Chemistry*, 20(2), 19–31.
- Peters, E. (n.d.). Leaching Kinetics. *Hydrometallurgy: Theory and Practice (Course Notes)* (pp. IV–11 – IV–29). Vancouver, B.C.: Department of Metallurgical Engineering, U.B.C.
- Salazar, K., & McNutt, M. K. (2012). *Mineral Commodity Summaries 2012.*
- Senanayake, G. (2006). The Cyanidation of Silver Metal: Review of Kinetics and Reaction Mechanism. *Hydrometallurgy*, 81(2), 75–85.
- Serruya, A., Mostany, J., & Scharifker, B. R. (1999). The Kinetics of Mercury Nucleation from Hg_2^{2+} and Hg^{2+} Solutions on Vitreous Carbon Electrodes. *Journal of Electroanalytical Chemistry*, 464, 39–47.

Silver Properties. (2013). *Chemistry Explained - Foundations and Applications*, Advameg, Inc. Retrieved January 11, 2013, from <http://www.chemistryexplained.com/elements/P-T/Silver.html#b#ixzz2Az1fiujL>

Tromans, D. (1998). Temperature and pressure dependent solubility of oxygen in water: a thermodynamic analysis. *Hydrometallurgy*, 48, 327–342.

Wadsworth, M. (2000). Surface Processes in Silver and Gold Cyanidation. *International Journal of Mineral Processing*, 58(1-4), 351–368.

Xie, F., & Dreisinger, D. (2007). Leaching of Silver Sulfide with Ferricyanide-Cyanide Solution. *Hydrometallurgy*, 88(1-4), 98–108.

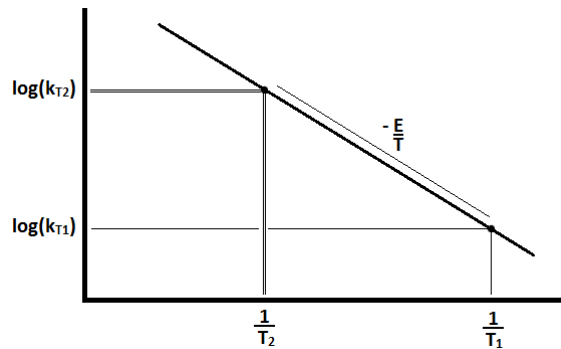
Appendix

Appendix A: Calculation of the Activation Energy

The use of the Arrhenius Rate Law for calculating the activation energy of a reaction is explained in this section (Dixon, 2000).

$$k_T = A \cdot \exp\left(-\frac{E}{RT}\right)$$

$$\log(k_T) = \log(A) + \left(-\frac{E}{RT}\right)$$



$$-\frac{E}{R} = \frac{\log(k_{T_1}) - \log(k_{T_2})}{\frac{1}{T_1} - \frac{1}{T_2}}$$

$$E = \frac{\log\left(\frac{k_{T_1}}{k_{T_2}}\right)}{\frac{1}{T_1} - \frac{1}{T_2}} \cdot (-R)$$

Appendix B: Mineral Assay of Heap Leach Residue

The mineralogical assays of all Leach Residue samples that were used in the current work are summarized. These values are related to the average head assays of silver and mercury that are presented in Table 3 in section 4.1.4.

Due to the low concentrations of silver and mercury available in the residue, the mineralogical analysis may not be entirely precise. The following are the data provided by Newmont Mining.

SEM/MLA Mineralogy Data of Leach Residue (report by Newmont Mining Corporation)				
Mineralogy		Association with Base Metal Minerals		
Mineral	Composition	Acanthite	Cinnabar	Velikite
Quartz	91.04%	17.80%	4.20%	9.30%
FeOx	6.46%	73.00%	25.90%	0.00%
Rutile	0.68%	0.80%	0.00%	0.00%
Barite	0.57%	6.00%	0.00%	0.00%
Pyrite	0.31%	0.50%	3.60%	52.60%
Alunite	0.19%	0.00%	0.00%	0.00%
Zircon	0.14%	0.00%	0.00%	0.00%
Svanbergite	0.13%	0.00%	0.50%	0.00%
Pyrophyllite	0.10%	0.00%	0.00%	0.00%
Beaudantite	0.10%	0.00%	2.20%	0.00%
Topaz	0.07%	0.00%	0.00%	0.00%
Calcite	0.07%	0.00%	0.00%	0.00%
Sericite	0.04%	0.00%	0.00%	0.00%
Zeolite	0.03%	0.00%	0.00%	0.00%
Diaspore	0.03%	0.00%	0.00%	0.00%
Energite	undeclared	0.00%	24.90%	16.40%

Exposed (Leachable) Surface of Ag and Hg Minerals			
Free Surface at 80% particle size	Acanthite	Cinnabar	Velikite
10-mesh passing (1700 microns)	1.80%	36.40%	13.80%
120 microns	75%	NA	NA

The following are head assays of the tested Leach Residue samples from the current work.

Experimental Head Assays of Silver and Mercury		
Experimental Condition Tested	Ag	Hg
	g/t	g/t
0.5 gL	13.88	14.14
35C	13.87	9.67
pH 10.5	14.02	6.69
pH 11.0	13.98	8.5
oxygen	14.06	9.75
0.25 gL	13.49	6.57
baseline (0.10gL, pH 11.5)	13.79	6.44
Average	13.87	8.82